

VILNIUS UNIVERSITY  
CENTER FOR PHYSICAL SCIENCES AND TECHNOLOGY

Edgaras  
MARKAUSKAS

# LASER PROCESSES FOR MONOLITHIC INTERCONNECTION FORMATION IN THIN-FILM SOLAR CELLS

**DOCTORAL DISSERTATION**

Technological Sciences, Materials Engineering T008

---

VILNIUS 2019

This dissertation was written between 2014 and 2018 in the Department of Laser Technologies of the Center for Physical Sciences and Technology.

**Scientific supervisor:**

Dr Gediminas Račiukaitis (Center for Physical Sciences and Technology, Technological Sciences, Material Engineering – T008).

## TABLE OF CONTENTS

TABLE OF CONTENTS .....	3
ACKNOWLEDGMENTS.....	6
LIST OF ABBREVIATIONS .....	7
1. INTRODUCTION.....	8
1.1 THE AIM OF THE RESEARCH.....	9
1.2 PRACTICAL VALUE AND NOVELTY.....	9
1.3 STATEMENTS TO DEFEND.....	10
1.4 APPROBATION.....	10
1.4.1 SCIENTIFIC PAPERS.....	11
1.4.2 CONFERENCE PRESENTATIONS .....	11
1.4.3 AUTHORS CONTRIBUTION .....	13
1.4.4 CO-AUTHORS CONTRIBUTION .....	13
2 LITERATURE REVIEW.....	14
2.1 PHOTOVOLTAICS IN THE GLOBAL ENERGY MARKET.....	14
2.2 SOLAR SPECTRUM.....	15
2.3 CRYSTALLINE SILICON SOLAR CELLS VERSUS THIN-FILMS .....	16
2.4 OPERATION OF THE SOLAR CELL .....	17
2.5 CIGS ABSORBER BASED SOLAR CELLS .....	22
2.5.1 CZTS SOLAR CELLS .....	24
2.6 FROM CELLS TO MODULES: MONOLITHIC SERIES INTERCONNECTION .....	25
2.7 PATTERNING OF THIN-FILM SOLAR CELLS: LASER VERSUS MECHANICAL SCRIBING .....	27
2.7.1 MECHANICAL SCRIBING.....	28
2.7.2 LASER SCRIBING .....	28
2.7.3 LASER PATTERNING: P1 STEP.....	29
2.7.4 P2 PROCESSING STEP.....	31
2.7.4.1 P2 PROCESSING: DIRECT LASER ABLATION .....	31
2.7.4.2 P2 PROCESSING: COMPLETE LIFT-OFF .....	32
2.7.4.3 P2 PROCESSING: LASER MICRO-WELDING .....	32
2.7.5 P3 PROCESSING STEP.....	33
2.7.5.1 P3 PROCESSING: DIRECT ABLATION AND TCO LIFT-OFF..	33
2.7.5.2 P3 PROCESSING: COMPLETE LIFT-OFF .....	34
2.8 LASER SCRIBING OF THIN-FILM SOLAR CELLS REPORTED IN THE LITERATURE.....	35
2.9 THEORY OF LIGHT-MATERIAL INTERACTION.....	38
3 EXPERIMENTAL SETUPS, PROCEDURES, AND MATERIALS	40
3.1 LASER SOURCES.....	40
3.2 OPTICAL SETUPS .....	41
3.3 MORPHOLOGICAL, TOPOGRAPHICAL AND ELEMENTAL ANALYSIS .....	42

3.4	THIN-FILM SOLAR CELL SAMPLES.....	42
3.5	RAMAN ANALYSIS .....	43
3.6	DIRECT MEASUREMENT OF SOLAR CELL ELECTRICAL CHARACTERISTICS .....	44
3.7	NESTED CIRCULAR LASER SCRIBING TECHNIQUE .....	44
3.8	LINEAR LASER SCRIBING TECHNIQUE .....	46
3.9	SERIAL INTERCONNECT SIMULATIONS .....	47
3.9.1	MINI-MODULE EFFICIENCY VERSUS P2 SCRIBE CONDUCTIVITY .....	48
3.9.2	MINI-MODULE EFFICIENCY VERSUS P3 SCRIBE CONDUCTIVITY .....	49
3.10	MODELLING OF THE ENERGY COUPLING IN THIN-FILM SOLAR CELLS .....	49
4	DEVELOPMENT OF PARALLEL RESISTANCE MEASUREMENT TECHNIQUE .....	51
4.1	EVALUATION OF THE NESTED CIRCULAR LASER SCRIBING TECHNIQUE .....	52
4.2	SIMULATION OF THE SOLAR CELL PARALLEL CONDUCTANCE MEASUREMENT .....	55
4.3	LINEAR LASER SCRIBING TECHNIQUE.....	58
4.4	CONCLUSIONS.....	60
5	P3 ISOLATION SCRIBES: OPTIMISATION OF THE LASER WAVELENGTH .....	61
5.1	SEM MORPHOLOGY ANALYSIS OF P3 TYPE 1 AND P3 TYPE 2 CHANNELS.....	62
5.2	P3 SCRIBE CONDUCTIVITY MEASUREMENTS.....	64
5.3	SIMULATION OF LASER-INDUCED TEMPERATURE DISTRIBUTIONS IN CIGS CELL.....	65
5.4	CONCLUSIONS.....	66
6	P3 ISOLATION SCRIBES: THE CASE OF HIGH-SPEED SCRIBING .....	68
6.1	HIGH-SPEED P3 SCRIBING IN CIGS SOLAR CELLS. SEM MORPHOLOGY ANALYSIS .....	69
6.2	SCRIBE CONDUCTIVITY MEASUREMENTS .....	70
6.3	P3 PROCESSING OF THE MINI-MODULE .....	71
6.4	MINI-MODULE EFFICIENCY SIMULATION.....	73
6.5	HIGH-SPEED SCRIBING OF P3 TYPE 2 CHANNELS .....	74
6.6	CONCLUSIONS.....	76
7	P3 LIFT-OFF SCRIBING OF CZTSE THIN-FILM SOLAR CELLS.....	77
7.1	LIFT-OFF CRATER SIZE DEPENDENCE ON THE LASER PULSE DURATION .....	78
7.2	PUNCHING THRESHOLD OF CZTSE LIFT-OFF CRATERS.....	80
7.3	MORPHOLOGICAL ANALYSIS OF CZTSE LIFT-OFF CRATERS .....	81

7.4	MICRO-RAMAN SPECTROSCOPY OF CZTSE SAMPLES .....	82
7.5	P3 SCRIBE CONDUCTIVITY MEASUREMENTS AND COMPARISON WITH TYPE 1 AND TYPE 2 SCRIBES .....	84
7.6	MINI-MODULE EFFICIENCY SIMULATION .....	85
7.7	CONCLUSIONS.....	87
8	FORMATION OF P2 INTERCONNECTS BY MODIFYING THE CONDUCTIVITY OF CIGS ABSORBER WITH A PICOSECOND LASER .....	88
8.1	CONDUCTIVITY OF MICRO-WELD CHANNELS IN CIGS SOLAR CELL.....	88
8.2	A CLOSER LOOK INTO THE MORPHOLOGY OF THE P2 MICRO- WELDS.....	90
8.3	MINI-MODULE EFFICIENCY SIMULATIONS .....	91
8.4	RAMAN AND EDS ANALYSIS OF THE LASER TRANSFORMED P2 INTERCONNECTS .....	92
8.5	CONCLUSIONS.....	95
	LIST OF MAIN CONCLUSIONS .....	96
	SUMMARY .....	97
	REFERENCES.....	98

## ACKNOWLEDGMENTS

I am grateful to my scientific supervisor Dr G. Račiukaitis for his support and advice.

I am grateful to Dr P. Gečys and Dr M. Gedvilas for advices and valuable discussions.

I express my thanks to Dr R. Trusovas, Dr E. Stankevičius, Dr S. Indrišiūnas, Dr V. Stankevič, K. Ratautas, J. Dudutis, A. Žemaitis, and other colleagues from the Department of Laser Technologies for support and professional environment.

Thanks to Dr Ingrid Repins and Dr Carolyn Beall (NREL, USA) for fruitful discussions and support with CZTSe samples.

Thanks to EMPA (Switzerland) and Solarion AG (Germany) for support with CIGS samples.

This work was partially funded by the European Union FP7 Programme under grant agreement No. 609355 (APPOLO).

## LIST OF ABBREVIATIONS

Al:ZnO	aluminium doped zinc oxide
AM	air mass
a-Si	amorphous silicon
a. u.	arbitrary units
BB	black-body
CdS	cadmium sulphide
CdTe	cadmium telluride
CIGS	copper indium gallium (di)selenide
CIS	copper indium (di)selenide
CZTS	copper zinc tin sulphide
FF	fill factor
HAZ	heat affected zone
i-ZnO	intrinsic zinc oxide
LLST	linear laser scribing technique
MPP	maximum power point
NCLST	nested circular laser scribing technique
OPO	optical parametric oscillator
PL	photoluminescence spectroscopy
SSRM	scanning spreading resistance microscopy
PV	photovoltaic
STC	standard test conditions
TCO	transparent conductive oxide
XRF	x-ray fluorescence
ZnO	zinc oxide

## 1. INTRODUCTION

Most of worlds energy demand is satisfied by burning the fossil fuels, which is responsible for greenhouse gas emissions contributing to global warming. Climate and environmental concerns led to the rapid growth of renewable power generation [1]. It is forecasted that by the year 2050, the renewable energy will account to about 85 % of the total power generation with solar photovoltaics (PV) being one of the major renewable energy sources [2].

Wafer-based silicon solar cells dominate the current PV market with a share of 95.5 % [3]. However, the wafer-based silicon technology is near its limits in both conversion efficiency and reduction of costs. The future demand for PV electricity could be satisfied only by the low cost, low material consuming thin-film devices, such as copper indium gallium (di)selenide (CIGS) and copper zinc tin sulphide (CZTS) solar cells, which can be grown on large area flexible and light substrates.

However, fully-sized thin-film solar panels fabricated under the industrial conditions suffer from about 3 – 5 % reduction in power conversion efficiency compared to the small size solar cells. For example, a full-sized (1 m<sup>2</sup>) commercial CIGS module reaches a significantly lower conversion efficiency of 15.7 % compared to a single cell record of 22.6 % [4].

One of the several factors responsible for the drop in power conversion efficiency is the finite resistance of the transparent conductive oxide (TCO) in thin-film solar modules [5]. Resistance problems are addressed by dividing the large solar cell area into the number of serially connected cells.

Three high-precision scribes are required to realise a serial monolithic interconnect in thin-film PV. The P1 scribe is needed for the patterning of the back-contact, the P2 forms the series interconnect between the TCO and the back-contact, and, lastly, the P3 scribe is needed for isolation of the neighbouring cells. However, the area between P1 and P3 scribes is inactive and does not contribute to the photocurrent generation. In the mass production, the P1 step is realised mostly by a laser, but P2 and P3 scribes still rely on the needle scribing, which produces wide and uneven scribes. As a result, up to 5 % of the active module area, which could be used for power generation, is lost because of the interconnects.

On the other hand, a complete laser integration as a standard tool into the mass production line could minimise the area consumed by the interconnects to below than 1 %, this way, increasing the conversion efficiency of the device [6].

Although laser processing can significantly increase the active area of the module, the poorly optimised processing parameters generate additional paths

for leakage current [7]. In most cases, the efficiency of the all-laser patterned modules falls behind the widely adopted needle scribing regarding the device efficiency [6, 8].

For this reason, precise optimisation and control over the laser parameters are essential to reduce damage to the solar cell layers. Such a task requires comprehensive and time-consuming experiments, especially when statistical analysis is necessary. Most of the direct electrical measurement techniques are complex, often require specific sample preparation, time-consuming or provide unreliable results. Therefore, the ability to quickly and reliably apply direct electrical measurements to evaluate the laser-induced damage in the thin-films becomes of the first importance.

For such a task, a novel direct electrical measurement technique (LLST) was developed and investigated in the first part of this thesis (Chapter 4). In Chapter 5, an influence of the laser wavelength to the conductivity of laser P3 scribes was investigated in CIGS thin-film solar cells. In Chapter 6, the high-speed and high-pulse repetition rate scribing of P3 scribes in CIGS solar cells was investigated. In Chapter 7, the complete lift-off process in CZTSe solar cells was investigated. In the last chapter (Chapter 8), picosecond laser pulses were used to locally transform CIGS absorber layer into a highly conductive compound to act as P2 interconnects.

## 1.1 The aim of the research

The research aimed to investigate the laser processing of the P2 and P3 scribes in thin-film solar cells searching for optimal laser pulse duration, laser repetition rate, wavelength, and various scribing approaches based on the in-house developed novel direct electrical measurement technique of electrical performance of the thin-film solar cells.

## 1.2 Practical value and novelty

1. A novel LLST direct electrical measurement technique was developed and tested to quickly and reliably measure the parallel conductivity of laser scribed channels in thin-film solar cells.
2. Laser scribing process of thin-film CIGS and CZTSe solar cells was thoroughly optimised regarding laser radiation wavelength, pulse repetition rate and pulse duration based on scribe conductivity values extracted by LLST.
3. Experiments showed that a picosecond laser could be used to locally transform CIGS into a low resistivity compound suitable for the P2 interconnects. This processing method can simplify and reduce the

costs of thin-film module production by applying the P2 and P3 scribes simultaneously.

4. A complete lift-off approach attracted much attention among many research groups due to the suppressed melting of the absorber layer associated with low scribe conductivity. However, the LLST measurements revealed the opposite: the complete lift-off approach produced the highest parallel conductivity scribes compared to the transparent conductive oxide (TCO) lift-off and direct laser ablation approaches, reducing the photo-electrical efficiency of solar cells.

### 1.3 Statements to defend

1. High measurement errors of the NCLST technique caused by the high areal conductivity of  $194 \text{ S/m}^2$  of the investigated solar cell can be avoided by tightly packing short laser scribes in a small area between the probe contacts, as proposed in the LLST technique.
2. By selecting proper laser wavelength, it is possible to control the laser energy coupling between thin layers of CIGS solar cell, which is essential to maintain required layer ablation selectivity and minimise the conductivity of the P3 scribes.
3. Heat accumulation during the P3 laser scribing in the solar cell layers is directly dependent on the laser pulse repetition rate triggering the formation of the highly conductive phase, which could result in the efficiency reduction of the CIGS solar cell.
4. Processing with the 10 ps duration pulses induce smaller structural degradation of CZTSe and provide lower conductivity P3 complete lift-off scribes by 11.6 % and 23 % compared to 1 ps and 300 fs pulses, respectively.
5. Scribing with picosecond duration pulses at the 1 MHz pulse repetition rate can locally transform CIGS into a highly conductive copper-rich compound (CGSe), which can be used as a connecting material between the adjacent cells.

### 1.4 Approbation

The thesis is based on results published in 5 scientific peer-reviewed papers [A1-A5] and presented in 16 contributions to conferences [C1-C16]. The author presented 9 of the contributions personally. In total, the author's publication list includes 10 scientific papers and 29 presentations at the conferences.

### 1.4.1 Scientific papers

#### **Related to the topic of this thesis (Peer-reviewed and indexed in Clarivate Analytics WoS)**

[A1] E. Markauskas, P. Gečys, A. Žemaitis, M. Gedvilas, G. Račiukaitis, Validation of monolithic interconnection conductivity in laser scribed CIGS thin-film solar cells, *Solar Energy*, **120**, 35-43 (2015).

[A2] P. Gečys, E. Markauskas, A. Zemaitis, G. Raciukaitis, Picosecond Laser Modification of CIGS Active Layer, *Journal of Laser Micro Nanoengineering*, **11(2)**, 257-260 (2016).

[A3] P. Gečys, E. Markauskas, A. Žemaitis, G. Račiukaitis, Variation of P2 series interconnects electrical conductivity in the CIGS solar cells by picosecond laser-induced modification, *Solar Energy*, **132**, 493-502 (2016).

[A4] P. Gečys, E. Markauskas, S. Nishiwaki, S. Buecheler, R. De Loor, A. Burn, V. Romano, G. Račiukaitis, CIGS thin-film solar module processing: case of high-speed laser scribing, *Scientific Reports*, **7**, 40502 (2017).

[A5] E. Markauskas, P. Gečys, I. Repins, C. Beall, G. Račiukaitis, Laser lift-off scribing of the CZTSe thin-film solar cells at different pulse durations, *Solar Energy*, **150**, 246-254 (2017).

#### **Related to the topic of this thesis (Conference Proceedings)**

[A6] E. Markauskas, P. Gečys, G. Račiukaitis, Evaluation of electrical shunt resistance in laser scribed thin-films for CIGS solar cells on flexible substrates, *Proc. SPIE*, **9350**, 93500S-1-6 (2015).

#### **Not directly related to this thesis (Conference Proceedings)**

[A7] E. Markauskas, P. Gečys, Thin water film assisted glass ablation with a picosecond laser, *Procedia CIRP*, **74**, 328-332 (2018).

### 1.4.2 Conference presentations

#### **Directly related to the topic of this thesis**

[C1] E. Markauskas, P. Gečys, M. Gedvilas, G. Račiukaitis, I. Repins, C. Beall, *CZTSe thin-film solar cell patterning with ultrashort pulsed lasers*, The 15th Laser Precision Microfabrication Symposium, Vilnius, Lithuania, 2014.

[C2] E. Markauskas, P. Gečys, M. Gedvilas, G. Račiukaitis, I. Repins, C. Beall, *Laser lift-off patterning of kesterite thin-film solar cells with picosecond and femtosecond pulses*, 29th European PV Solar Energy Conference and Exhibition, Amsterdam, Netherlands, 2014.

[C3] P. Gečys, E. Markauskas, G. Račiukaitis, *Investigations of laser-induced layer lift-off processes for thin-film solar cell processing*, Laser Processing in Photovoltaics, Leipzig, Germany, 2014.

- [C4] P. Gečys, **E. Markauskas**, G. Račiukaitis, I. Repins, C. Beall, *Investigation of Ultrashort Pulsed Laser Induced Ablation Process in CZTS Thin-Films*, The International High Power Laser Ablation Conference, Santa Fe, USA, 2014.
- [C5] **E. Markauskas**, P. Gečys, G. Račiukaitis, *Evaluation of electrical shunt resistance in laser scribed thin-films for CIGS solar cell on flexible substrates*, SPIE. Photonics West 2015, San Francisco, USA, 2015.
- [C6] **E. Markauskas**, P. Gečys, G. Račiukaitis, *Evaluation of Picosecond Laser-Induced Shunt Resistance in CIGS Thin-Film Solar Cells*, Lasers in Manufacturing, Munich, Germany, 2015.
- [C7] **E. Markauskas**, P. Gečys, M. Gedvilas, G. Račiukaitis, I. Repins, C. Beall, *Ultrashort laser patterning and electrical shunt evaluation of CIGS and CZTSe thin film solar cells*, 30th European PV Solar Energy Conference and Exhibition, Hamburg, Germany, 2015.
- [C8] P. Gečys, **E. Markauskas**, A. Žemaitis, G. Račiukaitis, *Picosecond Laser Modification of GIGS Active Layer*, The 16th International Symposium on Laser Precision Microfabrication, Kitakyushu, Japan, 2015.
- [C9] A. Žemaitis, **E. Markauskas**, P. Gečys, G. Račiukaitis, *Pikosekundiniu lazeriu suformuotų režijų laidžio tyrimas plonasluoksniuose CIGS saulės elementuose*, 41-oji Lietuvos Nacionalinė Fizikos konferencija, Vilnius, Lithuania, 2015.
- [C10] P. Gečys, **E. Markauskas**, S. Nishiwaki, S. Buecheler, R.D. Loo, G. Račiukaitis, *High-speed processing of CIGS thin-film solar cells*, 10th International Conference on Photoexcited Processes and Applications, Brasov, Romania, 2016.
- [C11] P. Gečys, **E. Markauskas**, G. Račiukaitis, *High-Speed Laser Scribing of CIGS Thin-Film Solar Cells*, The 17th International Symposium on Laser Precision Microfabrication, Xi'an, China, 2016.
- [C12] **E. Markauskas**, P. Gečys, G. Račiukaitis, *High Laser Pulse Repetition Rate Ablation of the CIGS Thin-Film Solar Cells*, The International High Power Laser Ablation Conference, Santa Fe, USA, 2016.
- [C13] **E. Markauskas**, P. Gečys, G. Račiukaitis, I. Repins, C. Beall, *Investigation of P3 patterning approaches in CZTSe thin-film solar cells*, 31st European PV Solar Energy Conference and Exhibition, Munich, Germany, 2016.
- [C14] **E. Markauskas**, P. Gečys, G. Račiukaitis, *Optimization of P3 Laser Scribing Process in Thin-Film Solar Cells*, The 18th International Symposium on Laser Precision Microfabrication, Toyama, Japan, 2017.
- [C15] P. Gečys, **E. Markauskas**, G. Račiukaitis, *CIGS thin-film solar cell patterning at different wavelengths*, International Conference on Advanced Laser Technologies, Busan, South Korea, 2017.

**[C16] E. Markauskas**, P. Gečys, *Optimization of P3 laser process in CIGS thin-film solar cells*, 11th International Conference on Photo-Excited Processes and Applications, Vilnius, Lithuania, 2018.

### **Contribution to other presentations at conferences**

**[C17]** P. Gečys, **E. Markauskas**, J. Dudutis, G. Račiukaitis, *Modern laser micro-fabrication: case of industrial implementation*, The 6th International Conference on Power Beam Processing Technologies, Xi'an, China, 2016.

**[C18]** **E. Markauskas**, P. Gečys, *Thin Water Film Assisted Glass Ablation with a Picosecond Laser*, 10<sup>th</sup> CIRP Conference on Photonic Technologies, Fürth, Germany, 2018.

#### 1.4.3 Authors contribution

The author of this thesis made the major part in experimental work, measurements, and numerical calculations. His contribution includes:

- Development and assembly of the direct electrical measurement setup.
- Development of LLST technique in collaboration with Dr P. Gečys.
- Experimental patterning of CIGS and CZTSe solar cells.
- Visual (optical microscope, SEM), elemental (EDS), and structural analysis (Raman spectroscopy) of thin-film solar cells and laser-patterned areas.
- Experimental laser scribe conductivity measurements using NCLST and LLST techniques.
- Numerical simulations of the efficiency of CIGS and CZTSe mini-modules and laser-induced temperature distributions in CIGS solar cell.
- Analysis and interpretation of results. Writing scientific publications and presentation of the results in scientific conferences.

#### 1.4.4 Co-authors contribution

Work presented in this thesis was supervised by Dr Gediminas Račiukaitis and Dr Paulius Gečys. Experiments were based on ideas conceived together with Dr Paulius Gečys. In Chapter 4, the linear laser scribing technique was developed in collaboration with Dr Paulius Gečys. He also simulated CIGS structure parallel conductance dependence on the structure radius in Section 4.2. Dr Paulius Gečys performed part of CIGS scribing, and SEM imaging presented in Chapter 6 and the solar cell scribing in Chapter 8. Scribing of the actual working CIGS mini-module was performed, and I-V curves were extracted by Dr Andreas Burn and Dr Valerio Romano from University of Bern, Switzerland.

## 2 LITERATURE REVIEW

### 2.1 Photovoltaics in the Global Energy Market

The improving economy, industrialisation of developing nations, and the rapidly growing population require massive inputs of energy, which is regarded as the primary driver of economic growth [9, 10]. Worldwide energy consumption has continuously been increasing for many years. Let alone, in 2017 the worldwide energy consumption exceeded 13300 million tons of oil equivalent (corresponding to 151 PWh of energy) [11]. Most of that energy was extracted from traditional fossil fuels, such as coal, oil, and natural gases [12]. According to the BP report, these resources accounted for more than 85 % of all energy produced that year [11]. Excessive consumption of fossil fuels is not only responsible for increasing air pollution and carbon emissions but also diminishes limited fuel reserves [12].

Climate and environmental concern led to the rapid growth of renewable power generation to meet the rising energy demand [1]; renewables contributed nearly 50 % of the growth in power generation in 2017 [13].

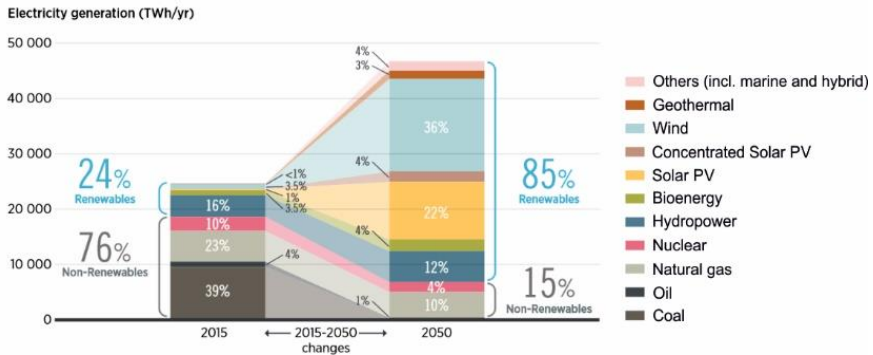


**Fig. 1.** Global electricity generation breakdown by electricity sources in 2015 and forecast of the year 2050. Figure adapted from [2].

One of the most promising renewable energy sources is harnessing the sun’s energy to produce electricity. In a single hour, the amount of solar energy reaching the Earth is more than the yearly energy demand of the entire world [14].

Photovoltaics produce safe and clean renewable energy, which can partially cover current electricity needs [12]. In 2016, the solar PV was the leading renewable power source considering the annual additions with the installed renewable power capacity of 43.3 % [15]. Global production of PV in 2017 accounted in 98 GW<sub>p</sub> reaching a cumulative installed PV capacity of

414 GW<sub>p</sub> (index p denotes that the generated power was measured under standard test conditions, which are discussed in the next chapter) [3].

The International Renewable Agency forecasted that by the year 2050 renewable energy share in power generation would account to 85 % (see Fig. 1) [2, 13]. Solar PV will become one of the two major sources for electricity generation with an estimated installed capacity of 7122 GW [2].

## 2.2 Solar spectrum

The solar light is electromagnetic radiation, which spans from the ultraviolet, visible light up to the infrared radiation. Outside the Earth’s atmosphere, the solar spectrum is similar to that what black body emits at the 6000 K (shown in Fig. 2 [16]). However, before reaching the Earth’s ground level, the light gets attenuated by the Earth’s atmosphere.

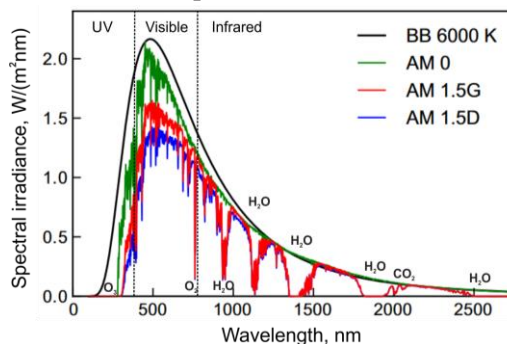


**Fig. 2.** The solar spectrum. Figure adapted from [16, 17].

Deviation from the black-body (BB) spectrum and breaks visible in Fig. 2 (radiation at sea level) are caused by the Rayleigh scattering, scattering from aerosols, absorption by various molecules, such as, water vapour (H<sub>2</sub>O), carbon dioxide (CO<sub>2</sub>), nitrogen dioxide (NO<sub>2</sub>), methane (CH<sub>4</sub>), oxygen (O<sub>2</sub>), ozone (O<sub>3</sub>), and various particles. [16, 18].

Attenuated light falling on the earth’s surface is generally characterised by the “Air Mass” coefficient  $AM = 1/\cos \theta$ , which is the shortest length of the path that light must travel through the atmosphere [18]. Here,  $\theta$  is the zenith angle in degrees. Extraterrestrial radiation is nominated by the AM0, while the AM1 represents the attenuated solar spectrum when it is normal to the earth’s surface. The sun is closest to the zenith at the midday, but on mornings and evenings, it is almost horizontal. Additionally, seasons have significant importance to the angle of the sunlight. Therefore, the Air Mass coefficient of 1.5 (AM1.5), which corresponds to  $\theta \approx 45^\circ$ , is generally used to evaluate the average annual irradiance for mid-latitudes [16]. Fig. 2 shows two cases of the AM1.5 spectrum: AM1.5D and AM1.5G. The former coefficient accounts

only the direct sunlight reaching the earth’s surface, while the latter includes both the direct sunlight and the scattered light from the atmosphere [17].

Indoor measurements on the performance of the photovoltaic device are generally performed under the standard test conditions (STC), which include the light spectrum similar to sunlight at AM1.5 conditions, device temperature fixed at 25 °C and irradiance of 1000 W/m<sup>2</sup> under normal incidence [19]. This way, solar modules can be compared relatively independently even if they derived from different technologies or manufacturers.

### 2.3 Crystalline silicon solar cells versus thin-films

Commercialised photovoltaic technologies can be divided into the first and second generation PV’s. The first generation is highly efficient but high-cost wafer-based mono- and poly-crystalline silicon solar cells. The second generation PV’s are the low-cost, lower efficiency thin-film cells, such as CIGS, cadmium telluride (CdTe), and amorphous silicon (a-Si) [20].

Wafer-based silicon PV currently dominates the solar cell market with a share of 95.5 % [3]. Crystalline silicon solar cells utilise well-known and abundant silicon as the absorber material. Currently, wafer-based Si modules are cheaper and more profitable than thin-film counterparts (see Fig. 3) [21].

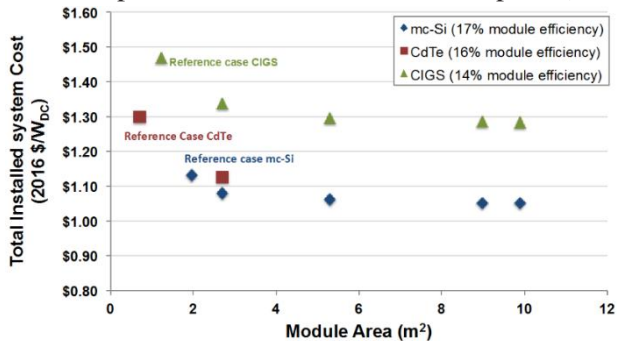


**Fig. 3.** Average total installed system cost by technology and module area [22].

On the other hand, the future for thin-film technologies is auspicious. Thin-films have a great potential in efficiency improvement and further cost reduction (material saving, a transition from glass substrates to large-scale roll-to-roll production). The wafer-based crystal-silicon technology is near its limits in both conversion efficiency and reduction of costs. Future demand for PV electricity could be satisfied by the low cost, low material consuming thin-film solar technologies.

Thin-films can be grown on flexible large-area substrates with minimum material usage [21]. Small weight and flexibility give an advantage over the traditional wafer-based PV technologies in applications such as mobile power

generation, building and transport integrated PV, as well as, space applications [23]. Flexible modules can be moulded to the curved surfaces, such as car roofs, facades, and other areas. Furthermore, they are lighter than modules on glass, and therefore require less mechanical support for mounting [24]. Thin-films can tolerate extreme heat conditions with efficiency losses significantly lower than the wafer-based Si counterparts, which makes them more suitable in tropical and subtropical regions [21, 25]. Combined with high device efficiency, thin-films becomes very competitive with crystalline silicon-based solar cells.

The most commercialised candidate solar cells are based on cadmium telluride (CdTe), copper-indium-gallium-(di)selenide (CIGS) or copper-indium-(di)selenide (CIS), and amorphous silicon (a-Si) semiconductor absorbers. Global thin-film PV module production between 2000 and 2017 is shown in Fig. 4 with the largest share for CdTe technology and continuously increasing production of CIGS.

Therefore, with thin-films becoming more efficient, cheaper to produce, and more reliable, it is expected that the thin-films will thrive soon [21].

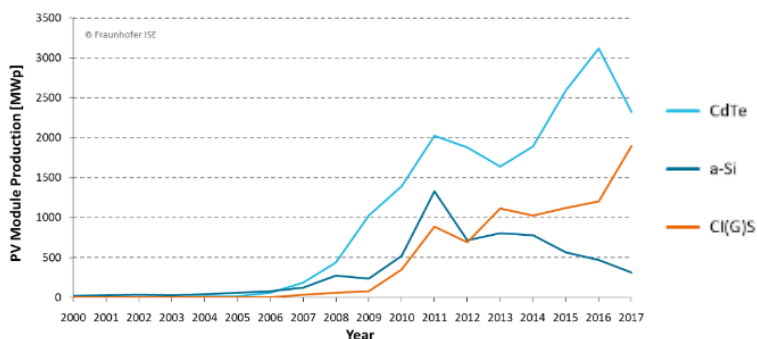


**Fig. 4.** Thin-film PV module production worldwide [3].

## 2.4 Operation of the solar cell

A solar cell is a semiconductor device, which directly converts sunlight into electricity when exposed to light. Operation of the solar cell can be divided into two steps: (1) generation of the charge carriers, and (2) separation of free carriers to produce electricity [18].

When the light is incident to a solar cell, a photon is absorbed, and a free electron-hole pair is generated. However, only suitable energy photons can be absorbed. The photon energy  $E_{ph} = hv$  must be equal to or greater than the bandgap energy  $E_g$  of the semiconductor, which is an energy range between the valence and conduction bands where no electron energy states can exist

[18]. Here,  $h$  is the Planck constant ( $\sim 6.62 \times 10^{-34} \text{ m}^2\text{kg/s}$ ), and  $\nu$  is the frequency of light.

After the electron-hole pair creation, charge carriers must be separated. Otherwise, they will recombine after a short period, and electrical energy will be lost. For that reason, a p-type and n-type semiconductors are joined together to form an electric field to separate photo-excited electrons and holes. Thin-film solar cells utilise a so-called hetero-junction, which is comprised of different types of extrinsic semiconductors (for example CIGS, cadmium sulphide (CdS), and intrinsic zinc oxide (i-ZnO)) [26].

The majority of charge carriers in an n-type semiconductor are free electrons, while in the p-type region, holes are the main charge carriers (see Fig. 5). Therefore, when n-type and p-type semiconductors are joined together, excess electrons in the n-type material diffuse to the p-type side due to the random thermal motion of the free electrons. Similarly, excess holes from the p-type material diffuse to the n-type side.

Diffusion of charge carriers results in the net negative charge build-up on the p-type semiconductor and the net positive charge build-up in the n-type semiconductor. This “built-in” electric field prevents further flow of electrons and holes. Furthermore, some of the charge carriers start to flow in the opposite direction than the diffusion (away from the p-n junction). Eventually, the net flow of electrons and holes across the junction become zero. No charge carriers remain in that area, also called, a depletion region.

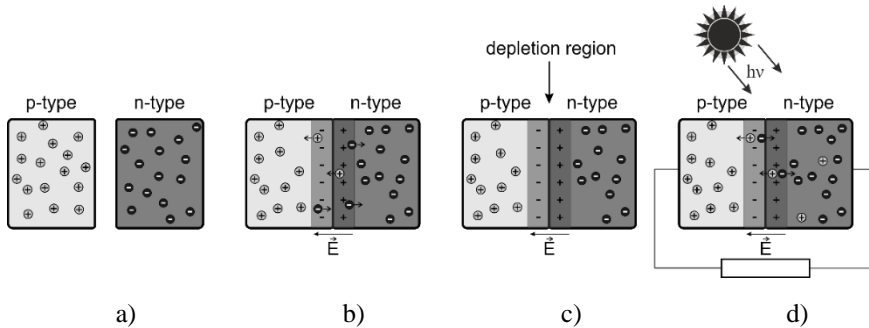


**Fig. 5.** Operation of a solar cell. P-type and n-type semiconductors (a) are joined together, and “built-in” electric field is formed (b). Electric field results in the depletion region at the junction (c). Charge carriers are created by the absorption of photons and are forced to travel through the external circuit.

The “built-in” electric field separates electrons and holes generated by light (photons). If the solar cell is connected to the external load (if the p-side and n-side of a photovoltaic cell are short-circuited), the light-generated current flow from the p-side to the n-side of the cell through the external circuit as shown in Fig. 5d [27].

A solar cell acts as a diode under dark conditions. If the diode is externally connected to the voltage source in the forward bias, then the current flowing through the diode under dark conditions can be expressed by Eq. (1) [26]:

$$I_D = I_0 \left( \exp \frac{qV}{\eta kT} - 1 \right). \quad (1)$$

Here,  $I_D$  is the dark current (flowing through the diode),  $I_0$  is the saturation current,  $q$  is the elementary charge,  $V$  is the voltage across the output terminals of the solar cell, and  $\eta$  is the diode emission coefficient. Boltzmann constant and solar cell temperature in Kelvin are described by  $k$  and  $T$ , respectively.

When the light shines on the solar cell, an output current  $I$  is generated:

$$I = I_D - I_{ph} = I_0 \left( \exp \frac{qV}{\eta kT} - 1 \right) - I_{ph} \quad (2)$$

This is the cell's output current, which flows into the external short-circuit. The output current is comprised of the diode current and photo-generated current  $I_{ph}$  flowing into opposite directions as shown in Fig. 6 [26, 27]:

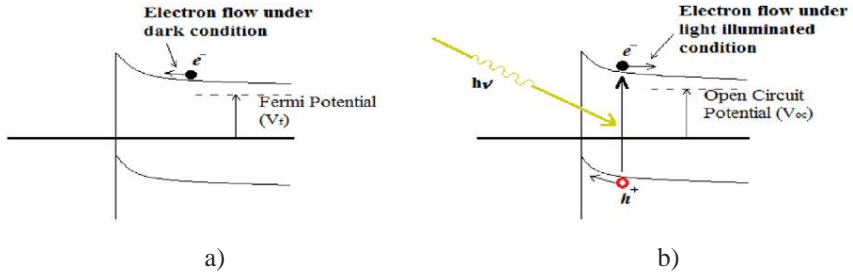


**Fig. 6.** Electron flow direction under the dark (a) and illuminated (b) conditions [16].

I-V (current-voltage) characteristic curve is one of the most important PV device's output performance revealing plots. I-V curves for dark and illuminated conditions were plotted in Fig. 7. As shown in the figure, when the solar cell is illuminated, it generates power, and the diode works in the fourth quadrant. When the solar cell is in dark conditions, the diode works in the first and third quadrants. According to equations (1) and (2), both curves are exactly the same; only the illuminated I-V curve is shifted down by the  $I_{ph}$ .

A photo-generated current  $I_{ph}$  is linearly related to the irradiance  $I_r$ , falling on the active cell area  $A$ , and short-circuit current density  $J_{sc}$ , which was measured at irradiance  $I_{0r}$ :

$$I_{ph} = J_{sc} A \frac{I_r}{I_{0r}}. \quad (3)$$

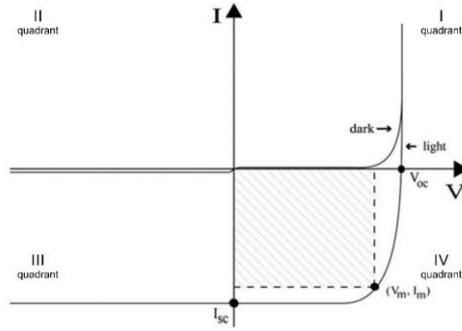


**Fig. 7.** I-V characteristics of a PV solar cell under dark and illuminated conditions [26].

However, solar cells are not ideal devices. They generally possess a parasitic series and shunt resistances, which negatively affect the illuminated I-V characteristics and efficiency of cells [28]. The equivalent circuit of a single solar cell incorporating series and shunt resistances is shown in Fig. 8.

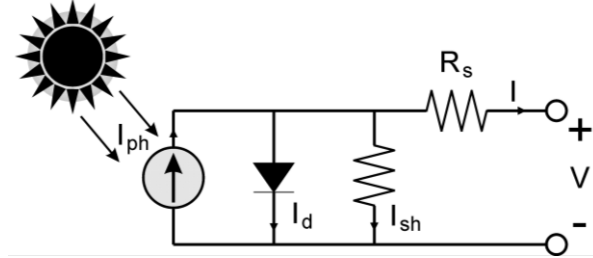


**Fig. 8.** Equivalent circuit of a single solar cell.

Equivalent circuit represents a single-diode model, which is commonly used for the modelling of the I-V curves of a cell, module, or arrays of modules. Accordingly, the equation (2) transforms as follows [29]:

$$I = I_{ph} - I_0 \left( e^{q(V+IR_s)/\eta kT} - 1 \right) - \frac{V+IR_s}{R_{sh}}. \quad (4)$$

High value of series resistance  $R_s$  reduce short-circuit current, while the low  $R_{sh}$  impairs the  $V_{OC}$  (open-circuit voltage) as indicated in Fig. 9. Furthermore, resistive losses become larger as substrate size increases [28]. Parasitic series resistance  $R_s$  arise mainly due to the front and back-contact resistances, the contact resistance between metal and the semiconductor, and the bulk resistance of the semiconductor itself. The shunt resistance  $R_{sh}$  is attributed to the imperfections on the device surface and in bulk, as well as from leakage currents across the p-n junction around the edge of the cell, crystal defects and impurities [28, 30].

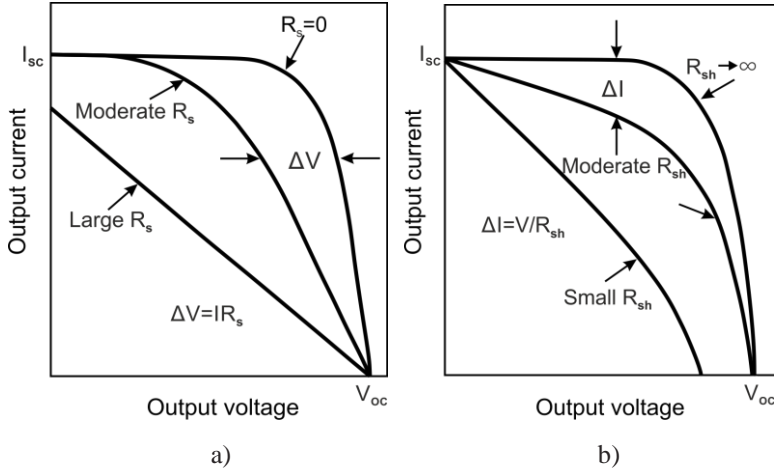


**Fig. 9.** Effect of series (a) and shunt (b) resistance to the I-V curve. Figures adapted from [30].

When analysing a solar cell device, important parameters include an open circuit voltage, a short circuit current density, a fill factor, and a conversion efficiency.

The open circuit voltage is the maximum voltage measured when no current is flowing through the external circuit. In this case,  $V_{OC}$  is derived from equation (2) by setting the output current  $I = 0$  (open circuit conditions):

$$V_{OC} = \frac{\eta k T}{q} \ln \left( \frac{I_{ph}}{I_0} + 1 \right). \quad (5)$$

The short circuit current density ( $J_{SC}$ ) is obtained when the solar cell is short-circuited (the voltage between the solar cell's output terminals is zero).

The shaded area in Fig. 7 represents the fill factor (FF). It is a fraction of electric power that can be drawn from the solar cell working at the maximum power point (MPP) [26]:

$$FF = \frac{V_m I_m}{V_{OC} I_{SC}}, \quad (6)$$

where  $V_m$  and  $I_m$  represent the output voltage and current at which the maximum power can be drawn from the cell and are linked by the load resistance  $R_L$ , according to Ohm's law:

$$V = R_L \cdot I. \quad (7)$$

MPP is dependent on many factors, such as solar irradiance, solar cell temperature and so on. Therefore, commercially available PV devices either adjust load resistance electronically so that the PV cell/module is always operated at its MPP, or has a fixed load resistance that keeps the module near MPP at normal operating conditions [18].

Solar cell's energy conversion efficiency ( $\eta_{eff}$ ) is the most commonly used parameter to compare different solar cell devices. It is equal to the ratio

between the output power of a solar cell  $P_{out}$  and the incident power  $P_{in}$  onto the solar cell [26]:

$$\eta_{eff} = \frac{P_{out}}{P_{in}} = \frac{V_{OC} \cdot I_{SC} \cdot FF}{P_{in}}. \quad (8)$$

## 2.5 CIGS absorber based solar cells

$\text{Cu}(\text{In}_x, \text{Ga}_{(1-x)})\text{Se}_2$  (CIGS or CIS)-based solar cells are one of the most promising amongst other PV technologies. It is a direct bandgap quaternary I-III-VI<sub>2</sub> polycrystalline semiconductor comprised of copper, indium, gallium, and selenium elements [31]. Crystals have a chalcopyrite structure, presented in Fig. 10.

CIGS has many advantages over the other conventional PV technologies. First of all, the bandgap can be tuned in a wide range between 1.04 and 1.7 eV to accommodate the device for different operation conditions [32]. CIGS possess a high absorption coefficient of  $10^5 \text{ cm}^{-1}$ , meaning that the incoming photons with energy higher than the bandgap are mostly absorbed within the first micrometer of the absorber layer. This way, the CIGS absorber layer can be hundreds of times thinner compared to the silicon wafers. The typical CIGS absorber layer thickness is about 2 - 2.5  $\mu\text{m}$  [32-34]. CIGS also possess a high energy yield (kWh/KWp installed), a low temperature coefficient of power loss, and short energy payback time [23].

Over the years, CIGS experienced a steady performance increase showing the successful development of the technology (see Fig. 10b). The first thin-film CIGS solar cell was manufactured in 1976 and had a conversion efficiency of 4.5 % [21]. Current laboratory scale cell record of 22.9 % is held by Solar Frontier [4]. The same company holds the record efficiency of 19.2 % for the  $30 \times 30 \text{ cm}^2$  submodule [4]. CIGS thin-film technology has been mostly developed on the glass substrates, and for a long time, CIGS solar cells deposited on flexible substrates (such as polyimide or metal foils) could not reach similar efficiencies [23]. However, efficiencies above 20 % have now been demonstrated on a polyimide substrate [35].

However, several issues should be addressed for successful large-scale commercialisation. It mainly concerns CIGS compositional uniformity between different batches and standardisation of equipment for growth and processing of CIGS layers [32].

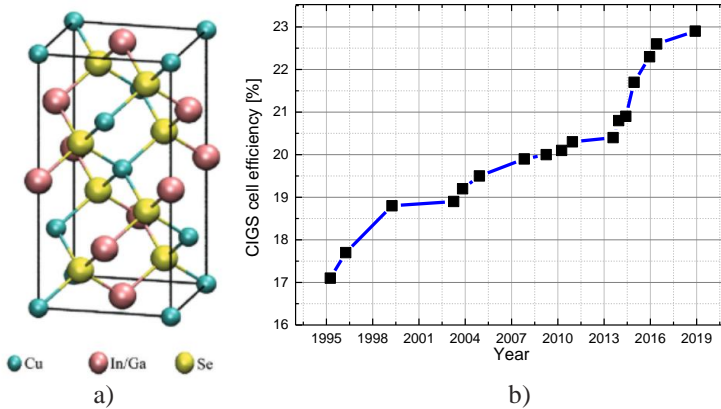


**Fig. 10.** Crystal structure of tetragonal chalcopyrite CIGS unit cell (a) [36]. Improvement in record efficiencies of CIGS solar cells [4, 21, 37-41].

Fig. 11 shows a layer structure of a typical CIGS cell. First of all, a substrate for the CIGS device is selected. The purpose of the substrate is the structural integrity of the CIGS device. Glass plates, polymer sheets and metal foils, such as steel or aluminium are mostly used. On top of the substrate, a thin 0.5 - 1  $\mu\text{m}$  molybdenum (Mo) layer is sputtered. This layer is used as the back-contact of the cell. Afterwards, polycrystalline p-type CIGS absorber with a thickness of several micrometres is grown. Co-evaporated CIGS layers make up the highest efficiency devices. On top of a CIGS film, n-type cadmium sulphide (CdS), undoped zinc oxide (ZnO), and Al:ZnO (aluminium-doped ZnO) layers are deposited to form a p-n junction with a CIGS absorber [24, 42]. CdS layer is usually 10 – 50 nm thick and is deposited using chemical-bath-deposition. Undoped ZnO and transparent conductive oxide (TCO) are usually sputtered with total thickness not exceeding 1  $\mu\text{m}$ . Here, Al-doped ZnO layer acts as a TCO. Optionally, an anti-reflection layer of  $\text{MgF}_2$  can be deposited on top of the TCO in order to limit the reflection losses.

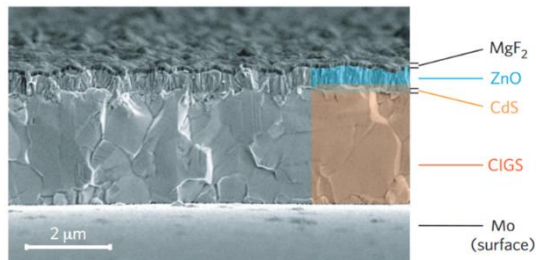


**Fig. 11.** Cross-section image of the CIGS solar cell [34]

### 2.5.1 CZTS solar cells

It is feared that the CIGS technology might not meet the future demand in scale grid level production [43]. The main concern lies in the scarcity of indium and gallium metals, which are crucial components in CIGS solar cells [44]. In particular, indium is one of the least abundant minerals on Earth, and high demand from the display industry can result in the growth of its price or even partial shortage of the material [43].

Therefore,  $\text{Cu}_2\text{ZnSnS}_4$  (CZTS),  $\text{Cu}_2\text{ZnSnSe}_4$  (CZTSe), and their alloy -  $\text{Cu}_2\text{ZnSnSSe}_4$  (CZTSSe) attracted much attention as a potential replacement for the CIGS technology. For the sake of brevity, in further text CZTS, CZTSe and CZTSSe compounds will be referred to as CZTS or kesterites, unless stated otherwise.

CZTS substitute scarce indium and gallium with much more abundant and non-toxic zinc (Zn) and tin (Sn). Moreover, the availability of Zn and Sn is 500 times and 14 times higher compared to that of In [45].

The crystalline structure of CZTS is presented in Fig. 12a. It can come in the tetragonal kesterite phase or stannite phase. The formation energy difference between these two phases is only 1.3 meV/atom; therefore, it is likely that both phases coexist in a single film or a device [46, 47]. Both crystal structures are very similar: both have cations located at tetrahedral sites, but the difference lies in the distribution of Cu and Zn within the unit cell [48, 49].

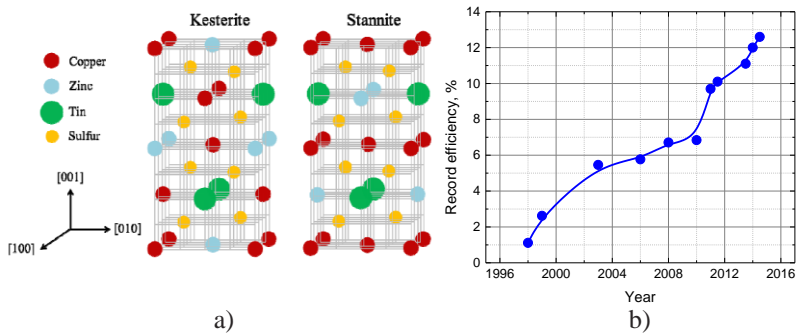


**Fig. 12.** The crystal structure of kesterite and stannite phases of CZTS [46] (a). Record efficiencies through a time of the CZTS solar cells [37-40, 50] (b).

CZTS as a suitable material for PV applications was confirmed in 1988 and the conversion efficiency for the first time was reported in 1996 with 0.66 % [51]. It is a second generation PV technology, which intense development resulted in a rapid efficiency rise with a currently certified record of 12.6 % for a  $0.42 \text{ cm}^2$  device (see Fig. 12b) [4]. CZTS possesses characteristics of a highly efficient device: the direct band-gap, which can be tuned over a range from 1.0 to 1.6 eV, and high absorption coefficient of

$10^4 \text{ cm}^{-1}$  allowing thin-film devices [43]. According to the Shockley-Queisser (SQ) limit, the maximum theoretical efficiency of the  $\text{Cu}_2\text{ZnSnSSe}_4$  solar cell (with a band-gap of 1.13 eV) is 31 % compared to the current record efficiency of 12.6 % [43]. CZTSe technology has a lot of room and potential for improvement. Champion cell performance describing parameters, such as open circuit voltage, short-circuit current density and fill factor are presented in Table 1. Currently, the  $V_{oc}$  deficit is the main obstacle responsible for falling behind CIGS and CdTe in terms of efficiency. The origin of the  $V_{oc}$  losses remains unclear; however, it is frequently associated with the charge-carrier recombination at defects in the bulk material and the charge extraction interfaces [21, 52].

Overall, CZTS thin-film solar cells have the same structure as CIGS cells, with similar processing strategies and challenges [21]. Low device efficiency and absorber stability are key issues preventing CZTS from commercialisation.

**Table 1.** Shockley-Queisser limit and record CZTS solar cell parameters [43].

	$\eta_{eff}, \%$	$V_{oc}, \text{mV}$	$J_{sc}, \text{mA/cm}^2$	FF, %
SQ limit	31	820	43.4	87.1
Achieved	12.6	513.4	35.2	69.8

## 2.6 From cells to modules: monolithic series interconnection

The size of a wafer-based Si solar cell is limited by the cylindrical crystal of silicon ingots, which can be grown only to a certain radius. Currently, 125 and 156 mm diameter cut-out Si cells are commercially available [53]. The typical size of solar panels used in a rooftop solar installation is approximately  $165 \times 100 \text{ cm}^2$ . Therefore, commercially available modules, depending on the size of the module, usually are comprised of 60 to 96 interconnected cells [54].

Individual cells are either connected in series or parallel. When the solar cells are connected in series, the open circuit voltage becomes the sum of  $V_{oc}$ 's of connected cells (see Fig. 13a). However, the current of each cell should be carefully matched, since the cell with the lowest current in a series limits the current of the whole module. I-V curves of a single, two, and three cells interconnected in series are shown in Fig. 13c.

Solar cells connected in parallel add up the current, while the  $V_{oc}$  remains equal to that of a single cell (or a weakest if there is one). Connection scheme is shown in Fig. 13b and I-V curves are shown in Fig. 13c [54].

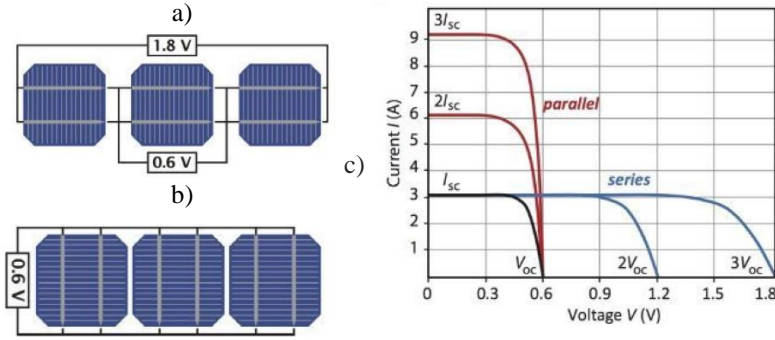


**Fig. 13.** A series (a) and parallel (b) connection of multiple cells. I-V curves of a single solar cell and multiple cells connected either in series or in parallel (c) [54].

Commercial thin-film panel sizes are similar to that of wafer-based counterparts: the dimensions of CIGS modules with glass as a substrate are about  $1250 \times 1000 \text{ mm}^2$  [55], while the flexible CIGS solar modules as large as  $3105 \times 411 \text{ mm}^2$  are already available [56].

Thin-film PV's have a significant advantage: solar cell layers can be uniformly deposited over the large area substrates. Therefore, it becomes possible to produce a single solar cell with the size of a solar panel without any additional interconnects needed. Unfortunately, large single solar cell modules are not produced but comprised of hundreds of smaller cells interconnected in series.

The reason for that is that the large solar cells produce a very high current. All the generated current should be transported across the thin contacts, meaning that resistive losses in the module could be detrimental.

The open-circuit voltage is independent of the cell size and roughly equals to  $V_{oc} = E_g/q - 0.5$ , meaning that the CIGS cell produces a voltage between 0.5 and 1.2 V [57]. Furthermore, equation (3) shows that the generated photocurrent  $I_{ph}$  is linearly proportional to the active area of the cell. This way,  $1.25 \text{ m}^2$  area solar cell with  $\eta_{eff} = 15.7 \%$  theoretically could generate 490 A current and just 0.5 V of voltage (resulting in the output power of 196 W). In reality, however, a module would suffer from significant power losses in the form of heat due to the resistance of thin contacts.

For this reason, the large area cells are divided into smaller ones and interconnected in series. This way, a photocurrent is limited to the current generated by a single solar cell, only the voltage is proportionally increased to maintain the same generated power. Such an approach allows bypassing the conductivity limitations of thin layers, therefore preserving the solar cell efficiency. For example, a commercially available module with the output power of about 170 W generates about 2 A at 85 V.

Three types of scribes are required to divide the large area module into smaller cells and interconnect them in series (to form monolithic serial interconnects) [58]. All scribing steps are performed in between layer deposition steps; therefore, the patterning becomes an integral part of the module production. The roll-to-roll-based production of CIGS solar cells is further discussed.



**Fig. 14.** Schematics of the roll-to-roll-based production of CIGS thin-film solar cells. Figure adapted from [59].

The P1 step is performed after the deposition of the back-contact (see Fig. 14). Its purpose is to completely cut through the conductive layer, thereby ensuring electrical isolation between the cells. P1 step defines the number and the width of the cells. P2 scribe is performed when the CIGS, and buffer layer are deposited. Its purpose is to open the back-contact layer, so when the conductive TCO layer is deposited, a series connection between the back and front contact layers of two adjacent cells is established. Finally, the P3 scribe produces electrical isolation in the front contact layer between neighbouring cells [60]. Fig. 15 shows the cross-section scheme of serially interconnected CIGS cells. All scribing steps are carried out from the thin-film side.

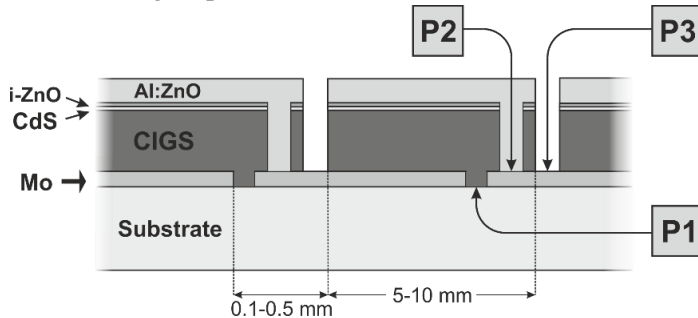


**Fig. 15.** Cross-section scheme of patterned CIGS solar module. Regions labelled with P1, P2, and P3 indicate the structuring patterns for the monolithic serial interconnection in CIGS module.

### 2.7 Patterning of thin-film solar cells: laser versus mechanical scribing

Monolithic interconnections are repeated across the device every 5 to 10 mm (see Fig. 15) [61]. It means that the typical 1 m<sup>2</sup> area module will consist of  $n = 100 - 200$  cells and  $n - 1$  interconnects [61]. The area between the P1 and P3 scribes is inactive and does not contribute to the photocurrent

generation. Consequently, it is referred to as the dead area. In other words, monolithic cell interconnections minimise ohmic losses by sacrificing part of the active module area.

### 2.7.1 Mechanical scribing

Mechanical scribing is the most used technology to perform P2 and P3 scribes for monolithic cell integration in CIGS thin-film PV. It uses a stylus to create channels in thin-films, and reasonable results were shown with the scribing of the CIGS and the TCO layers [62]. However, mechanically scribed channels are wide, about 100  $\mu\text{m}$  in width, imperfect and of poor edge quality (see Fig. 16a, b). Delamination, uncontrolled layer chipping, and breakouts are common during the needle patterning, which forces to leave additional gaps between P1-P2 and P2-P3 scribes [63]. Depending on the process optimisation level, the width of interconnects (the dead area) can be as wide as 200 - 500  $\mu\text{m}$  [6, 63]. As a result, interconnects spaced every 10 mm will lose up to 5% of the active module area, which could be used for power generation. Another significant drawback of mechanical scribing is the variation of the scribe quality due to the constant mechanical wear of the needle, which causes system downtime for replacement and adjustment of the needles. Wear and tear also increase variation in a solar module efficiency from batch-to-batch.

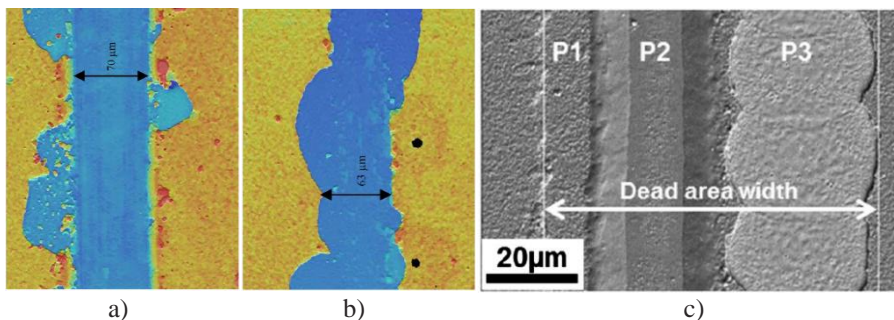


**Fig. 16.** Topography of the P2 (a) and P3 (b) channels performed by mechanical scribing. Random lift-offs and chipping of the layers are observed in the latter cases [64]. SEM image of the optimised dead area width of 70  $\mu\text{m}$  comprised of P1, P2, and P3 laser scribes (a) [6].

### 2.7.2 Laser scribing

Laser scribing is a competing technology, which has been actively developed for thin-film solar cell fabrication [58]. The advantages of the laser scribing technology for thin-film photovoltaics are evident: the non-contact origin, precise channel depth control, sharp boundaries, and reduction of the dead area compared to the conventional needle scribing. All-laser patterning can reduce the dead area below 100  $\mu\text{m}$ , minimising active area losses below 1 %

(see Fig. 16c) [6]. Additionally, laser scribing speed can easily reach several meters per second, which is not possible with a mechanical scribe, and lasers do not wear as the mechanical styluses do. Therefore, a laser tool fully integrated into the production lines of CIGS thin-films promises a stable channel formation, higher module efficiency and manufacturing throughput with less frequent system services (compared to mechanical scribing).

Lasers are extensively used in the production lines of flexible CIGS PV for all processing steps (P1, P2 and P3) since the mechanical scribing can easily damage the substrate. Additionally, it has been the process of choice to form a-Si and CdTe monolithic interconnections, where the laser processing takes place from the transparent substrate side [65].

However, CIGS thin-film modules use molybdenum as a back-contact, which is opaque. For this reason, the scribing can be applied only from the film side. Most of CIGS thin-film modules are manufactured on rigid glass substrates, which are not easily damaged during the mechanical scribing. Therefore, the industry still relies on the conventional mechanical scribing for P2 and P3 steps and laser is mostly used only for the P1 step.

Although laser processing can significantly increase the active area of the module but poorly optimised processing parameters generate additional paths for leakage current, which results in a decrease of the electrical solar cell parameters [7]. In most times the module efficiency of all-laser patterned modules falls behind the widely adopted mechanical scribing [6, 8].

The reason lies in that the laser scribing is based on the absorption of electromagnetic radiation in the material. This phenomenon contributes to the fast heating, melting, and, finally, the evaporation of the material. Unfortunately, not all laser-affected material is removed after the laser processing. Some of it remains at the edges of the ablated channels mostly as the partly evaporated and re-solidified material [66]. The decomposition temperature of complex, multi-component semiconductors (such as CIGS and CZTS) can be easily exceeded during the laser processing [67, 68]. It was shown that laser-induced thermal effects could lead to structural changes, the formation of electro-conductive phases causing the degradation of electrical properties [69, 70].

Therefore, precise optimisation and control of laser processing is not a simple task. It is crucial to minimise laser-induced damage in order to maintain high device efficiency.

### 2.7.3 Laser patterning: P1 step

The P1 process is the most straightforward of the three patterning steps. It is performed after the back-contact layer is deposited on the substrate. In the

case of a CIGS and CZTS technologies, molybdenum as a back-contact layer is almost solely used. P1 scribe completely cuts through the conductive layer ensuring high electrical isolation between individual cells. According to A. Burn, et al. [71] the resistivity of the high-quality P1 scribe should exceed  $20 \text{ M}\Omega \times \text{cm}$ . Morphologically, a high-quality laser-performed P1 scribe should produce a clean bottom of the P1 trench, a sharp rupture at the borders, a small heat-affected zone and minimal burr formation [71].

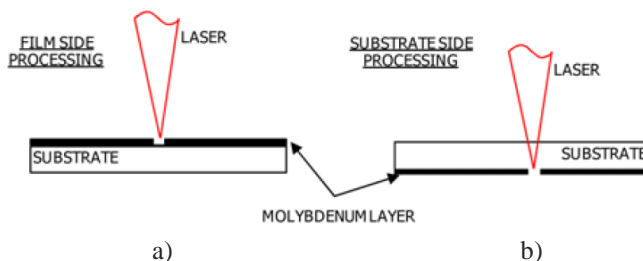


**Fig. 17.** Cross-section schemes of two possible P1 approaches from the film (a) and the substrate (b) sides [72].

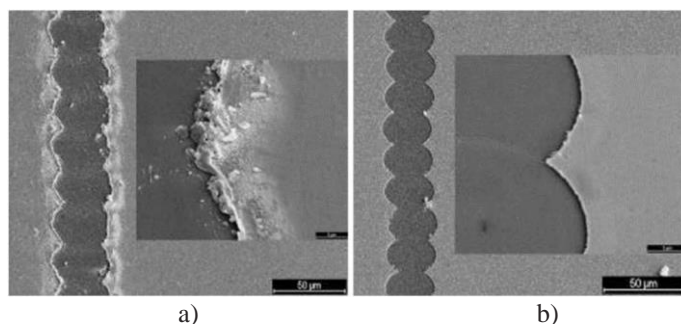


**Fig. 18.** SEM micrographs of typical laser processed P1 channels from the film side (a) and the substrate side (b). Inserts show magnified images of the channel edges. Scribes were made with a 10 ps, 1064 nm wavelength radiation emitting laser [71].

Depending on the type of the substrate, two P1 patterning approaches can be distinguished: molybdenum ablation from the film side (direct laser ablation), and the laser-induced molybdenum layer spallation from the substrate side (see Fig. 17). Both approaches can be realised on the substrates, which are transparent to the laser radiation, such as glasses [71]. In the case of opaque substrates (such as metal foils or polyimide substrates), only the film-side approach is possible. Usually, if a transparent glass is used as a substrate, then the molybdenum layer scribing takes place from the substrate side. The main benefits are that the ablation from the substrate side produces cleaner borders, channel bottoms, and smaller heat affected zone [71]. Typical P1 scribes produced from the film and the substrate sides are shown in Fig. 18a and b, respectively.

## 2.7.4 P2 processing step

The second scribing step is P2. It must ensure a reliable and low resistance contact between the molybdenum back-contact and the front contact of the cell [63]. A low resistance P2 connection keeps the resistive losses of the serial interconnection low maintaining high module efficiency. Most common P2 approaches are shown in Fig. 19 and briefly discussed in the following sections.

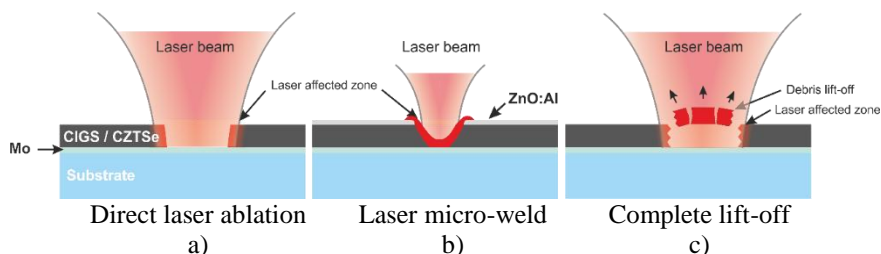


**Fig. 19.** Cross-section schemes of P2 laser scribing approaches. Mo back-contact exposure by direct ablation (a), laser-welding is used to metallise the resistive CIGS layer to act as a P2 interconnect (b), and Mo back-contact exposure by a laser induced CIGS lift-off (c).

### 2.7.4.1 P2 processing: direct laser ablation

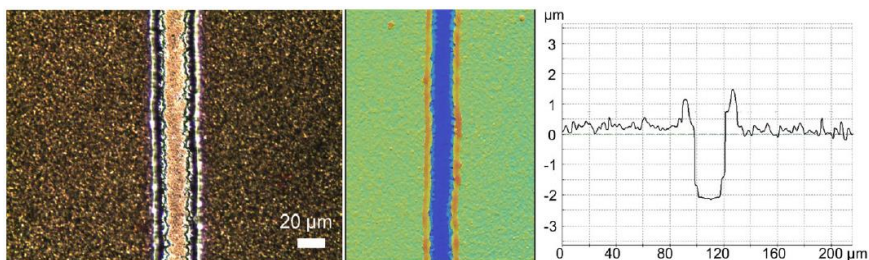


**Fig. 20.** P2 trench scribed in a CIGS solar cell with picosecond pulses. From left to right microscope image, confocal microscope image, and cross section profile [73].

Direct laser ablation of the CIGS material is a conventional approach to P2 laser processing (see Fig. 20). It is performed after the deposition of CIGS and buffer layers, but before the deposition of the TCO. The challenge is to find a suitable combination of laser pulse energy and pulse overlap (in the range of 90 %) to thermally evaporate buffer and CIGS layers down to the Mo back-contact in a layer-by-layer fashion [58]. Damage to the Mo layer must be avoided to ensure mechanically stable and low resistance contact with the TCO [63].

#### 2.7.4.2 P2 processing: complete lift-off

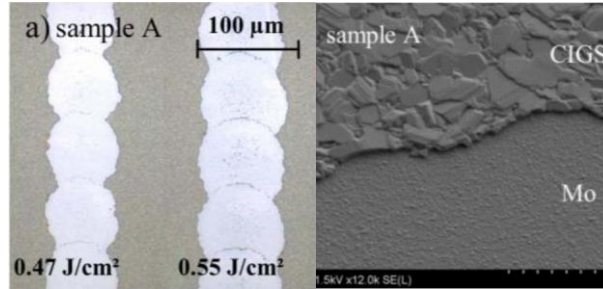


**Fig. 21.** Optical and SEM micrographs of P2 channels after the lift-off in a CIGS solar cell. Clean and damage-free molybdenum surface is exposed at the bottom of the trench [74].

A second P2 scribing approach is based on the laser-induced material lift-off process. Cross-section scheme and typical micrographs of complete lift-off P2 channels are shown in Fig. 19 and Fig. 21, respectively. P2 scribes based on the layer lift-off are usually performed after the deposition of absorber and buffer layers, but before the deposition of TCO.

It is considered that the material lift-off process enables to process the thermally sensitive films because all the laser affected material is mechanically removed from the laser ablation area. Therefore, the melting of the absorber layer around the laser-processed areas is significantly reduced or in some cases not even observed. The layer breaks away when the laser-induced stress exceeds its tensile strength. According to the literature, the layer lift-off is driven by (1) the fast expansion of the material; and (2) laser penetration and absorption at the interface of two layers [63, 75-77]. In the former case, the absorption of the laser energy induces a rapid thermally driven material expansion, which results in a significant stress build-up in the layer. In the second case, laser energy absorption at the inner interface between the layers triggers localised rapid temperature rise, which sublimates the interface. Stress build-up is generated by the formation and expansion of vapour gases under the confinement.

#### 2.7.4.3 P2 processing: laser micro-welding

Early experiments of the thin-film solar cell scribing showed that the laser heated CIGS could be transformed into a highly conductive compound. P.O. Westin first showed that the laser-transformed CIGS could act as P2 interconnect [78, 79].

A P2 micro-weld is performed on the finished solar cell stack after the TCO deposition. A laser patterning “welds” the front contact and CIGS layers along the scribe line [78].

The welded line provides electrical contact between the front contact of one cell and the back-contact of another. A typical laser micro-weld is shown in Fig. 22. The transformed area has the appearance of a welding bead. Large laser doses exceeding  $20 \text{ N}\times\text{J}/\text{cm}^2$  are required to transform CIGS absorber into a conductive compound [80]. However, laser fluence is usually kept below the ablation threshold of the CIGS layer in order to avoid the ablation of the absorber material.

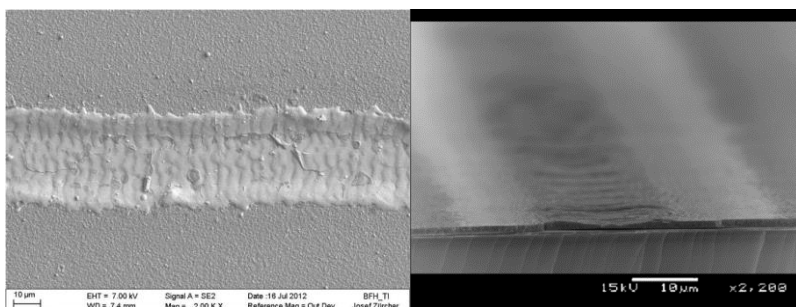


**Fig. 22.** SEM micrographs of laser micro-welds. TCO and CIGS layers are re-melted to form a connection between the TCO and the molybdenum back-contact [63, 79].

### 2.7.5 P3 processing step

The P3 process is the last step out of three used for formation of the series monolithic interconnection. It is performed after the deposition of TCO layer and is used to electrically isolate the front contact layer between adjacent cells [6]. Three different types of P3 processing are shown in Fig. 23 and briefly discussed in the following sections. For easier designation, P3 direct ablation and TCO lift-off will be mostly referred further in the text as the Type 1 and Type 2 scribing, respectively.

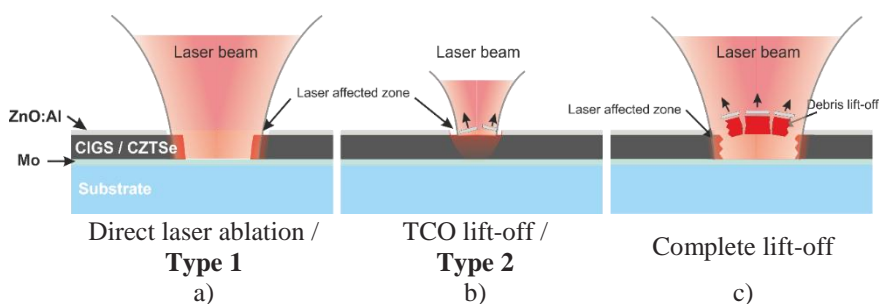


**Fig. 23.** Cross-section schemes of three P3 laser scribing approaches: (a) direct ablation, (b) TCO lift-off, and (c) complete lift-off.

#### 2.7.5.1 P3 processing: direct ablation and TCO lift-off

Historically, the P3 process involves the removal of the TCO, buffer, and absorber layer stack to expose the Mo back-contact via direct laser ablation in

a layer-to-layer manner as shown in Fig. 23a [63]. In general, this approach needs a reasonably high laser fluence (between 1 – 8 J/cm<sup>2</sup>, depending on the thickness of the layers) and pulse overlap of about 90 %. For this reason, scribing speed is limited to just several hundred mm/s for a laser system operating at 100 kHz pulse repetition rate. A typical directly ablated P3 channel is shown in Fig. 24a and c.

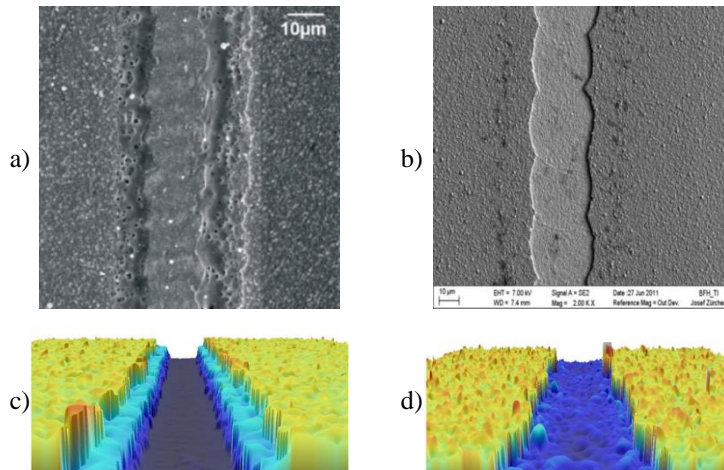


**Fig. 24.** SEM and confocal microscope images of P3 scribes made by the direct layer ablation (a, c), and TCO lift-off (b,d) in ZnO/CIS/Mo/SLG structure [63, 73, 81].

A second P3 approach is the TCO lift-off. As the name suggests, only the front contact layer is removed by the laser-induced material lift-off process which was discussed in detail in Section 2.7.4.2. This approach is used when the CIGS absorber has a sufficient layer resistance to ensure electrical isolation between the TCO's of two neighbouring cells. In this case, the laser fluence is significantly reduced so that the absorber layer stays intact and only the top contact layer is removed. It is a low pulse overlap process (20 – 40 %), so scribing speeds above 1 m/s can be easily achieved with a conventional 100 kHz laser. Laser fluence required to initiate a TCO lift-off depends on the thickness of the layer, however, based on our experience, it is roughly 5 to 10 times smaller compared to the P3 scribing by direct layer ablation. A typical TCO lift-off channel is shown in Fig. 24b and d.

### 2.7.5.2 P3 processing: complete lift-off

A complete lift-off approach for the P3 step attracted much attention among research groups for the possibility to avoid melting of the absorber layer in the vicinity of the scribed trench [74, 77, 82, 83]. This method includes the spallation of TCO, buffer, and absorber layers down to Mo with a single laser pulse. It is a low-pulse-overlap process (20 – 40 %), so scribing speeds above

1 m/s can be easily achieved with a conventional 100 kHz laser. Cross-section scheme is presented in Fig. 23c, while SEM micrographs of complete lift-off P3 channels are presented in Fig. 25. The material is removed mostly in the solid phase by laser-induced layer spallation, which driving mechanisms were discussed in Section 2.7.4.2.

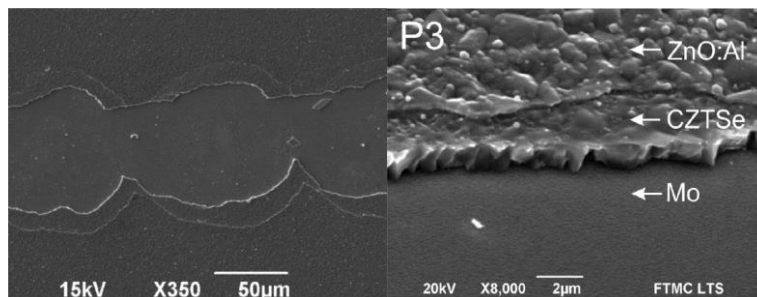


**Fig. 25.** SEM micrographs of P3 complete lift-off scribes in Al:ZnO/i-ZnO/CdS/CZTSe/Mo/SLG structure [70].

## 2.8 Laser scribing of thin-film solar cells reported in the literature

One of the first papers reporting the electrical measurements of the laser processed CIS thin-film mini-modules was reported by J. Hermann et al. [84]. In this paper, nanosecond and femtosecond pulses were used to cut through the active layers of the solar cell followed by the measurement of the I-V curves shown in Fig. 26. Electrical measurements revealed that processing with nanosecond pulses had shunted the device: the efficiency before and after the laser processing dropped from 6.8 % to 0.4 %. On the contrary, processing with femtosecond pulses retained device's photovoltaic efficiency with minimal losses. The I-V measurements revealed an insignificant efficiency drop from 6.8 % to 6.6 %. Authors deduced two phenomena why nanosecond pulses were responsible for the low device efficiency: (1) residues of melted Mo layer projected to the sidewalls of the ablated channel and (2) the metallization of CIS semiconductor shunting the device [84]. These phenomena can be observed during both the nano- and femtosecond processing. However, they are significantly more pronounced during the nanosecond pulse processing due to the longer laser-matter interaction.

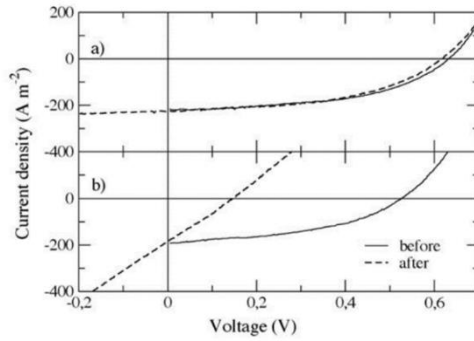


**Fig. 26.** Solar cells current density versus applied voltage measured before and after the laser processing with femtosecond (a) and nanosecond (b) pulses [84].

Most of the recent investigations on the P1, P2, and P3 laser scribing of thin-film solar cells concentrate on processing with ultrashort pulsed lasers (pico- and femtosecond pulse durations) [6, 58, 63, 73, 81]. Many authors concluded that laser irradiation of CIGS solar cells results in laser-induced material modifications such as excess melt formation on the sidewalls of the channel and heat affected zones (HAZ) [60]. The amount of melted CIGS strongly depends on the laser pulse duration. Ultrashort pulses can reduce melting of the CIGS, but it cannot be avoided entirely even when the femtosecond pulses are applied [81, 84, 85]. This is due to the low melting temperature of the CIGS absorber (between 1260 K and 1313 K), which is easily exceeded during the laser processing [86]. Despite that, mini-modules processed with ultrashort pulses showed similar efficiencies compared to mechanically produced counterparts [60, 73, 87].

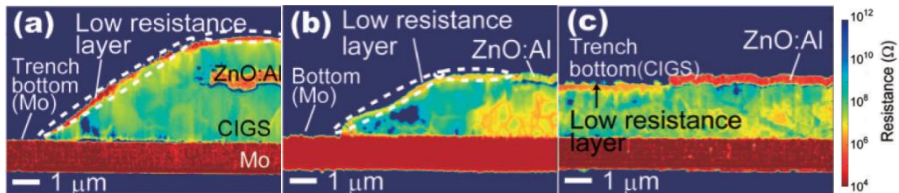


**Fig. 27.** SSRM images of the laser scribed trenches in CIGS solar cell (cross-section views). Processing parameters: (a) a P3 Type 1 channel ablated with 10  $\mu\text{J}$  pulses and 94 % pulse overlap, (b) a P3 Type 1 channel ablated with 2  $\mu\text{J}$  pulses and 83 % pulse overlap, and (c) a P3 Type 2 channel ablated with 2  $\mu\text{J}$  pulses and 20 % pulse overlap [60].

A. Narazaki et al. [60] performed scanning spreading resistance microscopy imaging (SSRM) on the cross-sections of the P3 scribes processed with a femtosecond laser (see Fig. 27, the electrical resistance is mapped and represented by the colour). SSRM images revealed that only a thin front layer of CIGS, which was melted and re-solidified, was of lower resistance compared to the non-irradiated CIGS. Authors also showed that the resistivity

of laser affected areas depended on the laser pulse energy and the pulse overlap. Large doses irradiated into the solar cell could significantly shunt the device even when femtosecond pulses were applied.

Gečys et al. [88] found that the laser pulse duration effect was most expressed when a few high-energy pulses were used to ablate CIGS absorber. However, when the number was increased to several tenths of pulses with lower energy, the melted area percentage around the exposed Mo layer with the total width of the ablated crater became almost identical for both femtosecond (320 fs) and picosecond (16 ps) pulses.

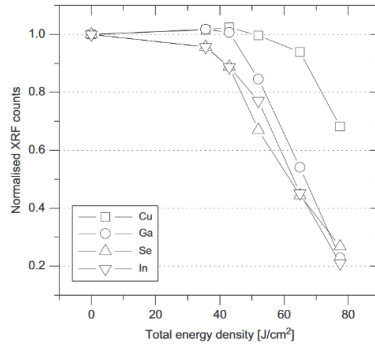


**Fig. 28.** XRF results showing relative changes in element content in CIGS after treatment with nanosecond pulses [79].

Other research groups concentrated on the investigation of the nanosecond pulse processing effects to the absorber material. P.-O. Westin et al. [79] investigated the composition of the CIGS versus the irradiated laser dose (total energy density). X-ray fluorescence (XRF) measurements showed that In and Se content dropped at lower nanosecond laser doses than Ga and Cu (see Fig. 28) [79]. In other words, copper-rich and selenium-poor phases transformed CIGS into a highly conductive compound. P.O. Westin et al. [78, 79] first showed that the locally laser-transformed CIGS could act as P2 interconnects. Authors estimated the P2 laser micro-weld specific resistivity of  $0.5 \Omega \times \text{cm}$ , which was comparable to that achieved in a typical mechanically patterned modules and showed reasonable results regarding the device efficiency [78, 79].

K. Stelmaszczyk et al. [89] showed that the laser-induced modifications in a CIGS absorber layer does not end at the edge of the HAZ, but expands much further. He performed P2 laser micro-welding in a fully working CIGS cell with a nanosecond laser. SEM microscopy showed that visual modifications spanned  $30 \mu\text{m}$  from the edge of the scribe in a direction perpendicular to the scribe. However, Raman and photoluminescence (PL) measurements revealed

that CIGS modifications were observed even at 100  $\mu\text{m}$  from the edge of the P2 scribe (see Fig. 29) [89].

Complete lift-off processing of thin-film solar cells with nanosecond pulses attracted much attention among many research groups [74, 77, 82, 83].

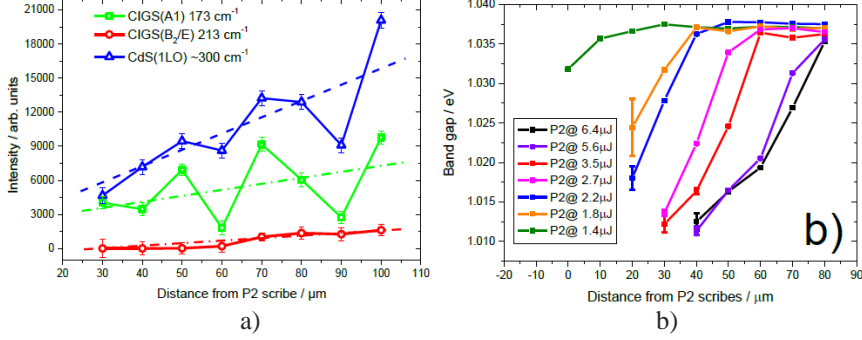


**Fig. 29.** Measured intensities of the CIGS and CdS mode Raman peaks versus the distance from the P2 scribe (a). CIGS bandgap dependence on the distance from the P2 scribe edge for different pulse energies (b). Both images were borrowed from [89].

## 2.9 Theory of light-material interaction

When the light strikes the surface of the material, the interaction between the electromagnetic waves and the matter takes place. During this interaction, several events might happen: the light might be reflected from the sample's surface, transmitted through the sample, absorbed in its volume, or diffusely scattered [90]. Laser ablation of CIGS cells is a light-matter interaction. In this chapter, interaction of electromagnetic waves with the matter is briefly discussed.

A plane electromagnetic wave can be described by the following equation [91]:

$$\vec{E}(\vec{r}, t) = E_0 \exp\{i(\vec{k}\vec{r} - \omega t)\}, \quad (9)$$

where the  $\omega$  is the angular frequency of the wave,  $\vec{k}$  is called the wave-vector, coordinate vector is  $\vec{r}$  and  $t$ ,  $E_0$  being time and electromagnetic field amplitude, respectively. According to the Lorentz model, the material can be treated as a combination of harmonic oscillators. Hence the motion equation for electrons in an electromagnetic field is defined as follows [90]:

$$m \frac{d^2 \vec{r}}{dt^2} + m\gamma \frac{d\vec{r}}{dt} + m\omega_0^2 \vec{r} = -e\vec{E}_{loc}(\vec{r}, t), \quad (10)$$

where  $m$  is the electron mass,  $\gamma$  is the attenuation of electron oscillations,  $\vec{E}_{loc}$  is the local field strength, and  $\omega_0$  being the angular frequency of the electromagnetic wave. The dielectric tensor  $\epsilon$  couples the locally acting electric field  $\vec{E}_{int} = \langle \vec{E}_{loc} \rangle$  to an external electric field:  $\vec{E}_0 = \epsilon \cdot \vec{E}_{int}$ . If the matter

is absorptive, then the dielectric tensor can be separated into real and imaginary parts:

$$\varepsilon = \varepsilon_1 + i\varepsilon_2, \quad (11)$$

which are equal to  $\varepsilon_1 = n^2 - \kappa$  and  $\varepsilon_2 = n\kappa$ . Here, the refractive index  $n$  and extinction coefficient  $\kappa$  characterize the refractive and absorptive properties of the material, respectively.

When the light is incident to the surface of the material, part of the light will be reflected based on the reflectivity coefficient  $R$  [92]. If the incident light is normal to the surface of the material, then the reflection will be:

$$R = \frac{(n_1 - n_2)^2 + (\kappa_1 - \kappa_2)^2}{(n_1 + n_2)^2 + (\kappa_1 + \kappa_2)^2}. \quad (12)$$

Here, index 1 denotes the surrounding media and 2 - the incident material. The rest of the light, which was not reflected, will be transmitted into the material.

According to the Beer-Lambert law, the light inside the material will decay exponentially with the depth  $z$  at a rate determined by the material's absorption coefficient  $\alpha$  [93]:

$$I(z, t) = (1 - R)I_0(t)e^{-\alpha z}, \quad (13)$$

where  $I$  is the remaining light intensity and  $I_0$  is the initial intensity of light falling on the sample's surface [93]. Absorption coefficient  $\alpha$  is related to the extinction coefficient  $\kappa$  and  $\lambda$  is the wavelength of light:

$$\alpha = \frac{2\omega\kappa}{c} = \frac{4\pi\kappa}{\lambda}. \quad (14)$$

Absorbed laser energy heats the material. If the laser spot size is considered to be much larger than the thermal diffusion length  $z_{th} = \sqrt{\tau k_e / C_p}$ , then the heat transfer equation can be simplified to one-dimensional to evaluate the temperature field distribution in the material:

$$\rho C_p(T) \frac{dT(z, t)}{dt} - \nabla(k_e(T)\nabla T(z, t)) = Q(z, t), \quad (15)$$

where  $\tau$  is laser pulse duration,  $k_e$  is the heat conductivity,  $C_p$  is the specific heat,  $\rho$  is the material density.  $Q$  is the heat source (in this case, absorbed laser energy), which can be considered as the sum of the absorbed laser energy (13) and the heat sink  $\Delta U(z, t)$  for phase transition:

$$Q(z, t) = I(z, t) + \Delta U(z, t). \quad (16)$$

Temporal shape of the laser beam can also be considered. In most cases, it is convenient to use a Gaussian temporal shape, which can be described by the following equation [91]:

$$I(t) = I_p \exp(-4\ln 2(t/\tau)^2), \quad (17)$$

where  $I_p$  is the maximum intensity, and  $\tau$  is the full width at half-maximum pulse duration.

## 3 EXPERIMENTAL SETUPS, PROCEDURES, AND MATERIALS

### 3.1 Laser sources

In the course of this thesis, a range of laser parameters was varied to thoroughly investigate the laser-patterning processes in CIGS and CZTSe thin-film solar cells. For this task, multiple laser sources were utilised: four picosecond, one femtosecond, and one nanosecond lasers. Summary of the laser sources used in the experiments is presented in Table 2 and briefly discussed below.

**Table 2.** Parameters of the laser systems used in thin-film solar cell patterning.

Laser	Atlantic 15 W	Atlantic HE	Atlantic 1342	Atlantic 60 W	Pharos	NT277
Wavelength, nm	1064, 532, 355	1064	1342	1064, 532	1030	2500
Pulse duration, ps	13	60	13	13	0.3-20	6000
Repetition rate, kHz	500	1	300	1000	500	1
Beam/sample positioning	Galvo	XY axes	XY axes	Galvo	XY axes	XY axes
Focal length of objective, mm	80	50	50	80	50	50

Picosecond lasers (13-60 ps pulse duration) used in the experiments were diode pumped lasers based on the Nd:YVO<sub>4</sub> laser gain medium. Two emission wavelengths of the Nd:YVO<sub>4</sub> crystal were used: 1064 nm and 1342 nm. Atlantic HE, Atlantic 15W, and Atlantic 60W lasers produced the former fundamental wavelength, while the Atlantic 1342 produced 1342 nm laser output [94]. In some experiments, second (532 nm) and third (355 nm) harmonics of the 1064 nm laser were used.

A femtosecond laser Pharos (pulse duration 300 fs – 20 ps) was based on Yb:KGW laser medium exhibiting 1030 nm wavelength radiation. The output pulse duration was tuned by an integrated compressor employing two transmission diffraction gratings.

For nanosecond pulses, an NT277 laser (based on the Nd:YVO<sub>4</sub> laser gain medium) was utilised providing 6 ns length pulses at 1 kHz pulse repetition rate. Laser included an integrated optical parametric oscillator (OPO) to obtain 2.5 μm wavelength radiation in the mid-infrared region.

Finally, the output of all laser sources had a similar to Gaussian beam intensity distribution.

### 3.2 Optical setups

Laser scribing experiments were realised using three basic setups presented in Fig. 30. Each setup consisted of a laser, a beam expander, and several folding mirrors directing the laser beam to the scanning system. In the case when a laser did not have an internal laser power attenuator or harmonic modules, an external solution was used: a half-wave plate and a polariser to attenuate the power, and non-linear crystals to convert the laser wavelength.

Scribing experiments were realised either by scanning the laser beam over the sample surface or by moving the sample in respect to the laser beam. Optical system No. 1 consisted of a galvanometer scanner (from ScanLab), which was used with 80 mm focusing telecentric f-theta lens (shown in Fig. 30b). Individual systems for 355 nm, 532 nm, and 1064 nm wavelengths were built. Sample positioning along the direction of the laser beam was conducted by a motorised Z-axis (from Standa).

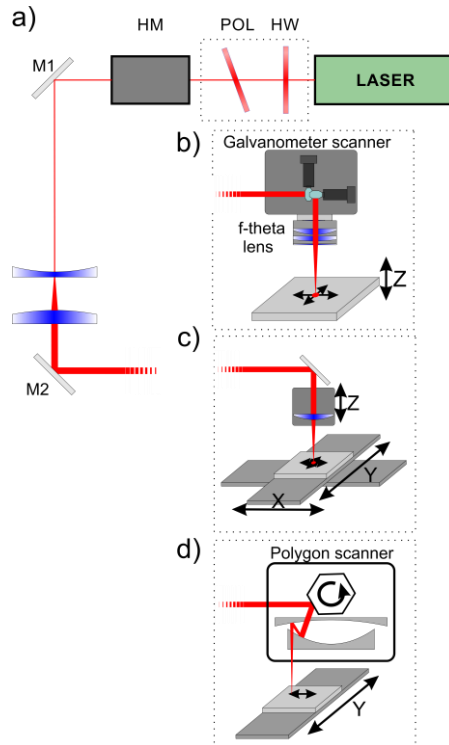


**Fig. 30.** Laser scribing setups: (a) base components common for used laser systems; (b) galvanometer scanner setup; (c) setup with XYZ linear stages; (d) polygon scanner setup. HW – half-wave plate, POL – polariser, HM – harmonics module, M – mirror.

The second setup (No. 2) is presented in Fig. 30c. This setup included the linear XYZ translation stages (from Aerotech) with a 50 mm focusing objective. This setup was used with 1342 nm and 2.5  $\mu\text{m}$  wavelengths. The

objective was mounted on the Z stage, and the sample was tightly fixed to the XY stages.

The last setup (No. 3, see Fig. 30d) included a 1-dimensional polygon scanner LSE170 (from Next Scan Technology) and a linear translation axis. In order to realise a 2-dimensional (XY) scanning, a linear axis was positioned perpendicularly to the scanning direction of the polygon scanner. A laser beam was focused with a 190 mm focal length f-theta mirror-based objective.

### 3.3 Morphological, topographical and elemental analysis

The visual quality of laser-processed samples was analysed with an optical microscope (BX51, Olympus) and the scanning electron microscope (SEM) JSM-6490LV from JEOL. Elemental analysis of the samples was carried out by energy-dispersive X-ray spectroscopy (EDS) from Oxford instruments.

### 3.4 Thin-film solar cell samples

All experiments were conducted in CIGS and CZTSe based thin-film solar cells, which were kindly provided by the Solarion AG (Germany), EMPA (Switzerland), and NREL (USA). CIGS and CZTSe technologies share the same layer deposition processes and order of deposited layers, basic structure, and have similar layer thicknesses. Experiments presented in this thesis were done on a number of CIGS ( $\text{Cu}(\text{In,Ga})\text{Se}_2$ ) and CZTSe ( $\text{Cu}_2\text{ZnSnSe}_4$ ) cells. For clarity, solar cell samples were assigned to a specific number ranging from 1 to 5 (see Table 3 and Fig. 31). CIGS experiments were performed only on fully functioning cells comprised of a substrate, back-contact, absorber, buffer layer, and TCO. Experiments on CZTSe solar cells were conducted on two types of cells: (1) a fully functioning cells, and (2) partial cells without the TCO and buffer layers.

**Table 3.** CIGS and CZTSe samples used in the experiments.

No.	Solar cell type	Scribe type	Layer thickness, $\mu\text{m}$				
			TCO	CdS	Absorber	Mo	Substrate
1	<b>CZTSe/Mo/SLG</b>	P2	-	-	<b>1.3</b>	1	1000
2	Al:ZnO+i-ZnO/CdS/ <b>CZTSe/Mo/SLG</b>	P3	0.25	0.05	<b>0.8</b>	1	1000
3	Al:ZnO+i-ZnO/CdS/ <b>CZTSe/Mo/SLG</b>	P3	0.25	0.05	<b>1.3</b>	1	1000
4	Al:ZnO+i-ZnO/CdS/ <b>CIGS/Mo/SLG</b>	P3	0.8	0.05	<b>2.0</b>	1	1000
5	Al:ZnO+i-ZnO/CdS/ <b>CIGS/Mo/Pi</b>	P3	0.35	0.05	<b>2</b>	0.5	25

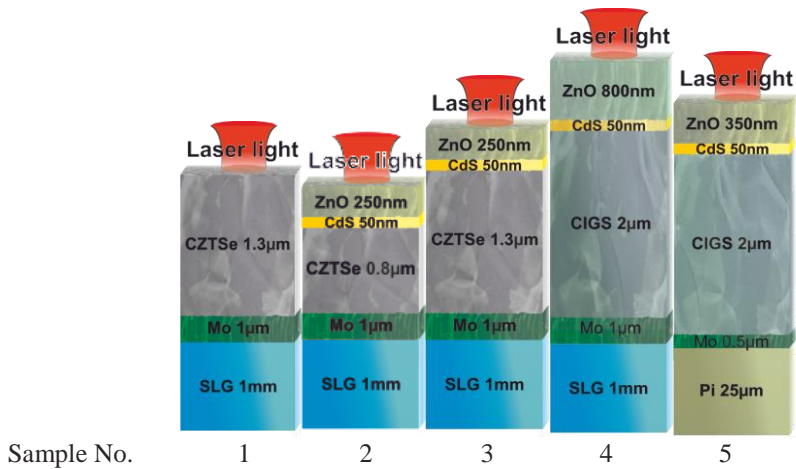


**Fig. 31.** CIGS and CZTS solar cell samples used in the experiments.

### 3.5 Raman analysis

Raman spectroscopy is used to detect substances, provide information on chemical structures and physical forms from the acquired characteristic spectral patterns [95]. Monochromatic light is used to irradiate the samples and excite molecules from the ground state into the virtual state determined by the frequency of the incident light. Shortly after, the excited molecule re-emits the photon of either the unchanged, lower or higher energy than the incident photon. These photons are identified as Rayleigh, Stokes, and anti-Stokes, respectively.

Raman spectroscopy is based on the detection of the inelastic scattering of incident photons. Usually, Stokes scattering is recorded, since the signal intensity is much higher compared to anti-Stokes [95].

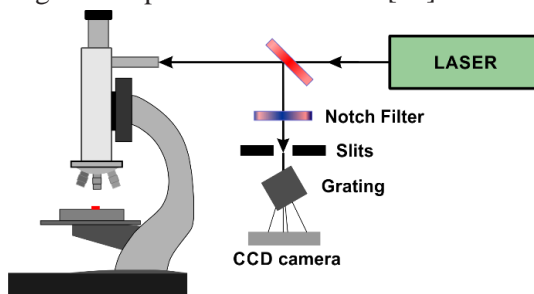


**Fig. 32.** Typical Raman microscope consisting of the microscope, laser, notch filter, a grating, and a CCD detector. Picture adapted from [95].

Characterisation of the thin-films was carried out by a micro-Raman microscope (nVia Renishaw). In this setup, the 633 nm laser was used as a narrow linewidth light source. A laser clean-up filter was used to remove any background and emission lines other than the main excitation line of the laser

[96]. A 180° scattering geometry setup was used. Here, the same lens system was used for both, the delivery (and focusing) of the laser beam onto the sample and collecting back the scattered light. A notch filter was used to remove much more intense Rayleigh scattering. Finally, the light passed into the monochromator and a CCD detector. The spot size and the spatial resolution were estimated to be 1  $\mu\text{m}$  and 0.5  $\mu\text{m}$ , respectively. Excitation laser power was set to 1 mW, and every Raman spectrum was accumulated for 100 s.

### 3.6 Direct measurement of solar cell electrical characteristics

Dual channel source meter (Keithley 2602A) was used to measure solar cell's electrical characteristics. Electrical measurements were applied in dark conditions by placing the samples in a light-tight enclosure (see Fig. 33). The dark characteristics provide useful information about the quality of the p-n junction and the grid and contact electrical resistance [97].

Measurements were applied between laser patterning steps without removing the measurement probes. The laser beam was introduced into the enclosure through the port at the top of the box (see Fig. 33). The port was closed during electrical measurements. I-V curves were obtained by applying stepped voltage and measuring the current flowing through a solar cell. A small voltage range was measured in a region where the current and voltage dependence was linear. Parallel resistance of a solar cell was extracted from the I-V plots.

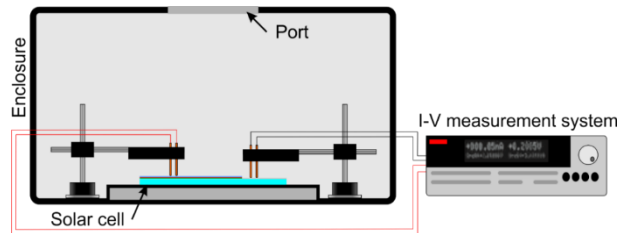


**Fig. 33.** Apparatus for the measurements of the in dark solar cell electrical properties.

### 3.7 Nested circular laser scribing technique

Reliable and fast laser processing quality evaluation is a crucial point for a highly efficient PV device. A Nested Circular Laser Scribing Technique (NCLST) was used to optimise laser scribing parameters. It is one of a few fast techniques, which require minimal sample preparation and can be carried out on a fully working solar cell [98]. NCLST technique provides the solar cell areal conductivity, information about localised defects, and laser scribe conductivity.

The NCLST procedure consists of the experimental setup for in-process measurements and a fitting model for evaluation of the electrical shunts. At first, electrodes of the I-V measurement system are connected to the back and front-contacts of the solar cell as shown in Fig. 34a. Then, the pre-patterns are made around the front-contact wire (two dotted lines, Fig. 34a). The solar cell cannot be ablated if the wire covers it; therefore, pre-patterns are used to complete a laser scribed circle and electrically isolate the laser enclosed area from the outer area.

Afterwards, a laser, with pre-selected processing parameters, is used to pattern concentric circles in the solar cell structure. Scribing is started with the outermost circle and with each consecutive laser scribe, the radius of the circle is reduced. This way, smaller and smaller enclosed area can be electrically isolated from the outside.

Parallel conductance measurements are applied between the scribes in the “scribe and measure” manner. The procedure is repeated multiple times to obtain a relationship between the parallel conductance of the isolated area and the laser scribe radius. A typical NCLST measurement result is presented in Fig. 34b [98].

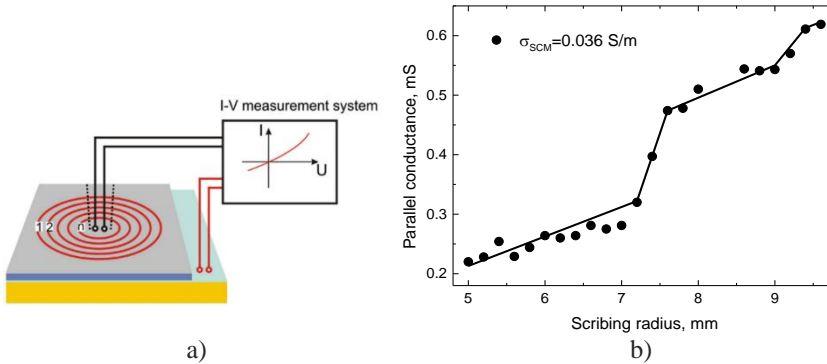


**Fig. 34.** Experimental setup of Nested circular laser scribing technique for in-process parallel conductance measurements (a); and a typical result of the NCLST measurement (b). Pictures adopted from [98, 99]

**Table 4.** NCLST fitting function parameters.

Parameter	Meaning
$G_p$ , S	Parallel conductance of the solar cell
$\sigma_{SCA}$ , S/m <sup>2</sup>	Cell areal conductivity
$\sigma_{SCM}$ , S/m	Laser scribe conductivity
$\sigma_{ID}$ , S/m	Conductivity of a localised defect $i$
$w_d^{ID}$ , mm	Size of a defect
$r^{ID}$ , mm	Distance to a defect centre

The proposed model considers parallel conductance as the sum of the contributions of the solar cell area, laser damage, and intrinsic defects. The measured conductance values should be plotted against the corresponding radius of the scribed circle, and fitted with proposed fitting function [98]:

$$G_p = \pi\sigma_{SCA}\cdot r^2 + \sigma_{SCM}\cdot r + \sum_i \left[ \iint_r \sigma_{ID} \frac{1}{w_d^{ID}} \cdot \exp\left(-\frac{1}{2} \cdot \left(\frac{r-r^{ID}}{w_d^{ID}}\right)^2\right) dA_{SC} \right], \quad (18)$$

here  $i$  represents the number of localised defects,  $r$  is the radius of the scribed circle, and  $A_{SC}$  is the enclosed solar cell area. The first member of the function stands for areal conductance of CIGS solar cell, and second – for laser-induced parallel conductance. The third member depicts the conductance caused by the localised initial defects, such as parasitic shunts and weak diodes [5]. Each of the function components (members) depend on the radius of the last scribed circle. The serial resistance of the top-contact is neglected assuming that the solar cell's parallel resistance  $R_p$  is much larger than the serial resistance  $R_s$  of TCO ( $R_p \gg R_s$ ). Fitting function parameters are explained in Table 4. Number, conductivity, or precise position of such defects is not investigated in the model, but they are considered as a sum of all initial defects enclosed in the particular circle  $n$  [98, 100].

### 3.8 Linear laser scribing technique

The NCLST technique turned out to be not always reliable when working with solar cells with a higher parallel conductance [99]. Secondly, having a large number of fitting parameters complicated the interpretation of the results.

Therefore, a new technique was developed based on NCLST approach and ideas reported in [101]. Short and straight lines were scribed instead of circular patterns. Scribes were positioned close to measurement probes, minimising the error of the measurements. We renamed the simplified technique to Linear laser scribing technique (LLST) and used it extensively in [66, 80, 99].

The LLST approach consists of pre-selected laser processing parameters used to ablate open contour patterns of defined length in a solar cell structure (see Fig. 35a). Considering that the solar cell's area is significantly larger than the area of the scribes, the LLST scribing geometry (straight lines) does not change the area of the solar cell or the number of defects enclosed in that area. For these reasons, the first member (areal conductance) of the complex NCLST fitting function (18) is considered constant during the LLST experiment, and the third fitting function member (conductance caused by initial defects) is neglected. This way, the variation of the solar cell's parallel conductance during the LLST experiment is influenced only by the laser scribing:

$$\Delta G_p = \sigma_{SCM} \cdot l. \quad (19)$$

Here, the  $\Delta G_p$  is the variation of the cell's parallel conductance,  $\sigma_{SCM}$  is the laser scribe conductivity and  $l$  represents the length of the scribe.

As previously, LLST experiment consists of the measurements of the parallel conductance performed between the laser scribes. This way, after just several scribing and measurement procedures, a relationship between the laser scribe length and cell's parallel conductance is obtained. Data points are plotted against the laser scribe length and fitted with function (19).

A typical LLST measurement plot is presented in Fig. 35b. The LLST measurements can be applied multiple times on the same sample as long as the previous measurements are electrically isolated from the laser non-affected area. For example, the TCO/CdS/CIGS layers can be peeled off with a sharp blade around the laser scribes.

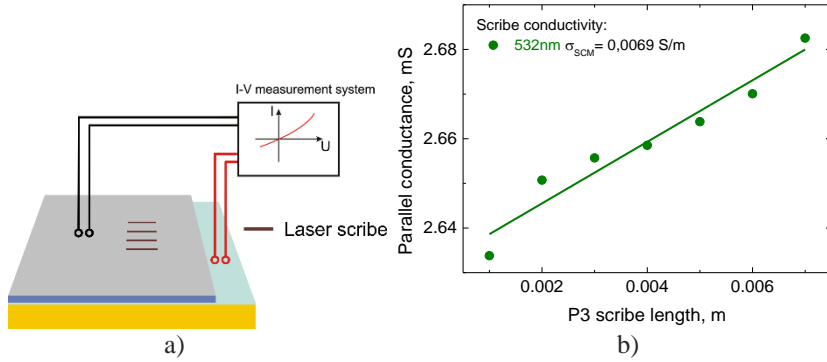


**Fig. 35.** Experimental setup of the LLST technique for in-process parallel conductance measurements (a); and a typical result of the LLST measurement (b).

### 3.9 Serial interconnect simulations

Simulations of the thin-film mini-module efficiency were conducted to estimate the efficiency degradation related to the laser-induced variation in solar cell's parallel conductance. Solar cell efficiency simulations were based on a classical Shockley equation for a Schottky diode (4) introduced in Section 2.4. The latter equation is commonly used to describe the current-voltage relationship of a solar cell when simulating solar cell's behaviour.

Two cases were simulated: mini-module efficiency versus (a) P2 interconnect conductivity, and (b) P3 isolation scribe conductivity. Standard Test Conditions were included in the model: mini-module temperature fixed at 25 °C and irradiance of 1000 W/m<sup>2</sup>.

**Table 5.** Electrical parameters for CIGS and CZTSe mini-module simulations.

Parameter	Solar cell		
Solar cell	#1 [102]	#2 [103]	#3 [104]
Absorber	CIGS	CIGS	CZTSe
Number of cells	1	8	1
$V_{oc}$ (mV)	746	5500	408
$J_{sc}$ (mA/cm <sup>2</sup> )	36.6	31.3	38.9
$J_0$ (A/cm <sup>2</sup> )	$2.4 \cdot 10^{-11}$	$4.74 \cdot 10^{-11}$	$1.6 \cdot 10^{-6}$
$\eta$	1.38	1.45	1.54
A (cm <sup>2</sup> )	0.497	1.57 (per cell)	1
$R_s$ $\Omega \cdot \text{cm}^2$	0.32	2.84	1.44
$R_p$ $\Omega \cdot \text{cm}^2$	1750	395	3130
FF (%)	79.3	61.2	61.4
$\eta_{eff}$ (%)	21.7	13.2	9.7

### 3.9.1 Mini-module efficiency versus P2 scribe conductivity

In the case of a laser P2 micro-welding, a serially interconnected PV array (shown in Fig. 36) mathematically was treated as a single solar cell. It is true if we introduce an average serial resistance  $R_{ave}$  representing a series resistor  $R_s$ , laser weld resistor  $R_{pl}$ , and a number of serially interconnected cells -  $N_s$ .

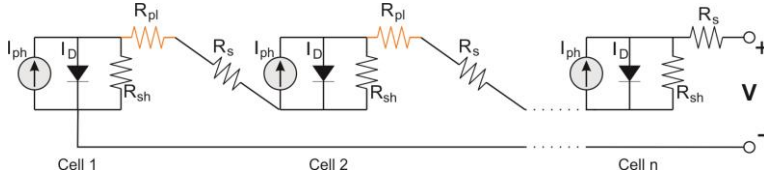


**Fig. 36.** Equivalent circuit of an n-cell mini module interconnected in series. The case of P2 laser process.

Considering that the  $R_s$  is connected with the  $R_{pl}$  in series, the average serial resistance  $R_{ave}$  was expressed as follows:

$$R_{ave} = \frac{N_s R_s + (N_s - 1) R_{pl}}{N_s}, \quad (20)$$

$$R_{pl} = \rho / L_{weld}, \quad (21)$$

where  $\rho$  is the experimentally obtained laser P2 weld resistivity and  $L_{weld}$  is the laser micro-weld length. The P1 and P3 scribes were assumed of infinite resistance and, therefore, neglected in the model. Only the P2 weld conductivity was varied. Taking everything into account, the final form of the equation (4) was transformed to:

$$I = J_{sc} A \frac{I_r}{I_{0,r}} - I_0 \left( e^{q(V/N_s + IR_s)/\eta k T} - 1 \right) - \frac{V/N_s + IR_{ave}}{R_{sh}}. \quad (22)$$

Maple software was used for P2 conductivity simulations.

### 3.9.2 Mini-module efficiency versus P3 scribe conductivity

In the case of P3 scribing, the equivalent circuit of an n-cell mini-module is shown in Fig. 37. Here, laser scribed P3 channels induced additional shunts, which are marked as  $R_{P3}$  resistors. A PSpice modelling software was used for simulations.

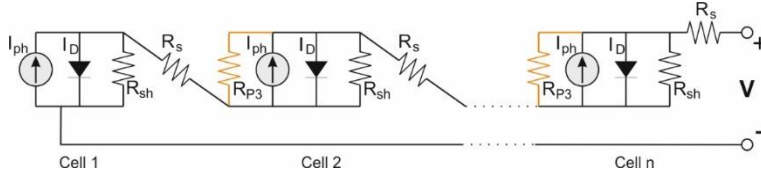


**Fig. 37.** Equivalent circuit of an n-cell mini module interconnected in series. The case of P3 laser process.

In the model, each solar cell (comprising a mini-module) was implemented as a separate sub-circuit and was described by the Shockley equation for a Schottky diode (4). The influence of P1 and P2 scribes were neglected in the model by considering that the P1 and P2 scribes were of infinite resistance and infinite conductivity, respectively. The laser-induced shunt resistance variation was implemented into the I-V equation considering that the resulting parallel resistance of the solar cell was comprised of an initial and P3 laser scribe shunts connected in parallel:

$$\frac{1}{R_p} = \frac{1}{R_{sh}} + \frac{1}{R_{P3}} = \frac{1}{R_{sh}} + \frac{L_{scribe}}{\rho} \quad (23)$$

### 3.10 Modelling of the energy coupling in thin-film solar cells

A numerical analysis was carried out in order to find the temporal evolution of temperature distribution in a thin-film solar cell after the laser-matter interaction. A one-dimensional (1D) light and heat propagation model was used since only the small central area of the laser-irradiated spot was simulated.

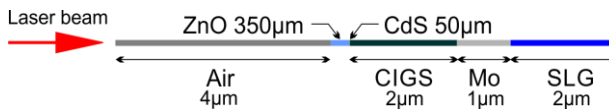


**Fig. 38.** A 1D CIGS computational cell scheme.

A thin-film solar cell was represented by a 1D computational cell (see Fig. 38). Electromagnetic wave entered the structure from the top-contact side normal to the surface of the cell. Additional 4  $\mu\text{m}$  thick layer of air was included in the model just before the top-contact. Laser energy coupling was determined by numerically solving the Helmholtz equation, which took into account absorption and reflection of electromagnetic waves:

$$\frac{d^2\vec{E}}{dz^2} + k_0^2 \tilde{n}\vec{E} = 0, \quad (24)$$

where  $\vec{E}$  is the electric field of the electromagnetic wave,  $z$  is the radiation penetration depth,  $k_0 = \frac{2\pi}{\lambda}$  is the wave number, and  $\lambda$  is the wavelength. The complex refractive index is given by  $\tilde{n} = n_0 + i\kappa$ , where  $n_0$  is the real part of the refraction index, and  $\kappa$  is the extinction coefficient. Solution to the equation (24) was the power loss density of electromagnetic wave [105]:

$$Q = \frac{1}{2} \omega \varepsilon_2 |\vec{E}(\omega)|^2. \quad (25)$$

Absorbed laser energy resulted in the heating of the material. The temperature field was calculated by using the heat transfer equation (15). A single pulse heating was represented by the Heaviside step function  $H(\tau - t)$  paired with the heat source  $Q$ , where  $\tau$  is the laser pulse duration. The latter function represented the rectangular laser pulse temporal shape. Lateral energy losses and material phase change were excluded from the model. The initial temperature was set to 273 K. In these simulations, the optical and thermophysical properties of materials were assumed to be temperature independent. Material parameters were obtained from multiple sources and presented in Table 6. The lack of wavelength dependent material parameters (extinction coefficient and refractive index) forced to use the closest found values.

**Table 6.** Material parameters used in CIGS simulations.

	Al:ZnO [106, 107]	CdS [108-110]	CIGS [111-113]	Mo [109, 114, 115]	Glass [116]
$\rho$ (g/cm <sup>3</sup> )	5.61	4.82	4.6	10.2	2.5
$C_p$ (J/(g·K))	0.5	0.47	1	0.18	0.72
$\kappa$ (W/(m·K))	65	20	3	143	1
$n_{355\text{nm}}$ , $k_{\text{ext}355\text{nm}}$	2.3, 0.23	2.49, 0.95	2.63, 1.02	3.06, 3.21	-
$n_{532\text{nm}}$ , $k_{\text{ext}532\text{nm}}$	1.43, 0.004	2.72, 0.7	3.02, 0.54	3.79, 3.61	-
$n_{1064\text{nm}}$ , $k_{\text{ext}1064\text{nm}}$	1.41, 0.06	2.28, 0.37	3.02, 0.22	2.44, 4.22	-
$n_{1342\text{nm}}$ , $k_{\text{ext}1342\text{nm}}$	1.14, 0.15	2.27, 0.15	2.95, 0.04	1.74, 6.48	-
$n_{2500\text{nm}}$ , $k_{\text{ext}2500\text{nm}}$	0.59, 1.74	2.3, ~0	2.73, ~0.02	1.37, 13.5	-

## 4 DEVELOPMENT OF PARALLEL RESISTANCE MEASUREMENT TECHNIQUE

**The material, related to this chapter was published in [A1] and [C5-7]**

Laser scribing of thin-films is based on the absorption of electromagnetic radiation in the material. The material is locally removed from the solid by evaporating, sublimating or in the state of a plasma. However, some of the laser affected material is not removed but remains in the solid as the heated or re-solidified material [66]. Both CIGS and CZTSe absorbers are complex, multi-component semiconductors, which start to decompose at temperatures far below the melting point. Both semiconductors start to lose Se and Sn content at 550 °C [67, 68]. High temperatures can lead to the absorber structural changes and formation of electro-conductive phases [69, 70]. These, in turn, result in the generation of shunts reducing the performance of PV devices.

Evaluation of the scribing quality is mainly done through visual (optical, SEM microscopes), elemental (EDS) [117, 118], and structural (micro-Raman spectrometry) [89] analysis. Shunt localization and evaluation of its properties can be performed with the dark lock-in thermography (DLIT) [7, 119], scanning spreading resistance microscopy (SSRM) [60], electroluminescence (EL) [7, 119, 120], photoluminescence (PL) [119, 121]. However, these methods are complex, slow, often require the specific preparation of the samples or does not always give reliable results.

The most reliable way is to apply direct electrical characterisation of a fully functional device. Efficiency measurements of fully laser scribed mini-modules were performed by several groups [6, 60]. However, this approach is very time-consuming and requires integration of the laser scribing tools into the CIGS production line or being located close to the production facility. Furthermore, careful optimisation of laser process requires a large number of mini-modules, all of which must undergo a complete production and post-processing stages. All of this introduce additional reliability issues due to bad contacting, sample handling, ageing, and batch to batch stability (e.g., film thickness, elemental composition, optical characteristics) [98]. It becomes difficult to distinguish efficiency changes caused by the laser scribing from the instability of the manufacturing process.

Precise optimisation and control over the laser parameters, such as laser wavelength, pulse duration, laser scanning speed, and pulse energy are essential to reduce damage to the remaining solar cell layers. Such a task requires comprehensive and time-consuming experiments, especially when

statistical analysis is necessary. Therefore, the ability to quickly and reliably apply direct electrical measurements to evaluate the laser-induced damage in the thin-film solar cells becomes of the first importance.

For such a task, a novel direct electrical measurement technique was developed and investigated in this chapter.

#### 4.1 Evaluation of the Nested circular laser scribing technique

In this section, the reliability of the NCLST technique is evaluated. For this task, the Atlantic laser 15 W (13 ps, 500 kHz, 532 nm) was used with a galvanometer scanner (optical laser system #2, see Fig. 30). Laser processing was performed in CIGS solar cell sample #5. The experimental procedure of the NCLST technique was discussed in section 3.7.

Two types of P3 isolation scribes were investigated: P3 Type 1 and Type 2. The former approach involved the direct ablation of the Al:ZnO/i-ZnO/CdS/CIGS layers to expose the Mo back-contact. The Type 2 scribe was based on the laser-induced lift-off process of the TCO layer. Laser processing parameters are presented in Table 7. The minimum diffraction-limited spot size of the focused laser beam was 10  $\mu\text{m}$ . Laser beam spot size was controlled by shifting the sample out of the focal plane.

**Table 7.** Laser P3 processing parameters.

Type of P3 scribe	Type 1	Type 2
Pulse energy, $\mu\text{J}$	21	15
Repetition rate, kHz	100	60
Scanning speed, mm/s	800	800
Beam size, $\mu\text{m}$	17	70

SEM image of the Type 1 channel is presented in Fig. 39a. Channel was ablated with 21  $\mu\text{J}$  laser pulses at 100 kHz pulse repetition rate. EDS and SEM analysis (Fig. 39) confirmed the exposure of the molybdenum layer. A sharp drop in the molybdenum content was observed at the centre of the scribe line. SEM images revealed that these were the small CIGS islets detected by the EDS.

In the case of Type 2 scribe, only the TCO layer had to be removed. Therefore, the channel was processed using lower pulse energy (15  $\mu\text{J}$ ) and lower pulse repetition rate (60 kHz). The laser spot size was increased to 70  $\mu\text{m}$ , which resulted in a laser fluence drop from 18.5 to 1  $\text{J}/\text{cm}^2$ . A front-contact layer was selectively removed with insignificant damage to the CIGS absorber surface (see Fig. 40a). Drop in zinc concentration confirmed the removal of the TCO layer (see Fig. 40b).

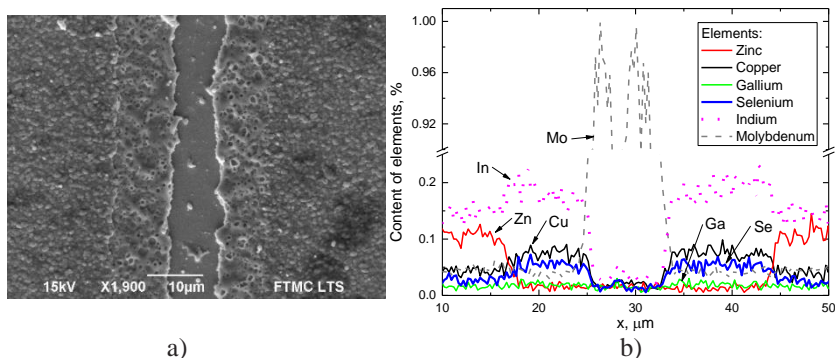


**Fig. 39.** SEM image (a) and EDS measurement (b) of P3 Type 1 laser scribe in a CIGS solar cell.

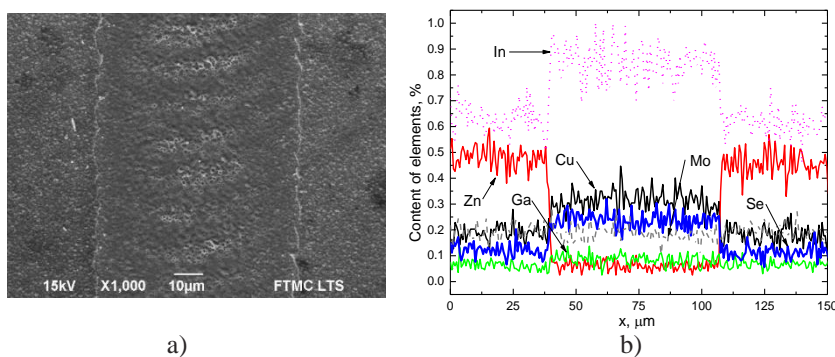


**Fig. 40.** SEM image (a) and EDS measurement (b) of P3 Type 2 laser scribe in CIGS solar cell.

Further, the conductivity of Type 1 and Type 2 scribes was investigated. A single NCLST experiment was comprised of 19 concentric rings. The radius of the circles was varied from 10 mm to 8.1 mm. One measurement probe was connected to the Al:ZnO top-contact and positioned in the centre of the circular scribes. The size of the electrode limited the smallest circle radius to 8 mm. The second probe was connected to the molybdenum back-contact. Parallel conductance measurements were applied after each circular scribe.

Fig. 41 shows the results for NCLST parallel conductance measurements for P3 Type 1 and Type 2 scribes. According to the measurements, one defect was localised within the scribing area for the P3 Type 1 case, and no defects were found for the P3 Type 2 case (a defect was distinguished by the sudden change in the parallel conductance). Therefore, the fitting function was adapted for the single and no defect cases. Experimental results were fitted with the NCLST fitting function (continuous black line). The extracted areal, laser scribe, and defect conductivity curves are presented in Fig. 41a and b along with the fit curve and the experimentally obtained data. The extracted coefficients are presented in Table 8. In the case of Fig. 41a (P3 Type 1

scribe), the centre of the defect was observed at the  $r$ -value of 9.1 mm. The width of the defect ( $w_d^{ID}$ ) was 0.09 mm. The areal and the laser scribe conductivities were 46 S/m<sup>2</sup> and 6.2 S/m, accordingly.

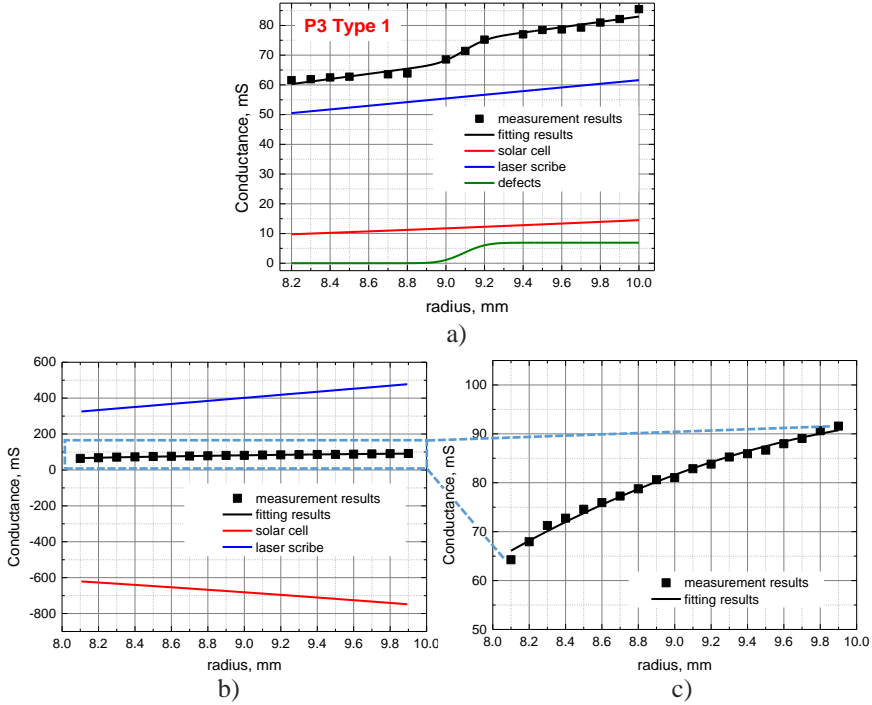


**Fig. 41.** Results of the parallel conductance of CIGS solar cell measurements for Type 1 (a) and Type 2 (b, c) P3 scribes. Graphs (a) and (b) presents the wider conductance range to accommodate experimentally measured results along with the simulated contributions of solar cell areal conductivity, laser scribing induced conductivity, and defect strength. Graph (c) shows an enlarged conductance region showing experimentally measured results for the P3 Type 2 case only.

**Table 8.** P3 laser scribe, areal and defect conductivity values extracted using NCLST technique.

Parameter	Laser scribe P3		Comments
	Type 1	Type 2	
$\sigma_{SCA}$ , S/m <sup>2</sup>	46	-282	
$\sigma_{SCM}$ , S/m	6.2	85	
$w_d^{ID}$ , mm	0.09	-	localised defect

Results for P3 Type 2 measurement are provided in Fig. 41b, c, and Table 8. Fig. 41c shows an enlarged conductance region, where it is visible that the measured parallel conductance of the investigated solar cell was saturating for higher  $r$ -values. In this case, a model provided a negative value of areal conductivity (-282 S/m<sup>2</sup>), which is an unrealistic result. To compensate for the

negative areal conductivity, the model exaggerated the laser scribe conductivity. Extracted laser scribe conductivity was significantly higher than the actual measured (net) parallel conductance (see Fig. 41b). Experiments with the same processing parameters were repeated multiple times with different samples; however, extracted values were widely spread and not reproducible (see Table 9). The average extracted values for areal and scribe conductivities were  $-20.3 \pm 164 \text{ S/m}^2$  and  $18.2 \pm 29.6 \text{ S/m}$ , respectively.

**Table 9.** P3 Type 2 laser scribe and areal conductivity values extracted using NCLST technique.

Parameter	Measurement No.						
	1	2	3	4	5	6	7
$\sigma_{SCA}, \text{ S/m}^2$	21	-22	130	121	98	-208	-282
$\sigma_{SCM}, \text{ S/m}$	8.8	9.9	1.5	4.8	6.7	11	85

The nested circular laser scribing technique was extensively used in [98, 100] and showed high reliability. In our case, the technique failed, by providing the negative areal conductivity in most cases. This behaviour indicated that the measurements did not follow the quadratic term  $\pi\sigma_{SCA}r^2$ .

#### 4.2 Simulation of the solar cell parallel conductance measurement

The reason for faulty NCLST results could be addressed to the high areal conductivity of the used CIGS sample. If the areal conductivity of the solar cell becomes comparable to that of the front-contact layer, the resistance of the latter layer might start to influence the measurements of the parallel conductance of the solar cell (especially for higher  $r$  values), which was not accounted in the NCLST model. In order to confirm that measurement errors depend on the areal conductivity of the investigated cells, a simulation replicating the NCLST measurement was conducted.

The numerical simulation took into account the electrical and geometrical parameters of the experiment: contact area between the I-V measurement probe and the solar cell's top-contact, circular geometry, thickness and conductivities of CIGS cell layers. NCLST measurements were modelled in COMSOL Multiphysics software by solving the Ohm's law:

$$\vec{J} = \sigma \vec{E} \quad (26)$$

here, the current density  $\vec{J}$  is directly proportional to the electric field  $\vec{E} = -\nabla V$  and the material's conductivity  $\sigma$ . A 2D, axisymmetrical geometry was used to replicate the circular laser scribing procedure used in the NCLST technique. Simulated geometry is shown in Fig. 42. Electrical parameters and thicknesses of constituent CIGS cell layers are presented in Table 10. The initial values for the Terminal 1 were set to  $V = 0 \text{ V}$  and  $I = 1 \text{ A}$ . The ground terminal

(Terminal 2) was set to  $V = 0$  V. The electric-insulation boundary condition was set to  $\vec{n} \cdot \vec{J} = 0$ .

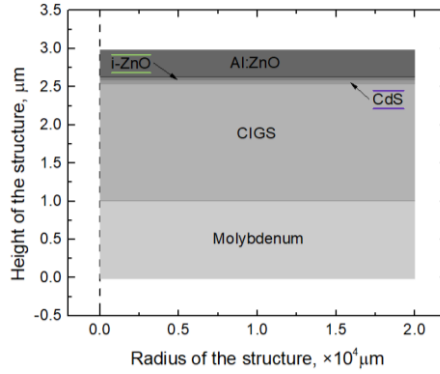


**Fig. 42.** A 2D axisymmetric model was conducted to simulate the NCLST experiment.

**Table 10.** CIGS cell parameters used in the model. Al:ZnO and Mo film conductivities were measured using the 4-point probe technique.

Material	Thickness, nm	S/m	Source
Al:ZnO	350	$5.19 \times 10^4$	4-point IV measurement of sample #5
i-ZnO	50	$3.33 \times 10^4$	[122]
CdS	50	$1 \times 10^{-5}$	[123]
CIGS	1500	1.67	[124]
Mo	1000	$1.67 \times 10^7$	4-point IV measurement of sample #5

In the simulations, Terminal 2 was set to cover all the surface area of the Mo back-contact. For Terminal 1, two cases were simulated: (1) terminal covering all the surface area of the Al:ZnO layer (this way the finite resistance of the top-contact can be neglected); and (2) terminal covering only a small  $0.8 \text{ mm}^2$  area located at the centre ( $r = 0$ ) of the simulated structure. In the latter case, a smaller contact area represented the top-contact probe used in the NCLST experiments in Section 4.1. The radius of the simulated structure was varied between 5 and 15 mm (covering the range of radii used in the actual NCLST experiments).

First, the electric potential distribution in the CIGS cell was simulated. The radius of the simulated structure was set to  $r = 8$  mm. Two electric potential distributions were observed, depending on the type of the terminal. In case of a full area Terminal 1 (Fig. 43), the electrical potential was uniform over all top-contact area. However, in the case of  $0.8 \text{ mm}^2$  contact area, the highest electric potential was observed at the centre of the structure where the probe was placed (Fig. 44). Electric potential gradually decreased when moving away to the edge of the structure. Such behaviour was related to the sheet resistance of the top-contact.

The following simulations show how the “measured” areal (parallel) conductivity of the solar cell depends on the type of the front-contact probe and the size (radius) of the isolated area.

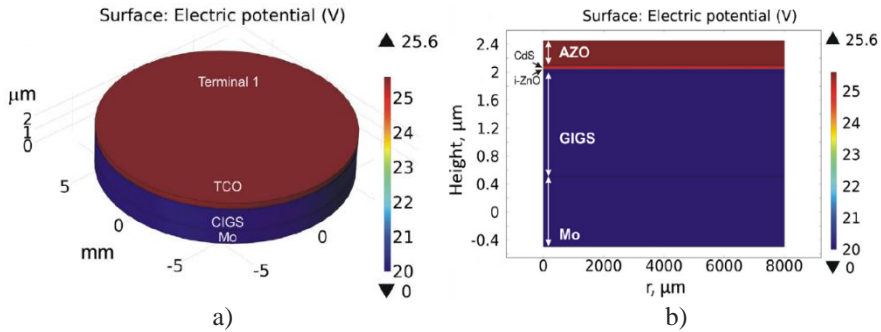


**Fig. 43.** Simulation of the electric potential distribution in CIGS solar cell. Terminal 1 and Terminal 2 covered the whole top and the bottom surfaces of the simulated cylinder.

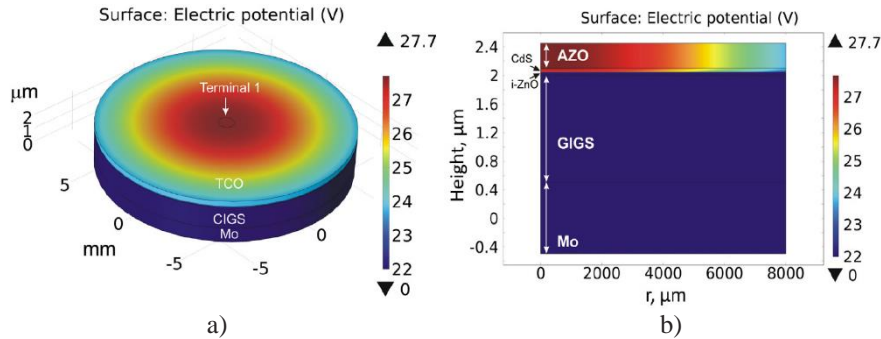


**Fig. 44.** Simulation of the electric potential distribution in CIGS solar cell. Terminal 1 covered an area of  $0.8 \text{ mm}^2$  at the top of the cylinder. Terminal 2 covered the whole bottom surface of the simulated cylinder.

The “measured” parallel conductance of the CIGS solar cell depended on the contact area of the top electrode and the radius of the simulated structure (Fig. 45). In the case of Fig. 45a, the areal conductivity of the CIGS layer stack was varied between 10 and  $194 \text{ S/m}^2$ , while the sheet resistance of the top-contact layer was fixed to  $55 \text{ } \Omega/\square$  (corresponding to  $5.19 \times 10^4 \text{ S/m}$ ). The dashed line represents the Terminal 1 covering the whole surface area of the simulated cell, while the solid lines represent the small probe regime ( $0.8 \text{ mm}^2$  area terminal). The simulation recorded a smaller parallel conductance of the CIGS cell when switched to the small probe regime. The deviation between the full surface and the small probe modes significantly depended on the conductivity of the CIGS layer stack.

Similar results were obtained in the case when the sheet resistance of the Al:ZnO layer was varied between 10 and  $90 \text{ } \Omega/\square$ , and the areal conductivity

of the CIGS layer stack was fixed to  $194 \text{ S/m}^2$ . Again, the simulation recorded a smaller resistance of the CIGS cell when switched to the small probe regime.

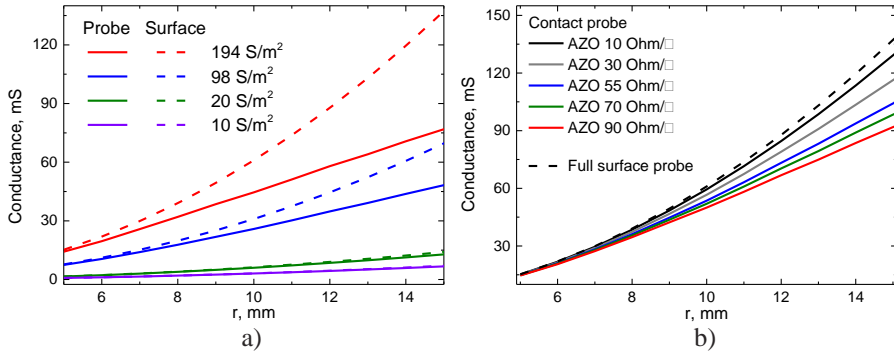


**Fig. 45.** Simulations of parallel conductance of CIGS solar cell versus the radius of the modelled structure: (a) Areal conductivity of CIGS layer stack was varied from 10 to  $194 \text{ S/m}^2$ , while sheet resistance of Al:ZnO layer was set to  $55 \text{ } \Omega/\square$ ; and (b) Al:ZnO top-contact sheet resistance varied from 10 to  $90 \text{ } \Omega/\square$  at constant CIGS layer stack areal conductivity of  $194 \text{ S/m}^2$ .

According to the simulations, measurement errors reached 22 % at the structure radius of 8 mm and increased to 37 % at a radius of 10 mm (for a CIGS cell with the Al:ZnO sheet resistance of  $55 \text{ } \Omega/\square$  and CIGS layer stack areal conductivity of  $194 \text{ S/m}^2$ ). It is likely that the errors were large enough to impact on the results obtained from the actual NCLST measurements. In the latter case, the errors could be kept under 5 % for the structure radius below 6 mm. However, the experimental setup limited the radius of the smallest isolated area to 8 mm. Therefore, another technique had to be developed to avoid geometry related limitations.

### 4.3 Linear laser scribing technique

Simulations showed that the errors in NCLST approach could be kept under 5 % if the experiment area was limited to the radius of 6 mm (for a CIGS cell with an areal conductivity of  $194 \text{ S/m}^2$  and a front-contact sheet resistance of  $55 \text{ } \Omega/\square$ ). However, due to the size limitation of the top-contact probe holder and the wiring of the front-contact, the minimum reachable radius was 8 mm.

In order to reduce the area of the single experiment, a new Linear Laser Scribing Technique (LLST) was developed. The concentric circular scribes were replaced with the scribing of shorter straight lines (see Fig. 35). This way, the size limitation of the front-contact probe holder was avoided by placing the front-contact probe near the laser scribes, but not in the centre of concentric rings. Shorter scribes could be performed in such a way that the distance between the measurement probe contacts and the laser scribes is no

more than 6 mm, minimising the laser scribing area from 50 – 80 mm<sup>2</sup> to less than 3 mm<sup>2</sup>. A complex fitting function was also simplified to a linear function having only one fitting parameter (laser scribe conductivity). More information on the LLST technique was presented in Section 3.8.

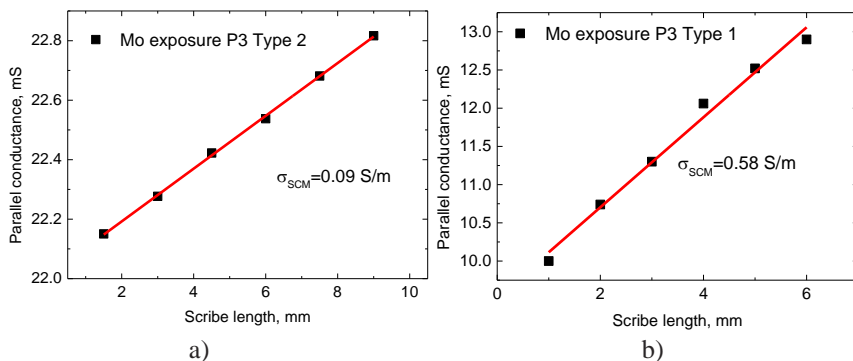


**Fig. 46.** Linear laser scribing technique (LLST) measurements in CIGS (a) and CZTSe (b) solar cells. Cases for P3 Type 2 (a) and P3 Type 1 (b) presented.

The result of the LLST cell parallel conductance measurement versus the laser scribed length is shown in Fig. 46a. Scribing was performed on the same solar cell as the NCLST experiments described in Section 4.1. The length of individual P3 Type 2 scribes was limited to 1.5 mm each located no more than 6 mm away from the measurement probe contacts. This way, the saturation of the parallel conductance of the CIGS solar cell was avoided. The relationship between the parallel conductance of the solar cell and the total scribed length exhibited a linear behaviour. The extracted P3 Type 2 scribe conductivity was 0.09 S/m. Measurements were repeated multiple times with the average extracted laser scribe conductivity of  $0.073 \pm 0.007$  S/m. The repeatability of the LLST experiment under the same processing conditions is shown in Table 11.

**Table 11.** The repeatability of the LLST experiment.

Parameter	Measurement No.					
	1	2	3	4	5	6
$\sigma_{SCM}$ , S/m	0.09	0.077	0.065	0.08	0.084	0.046

LLST P3 Type 1 tests were conducted in the CZTSe sample #2. Again, the linear behaviour between the scribe length and the parallel conductance of the solar cell was observed. The case for 0.58 S/m<sup>2</sup> is presented in Fig. 46b. Scribing and measurement procedures were repeated ten times confirming the repeatability and small measurement errors of the LLST approach: the average extracted laser scribe conductivity was  $0.47 \pm 0.05$  S/m.

It is worth to mention that several measurements can be made in the same sample area located close to each other without removing the measurement probes. Therefore, inaccuracy related to bad contacting and absorber layer inhomogeneity throughout the large solar cell area can be eliminated.

The LLST measurement procedure discussed above was used for all further laser scribe conductivity measurements presented in this thesis.

#### 4.4 Conclusions

1. The NCLST technique provided faulty CIGS areal conductivity results, which were addressed to the high parallel conductance of the CIGS sample used in our research and confirmed by numerical simulations.
2. The deviation between the areal CIGS conductivity simulated in a small probe and full area probe regimes depended on the areal conductivity of the CIGS sample and the area of the simulated structure. The difference can be kept below 5 % if the radius of the CIGS structure with  $194 \text{ S/m}^2$  areal conductivity is no larger than 6 mm.
3. Saturation of the measured parallel conductance of the CIGS solar cell was avoided by employing short and tightly packed laser scribes in the LLST technique.

## 5 P3 ISOLATION SCRIBES: OPTIMISATION OF THE LASER WAVELENGTH

**The material, related to this chapter was published in [C6], [C7], [C14], [C15]**

In this chapter, the influence of the laser wavelength to the conductivity of the P3 laser processing was investigated. Two types of P3 isolation scribes were performed: P3 Type 1 and Type 2 (more details on different P3 approaches are presented in Section 2.7.5). Experiments were conducted in a complete CIGS solar cell structure #5 presented in Fig. 47.

A vast number of investigations concluded that the use of ultrashort pulses was superior over the longer ns pulses in the visible and near infrared regions: laser-induced thermal damage was smaller and devices showed better electrical performance when ps pulses were applied [60, 81, 84, 125]. However, to the best of our knowledge, no data was published regarding the P3 processing of thin-film solar cells with mid-infrared wavelength lasers.

Therefore, we investigated the conductivity of P3 scribes processed with picosecond pulses in the 355 – 1342 nm wavelength range and compared to the nanosecond laser processing with a 2.5  $\mu\text{m}$  radiation wavelength. For such a task, we used two picosecond and one nanosecond lasers (Atlantic 15W, Atlantic 1342, and NT277).

LLST electrical measurements were performed to extract the conductivity of the P3 scribes. Finally, the laser absorption simulation was conducted to find the temperature distribution in the CIGS cell.

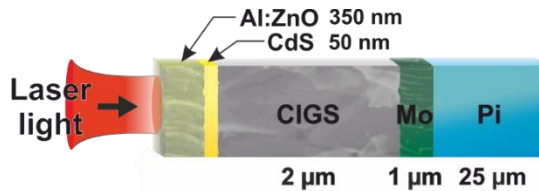


**Fig. 47.** Cross-section image of the CIGS #5 sample.

Type 1 and Type 2 P3 trenches were scribed with the 355 nm, 532 nm, 1064 nm, 1342 nm, and 2.5  $\mu\text{m}$  laser wavelengths. Laser scribing speed was set to 200 mm/s at the 100 kHz laser repetition rate for 355 - 1342 nm wavelengths. The smallest laser fluence was used with respect to high process quality and stability. Further reduction in pulse energy resulted in incomplete removal of the solar cell layers. In the case of a nanosecond laser, a fluence of 3 J/cm<sup>2</sup> was used for both Type 1 and Type 2 scribes. The laser operated only

at 1 kHz repetition rate; therefore, the sample scanning speed was limited to 5, and 30 mm/s for Type 1 and Type 2 scribing experiments, respectively.

### 5.1 SEM morphology analysis of P3 Type 1 and P3 Type 2 channels

SEM images of the laser processed Type 1 channels are presented in Fig. 48. Laser scribing speed and pulse repetition rate were adjusted to keep the pulse overlap at about 90 %. More details on Type 1 laser processing parameters are presented in Table 12.

**Table 12.** Laser processing parameters used in Type 1 CIGS scribing.

Wavelength, nm	Pulse duration, ps	Rep. rate, kHz	Laser fluence, J/cm <sup>2</sup>	Speed, mm/s	Peak intensity, W/cm <sup>2</sup>	Overlap, %
355	13	100	5	200	$1.69 \cdot 10^{12}$	89
532	13	100	4.2	200	$1.4 \cdot 10^{12}$	89
1064	13	100	2	200	$7.76 \cdot 10^{11}$	90
1342	13	100	3.8	200	$1.48 \cdot 10^{12}$	90
2500	6000	1	3	5	$3.6 \cdot 10^9$	90

A Type 1 channel ablated with the 2.5  $\mu\text{m}$  wavelength laser and a laser fluence of 3 J/cm<sup>2</sup> is shown in Fig. 48a. The surface of the Mo back-contact was cleanly exposed. However, significant melting at the edges of the channel was caused by long pulses locally forming CIGS aggregates.

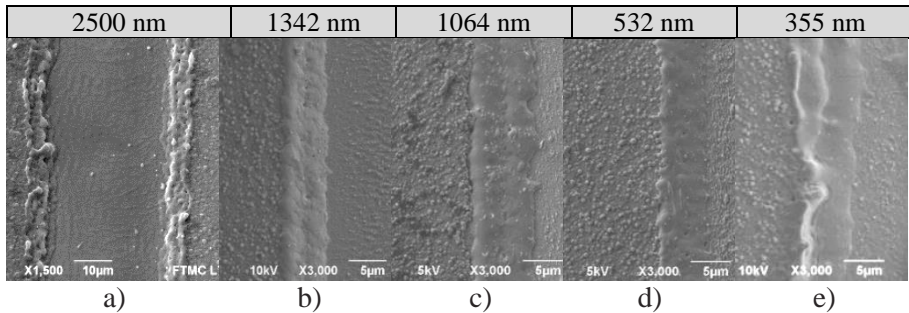


**Fig. 48.** SEM images of P3 Type 1 channel edges in CIGS #5 sample. Channels were ablated with (a) 2.5  $\mu\text{m}$ , (b) 1342 nm, (c) 1064 nm, (d) 532 nm, and (e) 355 nm laser wavelength radiations. 6 ns (a, full channel width view) and 13 ps (b – e, half-channel width views) duration pulses were used.

Transition to picosecond (13 ps) pulses improved the processing quality. Fig. 48b, c, and d show the channel edges processed with 1342, 1064 and 532 nm wavelengths, respectively. Exposure of the Mo layer required the laser fluencies between 2 and 4.2 J/cm<sup>2</sup> depending on the laser wavelength used (Table 12). The utilisation of shorter pulses reduced melting of the absorber layer. Exposed Mo surface was undamaged showing a high layer selectivity.

Optimisation of the P3 Type 1 scribe was not possible using 355 nm wavelength laser. Image of the trench ablated using the 5 J/cm<sup>2</sup> laser fluence is presented in Fig. 48e. The width of the exposed Mo channel was unstable, islets of partially ablated absorber periodically connected both sides of the channel. Furthermore, increasing the laser fluence above 5 J/cm<sup>2</sup> led to the back-contact damage rather than the removal of the CIGS layer. Interestingly, the melting of the CIGS layer with 355 nm laser was more pronounced compared to the channels processed with other wavelengths in the ps-pulse regime. Overall, high absorption of 355 nm laser led to a poor P3 channel quality and layer selectivity.

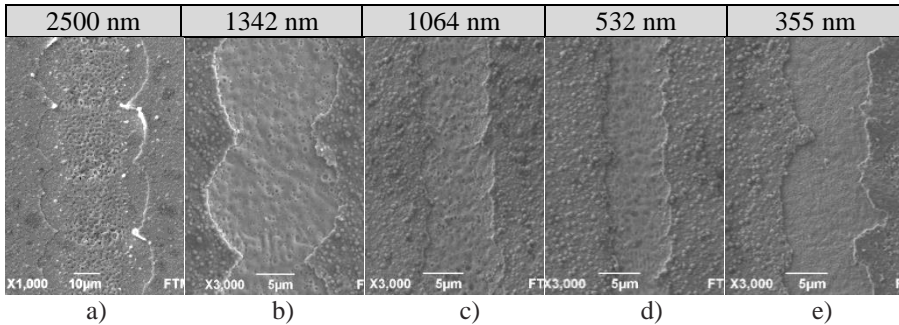


**Fig. 49.** SEM images of P3 Type 2 channel edges in CIGS #5 sample. Channels were ablated with (a) 2.5  $\mu\text{m}$ , (b) 1342 nm, (c) 1064 nm, (d) 532 nm, and (e) 355 nm laser wavelength radiations. 6 ns (a, full channel width view) and 13 ps (b – e, half-channel width views) duration pulses were used.

Type 2 scribing was based on the lift-off removal of the thin front-contact layer only. As a result, lower laser fluence and lower pulse overlap were applied, which minimised the thermal damage to the material.

**Table 13.** Laser processing parameters used in Type 2 CIGS scribing.

Wavelength, nm	Pulse duration, ps	Rep. rate, kHz	Laser fluence, J/cm <sup>2</sup>	Speed, mm/s	Peak intensity, W/cm <sup>2</sup>	Overlap, %
355	13	22	1	200	$3.32 \cdot 10^{11}$	20
532	13	30	0.5	200	$1.68 \cdot 10^{11}$	17
1064	13	30	0.3	200	$9.7 \cdot 10^{10}$	26
1342	13	14	0.75	200	$2.8 \cdot 10^{11}$	7
2500	6000	1	3	30	$3.6 \cdot 10^9$	37

P3 Type 2 processing parameters are presented in Table 13, while SEM images are shown in Fig. 49. As can be seen from the images, melting of the CIGS layer was minimised improving the visual quality of the scribes. Stable shape and cleanly exposed P3 channels were obtained for 1064 nm (0.3 J/cm<sup>2</sup>) and 532 nm (0.5 J/cm<sup>2</sup>) laser wavelengths – in a region where the front contact layer was the most transparent to laser radiation in the studied wavelength

range [23]. Scribing with the 355 nm wavelength radiation, produced the unstable shape of the channel with partly detached TCO flakes.

## 5.2 P3 scribe conductivity measurements

A non-optimized laser process can lead to a significant increase in parallel conductance of the solar cell. Resulting leakage currents could have a detrimental effect on the efficiency of the device. Therefore, direct electrical measurements (LLST) were conducted to validate the quality of the P3 scribes.

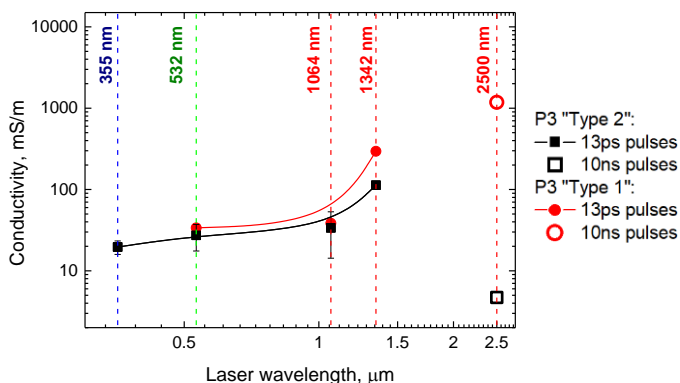


**Fig. 50.** Dependence of the P3 scribe conductivity on the used laser wavelength. Cases for P3 Type 1 and Type 2 scribing presented.

The dependence of the conductivity of P3 scribes on the laser wavelength is presented in Fig. 50. In the case of P3 Type 1 scribing (red dots), the smallest conductivity value of 33.8 mS/m was obtained for the 532 nm wavelength. A shift to 1064 nm laser radiation resulted only in a minor increase of the P3 scribe conductivity to 38.4 mS/m. Scribing with longer wavelength radiation further increased the conductivity of the scribes reaching a maximum value of 1.18 S/m at 2.5 μm. Scribes processed with the 2.5 μm nanosecond laser were 35 times more conductive compared to the least conductive 532 nm picosecond regime.

The extracted results on the P3 Type 2 scribing showed similar behaviour up to the 1342 nm radiation wavelength: the P3 conductivity increased when the longer wavelength was used to scribe the channels. The scribe conductivity reached the highest value of 0.11 S/m at the 1342 nm wavelength. The transition to the 2.5 μm wavelength gave an unexpected result. The least conductive P3 scribe was obtained using a nanosecond laser: the laser with the 2.5 μm wavelength and 6 ns duration pulses minimised the conductivity of P3 scribes to just 4.7 mS/m.

### 5.3 Simulation of laser-induced temperature distributions in CIGS cell

Numerical analysis was carried out in order to interpret the results of the LLST measurements. A 1D model was used to find the temporal evolution of the temperature distribution in the CIGS thin-film solar cell after a single laser pulse irradiation. Numerical model and the CIGS cell material parameters used in the simulations were discussed in more detail in Section 3.10.

Simulation result for a coupled laser energy distribution in the CIGS cell is presented in Fig. 51a. Here, a coupled laser energy in the CIGS cell was set equal for all wavelengths. Periodical modulation of the absorbed laser energy was caused by the reflection of the laser radiation at the inner surfaces of thin-films.

In the solar cell structure, the 355 nm radiation was efficiently absorbed in the CdS layer and did not penetrate the CIGS absorber. Longer wavelengths (532 and 1064 nm) were mostly absorbed either in CdS or Al:ZnO layers, however, a small part of it penetrated into the CIGS layer. On the other hand, the laser energy was absorbed in the upper part of the CIGS absorber leaving it mostly unaffected by the laser radiation.

The 1342 nm laser penetrated through the front-contact, buffer layer, and the absorber reaching the molybdenum back-contact. All of the coupled energy nearly equally distributed in the layers and, this way formed a continuous channel of the laser affected material from the TCO to Mo. In the case of the 2.5  $\mu\text{m}$  radiation, almost all coupled energy (93 %) was absorbed in the Al:ZnO layer. Energy remainder distributed in the CIGS and Mo layers.

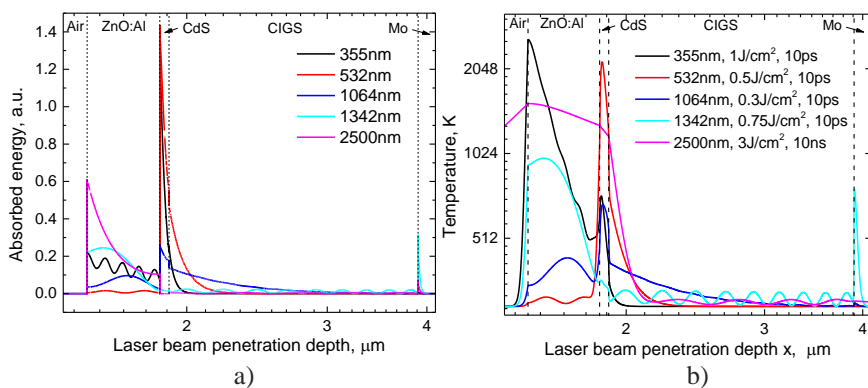


**Fig. 51.** Coupled laser energy distribution in the CIGS solar cell (a). Temperature distribution after a single laser pulse irradiation (b).

Further, the temperature distribution in the CIGS solar cell was simulated. The LLST measurements revealed that the P3 Type 2 approach resulted in less conductive P3 scribes compared to the Type 1 approach. For this reason, only the P3 Type 2 processing parameters (Table 13) were used as the input

parameters for the temperature distribution simulation. Taking into account that the P3 Type 2 scribing process is of low pulse overlap (less than 40 %), the case of single pulse irradiation was solved. Simulation results are presented in Fig. 51b. The temperature distribution in the CIGS cell is shown at the end of a laser pulse when the peak temperature is reached.

According to the simulations, the CIGS layer did not reach its melting temperature, which is reported to be between 1260 K and 1313 K [86]. The maximum peak temperature of 1100 K of the CIGS layer was recorded near the CdS/CIGS interface after the irradiation with the 2.5  $\mu\text{m}$  wavelength pulse. In other cases, the CIGS layer temperature was far from the melting point and ranged between 330 K and 700 K. Simulations suggested that in the case of P3 Type 2 processing, modifications in the CIGS absorber occurred at temperatures below the phase transition.

LLST measurements revealed that choosing the right laser wavelength for the process is crucial to minimise the conductivity of P3 scribes. A high absorption in the CIGS layer produced both P3 Type 1 and Type 2 scribes with conductivity lower than 40 mS/m, while the high absorption in the TCO layer (but not in the CIGS) produced the P3 Type 2 scribes with a low conductivity only.

Overall, the front-contact lift-off approach (P3 Type 2) was superior over the direct ablation (P3 Type 1). The lowest conductivity P3 Type 2 scribes were achieved using a nanosecond 2.5  $\mu\text{m}$  wavelength laser. Here, most of the laser pulse energy was absorbed in the Al:ZnO layer facilitating the removal of the TCO. Remaining laser energy did not induce any significant changes in the CIGS conductivity, which was associated with a low peak intensity of the nanosecond laser. However, ablation with picosecond pulses of 355, 532, and 1064 nm radiation wavelengths produced similar results.

Generally, Type 1 scribes are more conductive due to larger laser energy dose irradiated into the material. However, higher absorption in the CIGS layer can minimise the laser damage, which was observed with the 532 and 1064 nm laser. It should be noted that due to high absorption in the layers, ablation selectivity will suffer. In the case of the 355 nm laser, no optimised regime was found, since it was not possible to remove the CIGS layer entirely without damaging the molybdenum back-contact.

## 5.4 Conclusions

1. LLST measurements revealed the relationship between the P3 scribe conductivity and the used laser wavelength. It was possible to minimise the scribe conductivity by properly selecting the laser radiation

- wavelength, so that, according to the simulations, most of the laser energy was absorbed either in the CIGS absorber or in the TCO front-contact but did not penetrate down to Mo back-contact.
2. The P3 Type 2 scribing with the 2.5  $\mu\text{m}$  wavelength nanosecond pulses produced the lowest conductivity scribes of 4.7 mS/m.
  3. TCO lift-off (Type 2) approach was superior over the direct ablation (Type 1) of P3 channels in CIGS solar cells. At every investigated laser wavelength, the TCO lift-off produced scribes with lower conductivity. This was associated with the lower pulse overlap and laser fluence, which minimised the irradiated laser dose into the CIGS material.

## 6 P3 ISOLATION SCRIBES: THE CASE OF HIGH-SPEED SCRIBING

The material, related to this chapter was published in [A4], [C10], [C11], [C12], [C14]

Scaling up the manufacturing throughput is one of the major objectives for the successful development of CIGS thin-film technologies. Therefore, a laser should ensure high-speed scribing for a successful implementation of the laser tool in the industrial-scale production of thin-film photovoltaics.

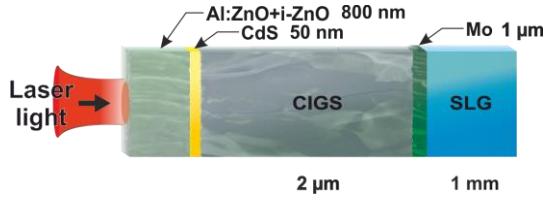


Fig. 52. Cross-section image of the CIGS sample #4.

During the laser processing, the laser fluence is kept relatively low to avoid thermal damage to the absorber layer. For this reason, laser systems working at 100 kHz pulse repetition range were not effectively utilised limiting the scribing speed to just several hundred mm/s.

Modern ultra-short lasers can offer high average power at the laser pulse repetition rates often exceeding 1 MHz. That provides a possibility to scale up the thin-film processing speeds while keeping the laser fluence low. Usually, this is realised by increasing the laser pulse repetition rate (together with the average power) and the laser scanning speed.

However, high repetition rates could lead to heat accumulation effects in the material [126]. Laser patterning of thin-film solar cells is not an exception, and during the high pulse repetition rate scribing, the heat accumulation effects also should be observed. In this case, heating of the CIGS absorber should cause degradation of the material resulting in the efficiency losses [70, 81, 85].

There is no comprehensive study covering the high-speed high-pulse repetition rate scribing of thin-film solar cells yet [71, 84, 127]. Therefore, in this section, the P3 processing of CIGS thin-film solar cells was investigated in the case of high-speed scribing. For this task, the Atlantic 60 W 13 ps pulse duration laser was used in the laser setup #2. Two wavelengths were used in the experiments: 532 and 1064 nm. During the experiments, the laser repetition rate was varied from 100 to 1000 kHz. The setup included the galvanometer scanner with an 80 mm focal length f-theta lens. The lens

focused the beam into an 11  $\mu\text{m}$  radius spot. Scribing was performed in CIGS sample #4. Scheme of the CIGS cell is provided in Fig. 52.

### 6.1 High-speed P3 scribing in CIGS solar cells. SEM morphology analysis

Two types of P3 scribes were investigated: P3 Type 1 and Type 2. Scribing was performed in a single scan to ensure sufficient process yield required to meet the demands of the industry (at least  $v = 2 \text{ m/s}$ ). Table 14 shows the summarised parameters for the investigated regimes. SEM images of the P3 scribes performed with 1064 and 532 nm wavelengths are presented in Fig. 53. The average width of the ablated channels was 30  $\mu\text{m}$ .

**Table 14.** Laser processing parameters used in CIGS scribing.

No.	P3 process	Rep. rate, kHz	Fluence, J/cm <sup>2</sup>		Speed, m/s	Pulse overlap, %
			1064nm	532nm		
1	Type 2	100	1.7	1.6	1.7	23
2	Type 1	200	3.8	2.9	0.4	91
3	Type 1	400	3.8	2.9	0.8	91
4	Type 1	1000	3.8	2.9	1.7	92

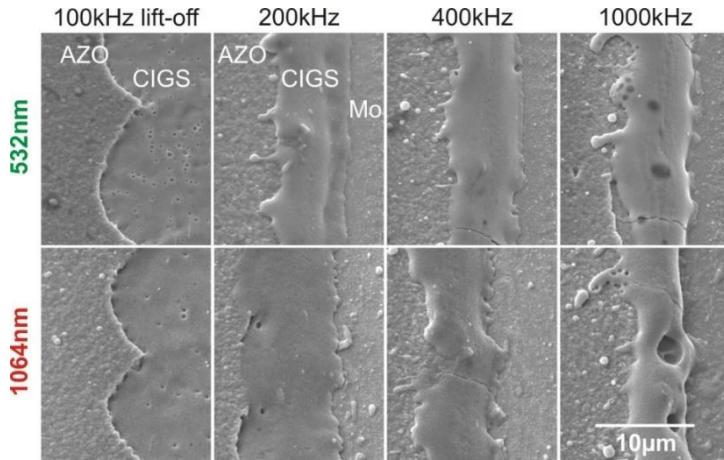


**Fig. 53.** SEM images of the P3 Type 1 and Type 2 scribe edges. P3 Type 1 processing was made with 200 – 1000 kHz laser repetition rate. P3 Type 2 channels were processed using the 100 kHz laser rep. rate. Channels were ablated with 1064 and 532 nm radiation wavelengths.

In the case of Type 1 scribes, laser beam scanning speed and pulse repetition rate were varied to maintain the constant pulse overlap between 91 - 92 %. Damage-free molybdenum layer was exposed in all cases. However, the melting of the CIGS absorber was significant at the edges of the scribe even for the 200 kHz regime. The increased pulse repetition rate (scribing speed) degraded the quality of the scribes: melting and cracking of the CIGS layer became more pronounced. Voids were formed at the 1 MHz

repetition rate. Taking into account that the laser irradiation dose was kept constant for different scribing speeds, the degradation of the absorber material was addressed to the heat accumulation effect. Switching to the 532 nm wavelength did not introduce any significant quality changes despite that the optimal laser fluence was reduced from 3.8 to 2.9 J/cm<sup>2</sup>.

The front-contact lift-off process was used for the P3 Type 2 processing. The laser fluence and the beam overlap were reduced to 1.6 - 1.7 J/cm<sup>2</sup> (depending on the used laser wavelength) and 23 %, respectively. A low pulse overlap enabled to reach 1.7 m/s scribing speed with a relatively low laser pulse repetition rate – 100 kHz. Subsequently, it improved the visual quality of the channels: the grooves were crack-free, had sharp edges, without any breaks. No heat accumulation effects were observed. A transition from 1064 nm to 532 nm laser did not introduce any significant changes to the visual quality of the scribes.

## 6.2 Scribe conductivity measurements

Further, LLST technique was used to extract the conductivity of P3 scribes. Series of laser scribes were performed in CIGS solar cell sample using the same laser processing parameters presented in Table 14.

The parallel conductivity of P3 Type 2 scribes is presented in Fig. 54. Ablation with the 532 nm radiation resulted in two times lower P3 scribe conductivity than the ablation with the 1064 nm wavelength: 0.0014 S/m and 0.0029 S/m, respectively. In this case, scribing with a 1064 nm wavelength radiation, induced more damage to the CIGS cell, although SEM images revealed no visual difference between those two scribes.

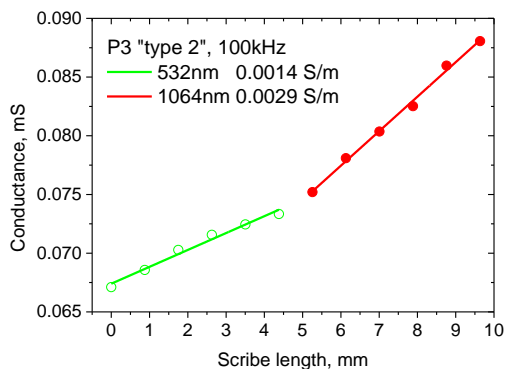


**Fig. 54.** Parallel conductance of CIGS solar cell versus the length of the P3 Type 2 scribe. Channels processing parameters: 100 kHz laser rep. rate, 1.7 m/s scribing speed. The measurements were performed for both 1064 nm (red dots) and 532 nm (green hollow dots) wavelength processing.

Switching to the direct ablation regime (P3 Type 1 scribing) significantly increased the P3 scribe conductivity (see Fig. 55). Scribing with a pulse repetition rate of 200 kHz resulted in significantly higher damage compared to the P3 Type 2 process. The scribe conductivity of 0.012 and 0.07 S/m was extracted for the 532 and 1064 nm cases, respectively. As the laser pulse repetition rate was increased, the conductivity of P3 scribes increased also. The maximum conductivity of 7.9 S/m was extracted for the 1064 nm laser working at 1 MHz pulse repetition rate. In this case, the maximum laser repetition rate was used to reach the scribing speed of 1.7 m/s. Again, processing with the green laser (532 nm wavelength) reduced the conductivity of P3 scribes.

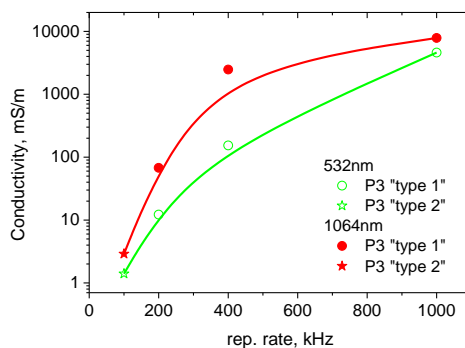


**Fig. 55.** Extracted P3 Type 1 and Type 2 scribe conductivity versus the laser repetition rate. The measurements were performed for both 1064 nm and 532 nm wavelength processing.

### 6.3 P3 processing of the mini-module

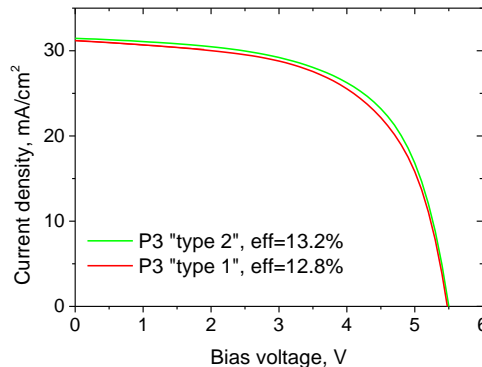
The P3 Type 1 and Type 2 scribing approaches were tested on two fully functional all-laser-scribed mini-modules. The active area of both mini-modules was  $32 \times 40 \text{ mm}^2$ . Each module consisted of eight  $4 \times 40 \text{ mm}^2$  sized cells interconnected in series. All laser scribes (P1, P2, and P3 steps) were realised with a picosecond 532 nm laser. The P1 and P2 processing parameters were the same for both mini-modules.

Laser processing parameters for the P3 step are presented in Table 15. P3 Type 1 scribing was realised using 96 % laser pulse overlap at  $0.65 \text{ J/cm}^2$  laser fluence. In the case of P3 Type 2 scribing, the laser pulse overlap was reduced to 30 %, and the laser fluence was reduced to  $0.49 \text{ J/cm}^2$ . Laser scribing was realised by moving the sample with translation stages, which resulted in low processing speeds. Consequently, the laser repetition rate was limited to 50 kHz.

**Table 15.** P3 processing parameters for mini-module scribing.

Module	P3 “Type 1”	P3 “Type 2”
CIGS #2	-	Pulse overlap 30%, fluence 0.49 J/cm <sup>2</sup>
CIGS #4	Pulse overlap 96%, fluence 0.65 J/cm <sup>2</sup>	-

J-V curves of the CIGS mini-modules were measured (see Fig. 56). The J-V parameters as depicted in Table 16 show gain in mini-module efficiency by 0.4 % (absolute) when switched from the P3 Type 1 to the Type 2 technique. Here, a more straightforward lift-off approach improved the open circuit voltage, short-circuit current, a fill factor, the module efficiency and the shunt resistance. The latter parameter, which is directly related to the laser-induced damage was improved most notably: the shunt resistance increased by 32 % from 297  $\Omega \cdot \text{cm}^2$  to 395  $\Omega \cdot \text{cm}^2$  per cell showing the increased quality of the P3 scribing. Obtained results were confirmed by the LLST measurements: the Type 2 scribing induced lower conductivity changes, which in result lead to a higher module efficiency.

**Fig. 56.** Mini-module electrical performance. Two different P3 scribing approaches were used – direct laser ablation (P3 Type 1) and top-contact lift-off (P3 Type 2).**Table 16.** Photo-electrical properties of the mini-modules.

Module number	P3 Process	$V_{oc}$ , V	$J_{sc}$ , mA/cm <sup>2</sup>	FF, %	$\eta_{eff}$ , %	$R_{ss}$ , $\Omega \cdot \text{cm}^2$ per cell	$R_{sh}$ , $\Omega \cdot \text{cm}^2$ per cell
1	P3 “Type 2”	5.50	31.3	61.2	13.2	2.84	395
2	P3 “Type 1”	5.48	31.2	59.9	12.8	2.82	297

Even at the low pulse repetition rate of 50 kHz, the difference between Type 1 and Type 2 techniques was evident. Increasing the P3 throughput to the industrially appropriate rates will force to use the high pulse repetition rate lasers. In the case of P3 Type 1 scribing, this could cause serious heat accumulation effects leading to even lower P3 scribe resistances.

On the other hand, the P3 Type 2 process showed very low scribe conductivity at the scribing speed of 1.7 m/s (100 kHz rep. rate). Therefore, it is the best candidate for the P3 structuring of thin-film solar cells.

#### 6.4 Mini-module efficiency simulation

PSPICE software was used to evaluate the PV mini-module efficiency degradation caused by the conductivity of the P3 scribes. The parameters for the 13.2 % efficiency solar cell were taken from the electrical measurements of the 8-cell mini-module “CIGS #2” described in Section 6.3 and are presented in more detail in Table 5 in Section 3.9. The active area of the simulated mini-module was  $3.2 \times 4 \text{ cm}^2$ , which was divided into eight equally sized strip-shaped cells ( $0.4 \times 4 \text{ cm}^2$ ) connected in series by seven 4 cm-long interconnects.

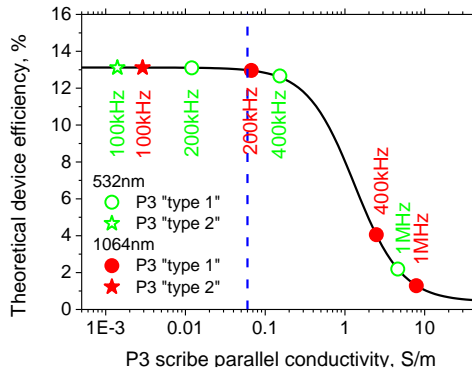


**Fig. 57.** Dependence of the simulated 8-cell CIGS mini-module efficiency on the P3 scribe conductivity.

Simulation results are presented in Fig. 57. The simulated curve represents the dependence of the CIGS mini-module efficiency on the conductivity of the P3 scribe. The extracted P3 scribe conductivity values are also plotted in the graph. A vertical blue dotted line separates device efficiency curve into two parts: a high-efficiency zone (to the left of the line), where the mini-module efficiency losses caused by the conductivity of P3 scribes are less than 1 %, relative; and the low-efficiency zone (to the right), where the losses are larger than 1 %, relative. According to the simulations, a high-efficiency device should possess a P3 isolation scribe with the maximum conductivity of less than 0.06 S/m in order to keep these losses below 1 %, relative.

The P3 Type 2 approach was superior over the P3 Type 1 approach in the mini-module efficiency. Both P3 Type 2 scribing regimes (scribing with 532 and 1064 nm wavelength radiations) were able to maintain efficiency losses below 1 %, relative, by removing the TCO layer only.

In the case of the P3 Type 1 processing, ablation with the 200 kHz pulse repetition rate was able to keep the losses below 1 %, relative. However, due to the low pulse rep. rate, the scribing speed was limited to just 400 mm/s. The P3 Type 1 processing with higher pulse repetition rates resulted in significant efficiency losses. Severe efficiency drop to 1.3 % (absolute efficiency) was recorded for the P3 Type 1 scribe processed with 1 MHz laser repetition rate. Therefore, only the P3 TCO lift-off technique maintained a high module efficiency at high scribing speeds exceeding 1 m/s.

### 6.5 High-speed scribing of P3 Type 2 channels

High-speed scribing of the P3 isolation scribes is crucial for the large-scale production of CIGS modules. According to the results, the best candidate is the P3 Type 2 approach, which ensures high processing speeds and low scribe conductivity. In this section, the P3 Type 2 scribing quality and scribe conductivity was evaluated in the case of a high-speed scenario. A polygon scanner, capable of moving the laser spot at 25 to 100 m/s utilised a full potential of the 1 MHz laser. For lower scribing speeds of 5, 10, and 15 m/s, the galvanometer scanner was pushed to its limit. In all cases, the laser pulse overlap was set to 50 % limiting the maximum scanning speed to 25 m/s. The laser beam was focused into a spot-size of 45  $\mu\text{m}$ . The first harmonics (1064 nm) of the picosecond laser was used in the experiments.

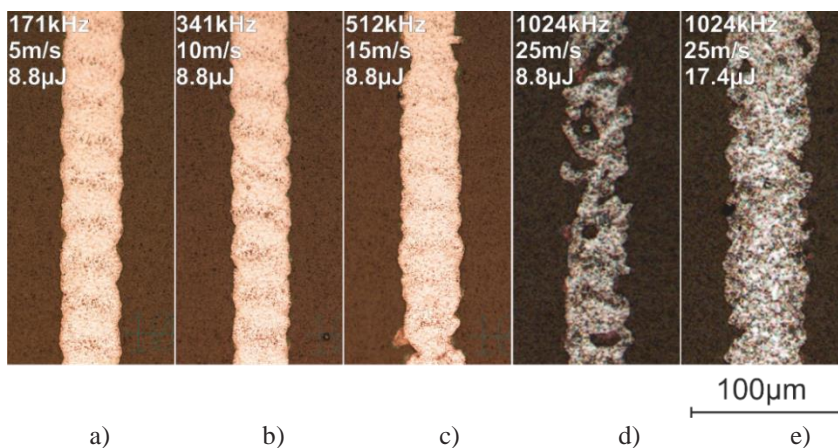


**Fig. 58.** Optical images of P3 Type 2 scribes ablated in CIGS thin-film solar cell with a galvanometer (a, b, c) and polygon (d, e) scanners. Constant pulse overlap of 50 % was maintained by controlling the laser scribing speed and laser pulse repetition rate.

After the series of experiments, an optimal pulse energy of 8.8  $\mu\text{J}$  was found to remove the TCO layer in the 5 – 15 m/s scribing speed range. Fig. 58a to c shows optical images of the P3 Type 2 scribes ablated using the

galvanometer scanner. Increasing the laser repetition rate, deteriorated the shape of the P3 channels. However, the channels remained continuous.

Transition to the polygon scanner allowed to employ the maximal laser repetition rate of 1024 kHz at the scribing speed of 25 m/s. However, the quality of the scribes was unsatisfactory: channels were not continuous, but with breaks, the width of the channels was unstable, and TCO islets remained in the laser ablated areas. For this reason, laser pulse energy had to be increased by twofold (to 17.4  $\mu\text{J}$ ) to produce a continuous channel (see Fig. 58d, e).

We believe that this was caused by the cloud of partially ablated TCO flakes ejected by the previous laser pulse. At the 1 MHz repetition rate, the time between pulses became too small for TCO flakes to leave the laser irradiation zone before the next laser pulse reaches the surface of the cell. The same experiment was repeated on the thin (60 nm) chrome layer (see Fig. 59). In the latter case, the channel quality did not deteriorate, since the chrome layer was evaporated.

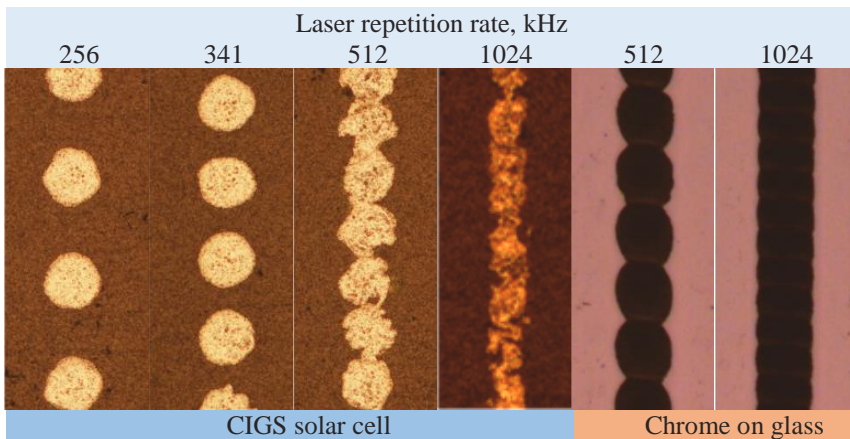


**Fig. 59.** Optical microscope images of P3 Type 2 scribes performed on the CIGS #4 sample and lift-off scribes on a thin chrome layer deposited on glass. The laser beam was scanned with a polygon scanner at 25 m/s. The quality of P3 scribes deteriorated with increasing laser repetition rate, however, remained of high quality when the chrome layer was ablated.

Next, the LLST technique was applied to evaluate the conductivity of the high-speed P3 Type 2 scribes. Results are presented in Fig. 60. It was found that conductivity of the scribes linearly depended on the scribing speed. By increasing the laser scribing speed from 5 m/s (171 kHz, 8.8  $\mu\text{J}$ ) to 25 m/s (1024 kHz, 17.4  $\mu\text{J}$ ), the extracted P3 scribe conductivity increased from 0.0019 S/m to 0.0033 S/m, respectively.

The P3 patterning at 25 m/s (1024 kHz) induced very low scribe conductivity, which, according to the simulations presented in Fig. 57 is well

below the recommended maximum P3 conductivity value of 0.06 S/m. The main limiting factor for the fast P3 Type 2 scribing was the beam shadowing by the TCO flakes, which forced to use a larger pulse energy to form a continuous channel. The maximum scribing speed for the high-quality P3 Type 2 scribing was 15 m/s.

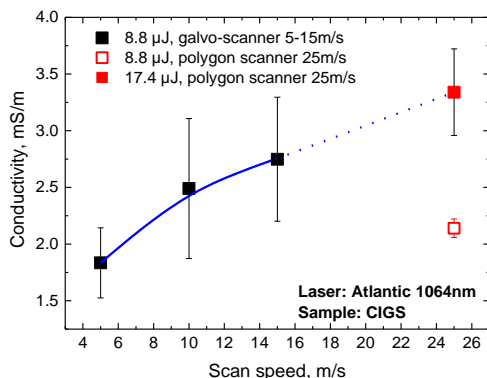


**Fig. 60.** Extracted P3 Type 2 scribe conductivity versus the laser scanning speed. Galvanometer scanner covered the laser scribing speeds from 5 m/s to 15 m/s (solid black symbols). Polygon scanner was used to form P3 Type 2 channels at the highest scribing speed of 25 m/s. Solid and hollow red symbols identify the P3 Type 2 channel formation with 17.4  $\mu\text{J}$  and 8.8  $\mu\text{J}$  pulses at 25 m/s, respectively. Processing at 25 m/s and 8.8  $\mu\text{J}$  resulted in an unsatisfactory quality of the channel.

## 6.6 Conclusions

1. Increasing the laser pulse repetition rate from 0.1 to 1 MHz increased the heat accumulation in the CIGS solar cell, which was observed as the pronounced melting, crack and void formation in the laser-scribed areas. This effect was highly dominant in the case of P3 Type 1 scribes.
2. P3 Type 1 processing at the 1 MHz pulse repetition rate resulted in the highest conductivity scribes of 7.9 and 4.6 S/m at the 1064 and 532 nm wavelengths, respectively. According to our simulations, the 8-cell mini-module should suffer from severe efficiency losses.
3. The TCO lift-off (Type 2) approach was the most promising scribing process: scribing at the 25 m/s speed and 1 MHz pulse repetition rate resulted in the extremely low P3 scribe conductivity of 3.3 mS/m keeping the efficiency losses below 1 %, relative.
4. The all-laser-scribed 8-cell mini-module structured using the P3 Type 2 process showed higher efficiency of 13.2 % compared to the 12.8 % efficiency of the device structured using the Type 1 approach.

## 7 P3 LIFT-OFF SCRIBING OF CZTSe THIN-FILM SOLAR CELLS

**The material, related to this chapter was published in [A5], [C1], [C2], [C3], [C4], [C13], [C14]**

Commonly, the P3 scribing is based either on the so-called direct laser ablation (Type 1) or the laser-induced lift-off of TCO layers (Type 2). Both techniques leave a small amount of laser-affected material remaining in the solar cell, which still may cause electrical degradation of the PV device.

Instead of two previously discussed techniques, a third option is available – the entire laser-induced mechanical front-side layer spallation (complete lift-off). The complete lift-off technique exposes the Mo back-contact by either removing Al:ZnO/i-ZnO/CdS/absorber layer stack (P3 case) or just an absorber layer (P2 case) mostly in the solid phase. Spallation occurs when the laser-induced stress exceeds the tensile strength of that layer. Stress build-up is mostly driven by the expansion of high-pressure vapour pillow generated by the laser energy absorption at the CZTSe/Mo interface, and the fast expansion of the laser-irradiated material. Therefore, specific laser processing parameters must be used to avoid direct layer ablation at the surface of the structure and allow laser energy to penetrate the structure down to the Mo back-contact.

Such technological approach can be one of the key techniques for the desired increase of the patterning speed maintaining a low scribe conductivity. However, no comprehensive study of the complete layer lift-off process was made covering ps and sub-ps pulse durations, and no electrical measurements of the P3 complete lift-off scribes were applied.

Therefore, in this section, the role of the laser pulse duration in the case of P2 and P3 complete laser lift-off processing was investigated in thin-film solar cells based on the CZTSe semiconductor.

For this task, two picosecond lasers from Ekspla – Atlantic and Atlantic HE were used to provide 10 ps and 60 ps duration pulses at the 1064 nm wavelength, respectively. A Pharos laser was utilised for 300 fs and 1 ps duration pulses. The Atlantic laser was combined with a galvanometer scanner (laser system #1). The Atlantic HE and the Pharos lasers were combined with motorised XYZ translation stages (laser system #2). Laser beams were focused with 80 mm focusing objectives resulting in a minimal diffraction-limited spot size of 23  $\mu\text{m}$ . The laser spot size on the sample surface was controlled by shifting the sample out of the focal plane using Z-axis translation stages. The sample was always shifted above the focal plane perpendicularly

to the beam propagation direction, keeping the focal spot below the processed surface.

The P3 scribing experiments were performed in a complete CZTSe structure, consisting of Al:ZnO/i-ZnO/CdS/CZTSe/Mo layers on the SLG substrate (Fig. 61a, Sample #3). P2 scribing experiments were performed in a partial CZTSe structure, consisting of CZTSe/Mo layers deposited on SLG substrate (Sample #1, Fig. 61b). In both cases, the thickness of CZTSe layer was 1.3  $\mu\text{m}$ .

LLST measurements were performed in a complete CZTSe structure, with the absorber thickness of 0.8  $\mu\text{m}$  (Fig. 61c, Sample #2). More details on the composition of the samples are presented in Section 3.4.

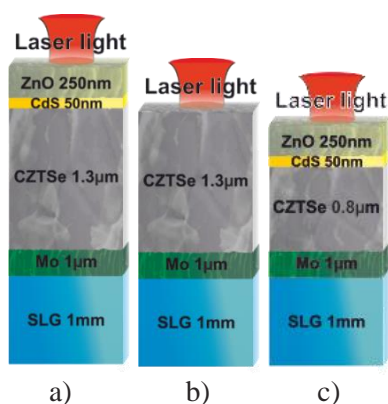


**Fig. 61.** The structures of the complete (a) and partial (b) CZTSe solar cells. A thinner cell (c) was used for the LLST conductivity measurements.

### 7.1 Lift-off crater size dependence on the laser pulse duration

Single pulse front-side crater ablation experiments were carried out in the partial and complete CZTSe solar cell structures with an absorber layer thickness of 1.3  $\mu\text{m}$ . When a tightly focused laser pulse was irradiated onto the surface of the CZTSe solar cell, a crater was formed by partly evaporating and partly melting the absorber layer (see Fig. 62). Increasing the laser spot size caused the laser-irradiated area to bulge. When a sufficient laser spot size was reached, a constant and highly-repeatable lift-off crater was formed exposing the molybdenum back-contact (see Fig. 63) [128].

The dependence between the minimal crater size and the laser pulse duration was investigated. The laser pulse energy was set to 50  $\mu\text{J}$ . The minimal P2 crater size in a partial CZTSe structure was linearly dependent on the pulse duration in the logarithmic scale (see Fig. 64).

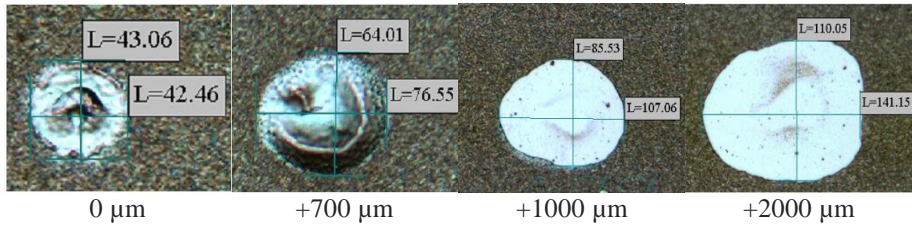


**Fig. 62.** Optical images of the lift-off crater formation in the partial CZTSe structure. The laser pulse energy was set to 50  $\mu\text{J}$ . Laser beam defocus was changed between 0 and 2 mm.

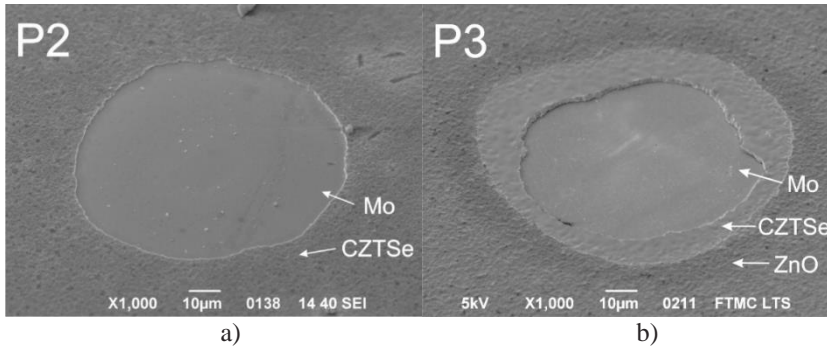


**Fig. 63.** SEM images of typical P2 and P3 lift-off craters ablated in the partial (a) and complete (b) CZTSe structures, respectively. The laser fluence of 3.1  $\text{J}/\text{cm}^2$  and 1 mm defocus were used for the 10 ps pulse irradiation in both structures.

P2 craters with the smallest diameter were produced with 300 fs pulses: the minimum diameter of the exposed molybdenum was 62  $\mu\text{m}$ . In this case, defocus was set to 0.6 mm, which corresponded to the laser fluence of 7.3  $\text{J}/\text{cm}^2$ . Transition to the 1 ps pulse duration increased the crater diameter to 75  $\mu\text{m}$  (0.8 mm defocus and 4.8  $\text{J}/\text{cm}^2$  fluence), while 10 ps pulses facilitated the formation of 83  $\mu\text{m}$  craters (1 mm defocus, 2.9  $\text{J}/\text{cm}^2$ ). The longest 60 ps pulses produced the largest craters. The minimum diameter of the exposed Mo layer was 120  $\mu\text{m}$  at the 1.8 mm defocus and 1  $\text{J}/\text{cm}^2$  fluence.

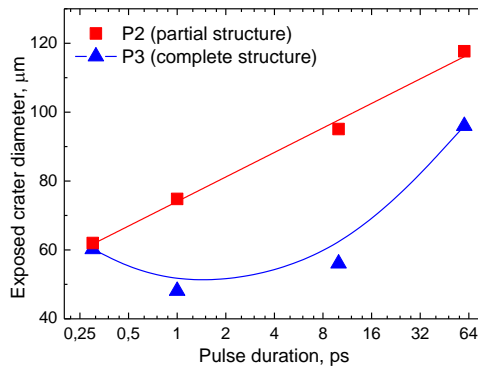


**Fig. 64.** The minimum diameter of the exposed molybdenum craters.

In the case of the complete CZTSe structure, the P3 crater size dependence on the pulse duration was less straightforward (see Fig. 64). Additional ZnO and CdS layers increased structural complexity. Therefore, the dependence of the exposed crater diameter on the pulse duration was no longer linear, but with the minimal – 1 ps pulses produced 48.1  $\mu\text{m}$  diameter craters. In this case, the focus offset was set to 0.7 mm (6.5 J/cm<sup>2</sup>). Again, the longest pulses produced the largest craters reaching 96  $\mu\text{m}$  in diameter (2.1 mm defocus and 0.75 J/cm<sup>2</sup>).

Shorter laser-material interaction (shorter duration pulses) caused lower thermal energy diffusion into the bulk of the material. Therefore, a sharper thermal transition between the cold and hot areas of the material induced higher stresses facilitating easier layer spallation. We believe that that was the reason why shorter pulses produced smaller diameter craters.

Griffith's criterion [77] states that if the tensile stress is too small to initiate the layer spallation, the lack of it can be compensated by a larger delamination area. In this case, longer pulses induced smaller stresses in the material and larger areas had to be irradiated to initiate the spallation.

## 7.2 Punching threshold of CZTSe lift-off craters

A punching threshold, which is the minimum laser fluence required to realise the lift-off, was investigated. Fig. 65 shows that the punching threshold in the partial and complete CZTSe structures was inversely proportional to the laser pulse duration. The highest threshold value was obtained for 0.3 – 1 ps pulses. The peak values were 0.5 and 0.9 J/cm<sup>2</sup> to expose the P2 and the P3 crater, respectively. The transition to the longer pulses reduced both the threshold difference between the P2 and P3 cases and the values itself. Finally, the lift-off process was most efficient for 60 ps pulses. Working with 60 ps pulses reduced the threshold value to a minimum value of 0.2 J/cm<sup>2</sup> for both P2 and P3 processes.

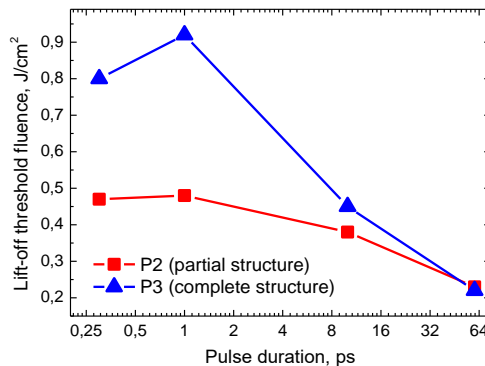


**Fig. 65.** Laser lift-off punching threshold fluence versus the laser pulse duration.

### 7.3 Morphological analysis of CZTSe lift-off craters

SEM was used to evaluate the visual quality of the craters. Fig. 66a shows front-side views of typical craters formed in the partial CZTSe structure without the TCO and buffer layers. The quality of the craters was very similar despite the different pulse duration. Processing did not induce any melt or burr formation at the perimeter of the crater. The use of the femtosecond pulses did not provide any noticeable advantage over the longer pulses in the picosecond time range.

Ablation of the P3 craters resulted in an exposed molybdenum crater surrounded by the ring-like structure (see Fig. 66b). Here, the front-contact was removed exposing the CZTSe layer. Longer 10 – 60 ps pulses caused more melting of the exposed CZTSe surface layer. On the contrary, sub-ps pulses preserved the exposed layer topography similar to that of unaffected areas.

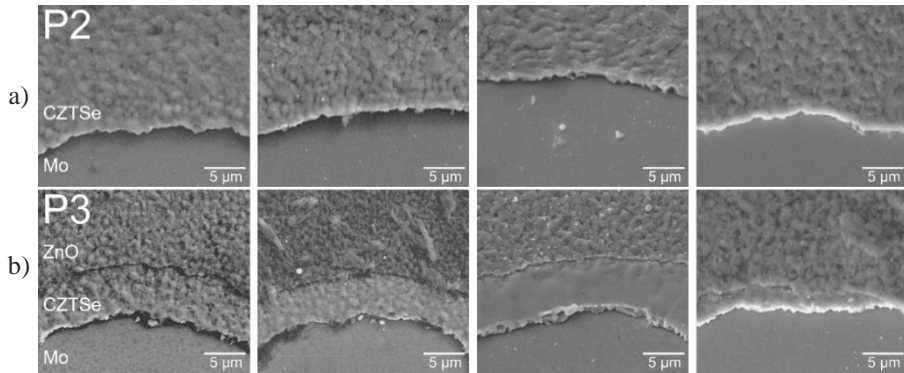


**Fig. 66.** SEM images of exposed P2 and P3 craters in partial (a) and complete (b) CZTSe structures, respectively. Laser fluence  $2.2 \text{ J/cm}^2$  and  $1.2 \text{ mm}$  defocus was used for 300 fs, 1 ps and 10 ps pulse durations. For 60 ps pulses, the laser fluence was reduced to  $0.83 \text{ J/cm}^2$  and defocus shifted to  $2 \text{ mm}$ .

Fig. 67 shows the cross-section views of the P2 and P3 crater edges. A white dotted line separates the exposed molybdenum area (to the right of the dotted line) and the surrounding area (to the left of the dotted line). The purple area shows the pre-deposited protective platinum (Pt) layer used in the sample preparation by focused ion beam (FIB). In the case of the P2 crater, no damage to the absorber or the Mo layer was observed near the crater's edge.

On the other hand, a thin layer of a melted absorber was observed in the complete CZTSe structure (around P3 crater, marked in yellow). The thickness of the affected layer was measured to span between  $0.25$  and  $0.3 \mu\text{m}$ , which was about one-fourth of the CZTSe layer. However, no direct contact

between the melted absorber and the molybdenum layer was observed, reducing the probability of short-circuiting the cell.

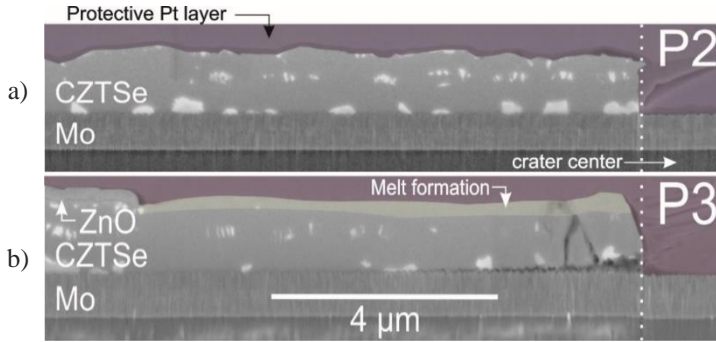


**Fig. 67.** SEM cross-section images of P2 and P3 craters ablated with 10 ps duration pulses in the partial (a) and complete (b) CZTSe structures, respectively. Ablation parameters:  $2.2 \text{ J/cm}^2$  and 1.2 mm defocus.

#### 7.4 Micro-Raman spectroscopy of CZTSe samples

Micro-Raman spectroscopy was used to investigate any structural changes and secondary phase formation induced by the laser process. The laser non-affected areas were analysed first. Afterwards, Raman measurements were conducted  $5 \mu\text{m}$  away from the laser ablated crater edge in the partial CZTSe structure (see Fig. 68a). In the case of the complete CZTSe structure, the measurements were taken in the centre of the exposed kesterite ring (see Fig. 68b). The distance from the inner edge of the exposed ring-structure was approximately  $5 \mu\text{m}$ .

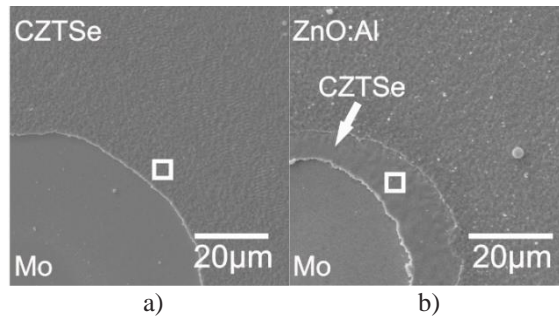


**Fig. 68.** A scheme of Raman measurements in the partial (a) and complete (b) CZTSe structures. Measurement spots are marked as white squares.

Spectra measured in the laser non-affected areas are indicated as “0” and are shown in Fig. 69. Both spectra exhibited typical CZTSe-pronounced peaks appearing at  $172 \text{ cm}^{-1}$  [129] and  $196 \text{ cm}^{-1}$  [130]. A low-intensity peak was observed at  $233 \text{ cm}^{-1}$  [130], which was also assigned to CZTSe. In the case of

the secondary phases, only a low-intensity ZnSe peak was observed at  $251 - 252 \text{ cm}^{-1}$  [131-133].

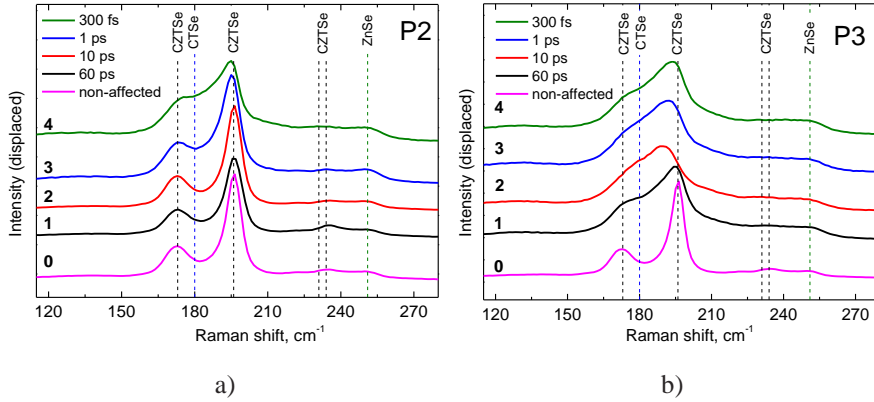


**Fig. 69.** Raman spectra of  $\text{Cu}_2\text{ZnSnSe}_4$  layer in the partial P2 (a) and complete P3 (b) solar cell structures  $5 \mu\text{m}$  away from the exposed molybdenum crater edge. The numbers from 1 to 4 correspond to the used laser pulse duration. Raman spectra of a laser non-affected areas are noted as 0.

Raman spectra measured in a partial CZTSe structure are presented in Fig. 69a. Spectra labelled 1 – 4 denote the laser pulse duration from 60 ps to 300 fs, respectively. An impact of the laser pulse duration was clear. The valley between two main CZTSe peaks at  $172$  and  $196 \text{ cm}^{-1}$  started to rise when the shorter pulses were used.

Furthermore, two peaks fused into one asymmetric peak after the processing with 300 fs. This effect shows increasing structural disorder in the crystal CZTSe lattice and the formation of CTSe ( $\text{Cu}_2\text{SnSe}_3$ ) phases at  $180 \text{ cm}^{-1}$  [129]. The latter compound is a low bandgap (0.8 eV) secondary phase, which can limit the open-circuit voltage of the solar cell [134]. The CZTSe peak broadening at  $234 \text{ cm}^{-1}$  was observed with the decrease in the pulse duration until it became indistinguishable when 300 fs duration pulses were applied (see Fig. 69a).

Fig. 69b shows Raman spectra measured at the centre of the exposed kesterite ring in the P3 structure. Significant changes in the CZTSe Raman signal was observed for all inspected laser pulse durations. Such behaviour was related to the increase of structural disorder and formation of the CTSe secondary phase. The characteristic CZTSe low-intensity peak at  $234 \text{ cm}^{-1}$  was not found in the laser affected area.

Laser-induced heating of the absorber layer could lead to the formation of the Cu-rich phase, which is observed in the CIGS cells. However, it should be valid for the CZTSe absorbers as well [79, 135]. The formation of the Cu-rich compound results in higher carrier concentration and shunting effects [136].

## 7.5 P3 scribe conductivity measurements and comparison with Type 1 and Type 2 scribes

The P3 lift-off trench scribing experiments were conducted in the complete CZTSe sample comprising of a slightly thinner  $0.8\ \mu\text{m}$  CZTSe absorber layer (Sample #2). Scribing was performed with 300 fs, 1 ps, and 10 ps pulses. Experimental conditions were kept as similar as possible: laser fluence was set to  $2.34\ \text{J}/\text{cm}^2$ , scanning speed to  $10\ \text{mm}/\text{s}$ , repetition rate to  $310\ \text{Hz}$ , and laser focus offset to  $400\ \mu\text{m}$  for investigated pulse durations. Ablated trenches were of high quality: edges were sharp, forming continuous and uninterrupted channels (see Fig. 70a).

Additionally, the Type 1 and Type 2 scribes were performed in the same CZTSe sample with 300 fs, 1 ps, and 10 ps duration pulses. The laser scanning speed was kept the same ( $10\ \text{mm}/\text{s}$ ), and the laser beam was focused on the sample surface. In the case of the Type 1 scribing (direct material ablation), the molybdenum back-contact was exposed with the  $1.35\ \text{J}/\text{cm}^2$  fluence and  $5\ \text{kHz}$  pulse repetition rate. For the Type 2 scribe (TCO lift-off), both the fluence and the pulse repetition rate were reduced to  $0.4\ \text{J}/\text{cm}^2$  and  $700\ \text{Hz}$ , respectively. SEM micrographs of the P3 Type 1 and Type 2 scribes are presented in Fig. 70b and c, respectively.

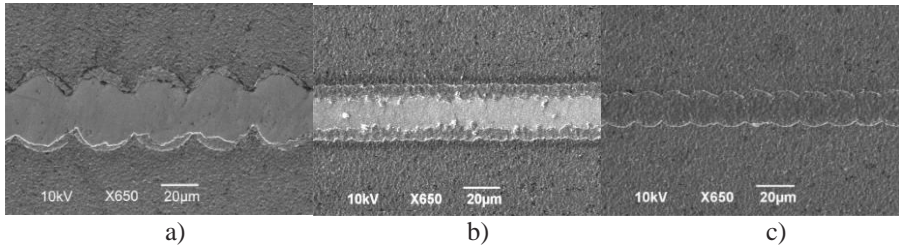


**Fig. 70.** SEM image of P3 scribes in a complete CZTSe sample ablated with 300 fs pulses. P3 complete lift-off (a), Type 1 (direct ablation) (b), and Type 2 (TCO lift-off) (c) cases presented.

The LLST technique was used to evaluate the conductivity of the P3 scribes. In the case of the complete lift-off, results showed that the P3 scribe conductivity had an inverse dependence on the laser pulse duration (see Fig. 71). Best results were achieved while scribing with the longest pulse duration ( $10\ \text{ps}$ ) –  $0.64\ \text{S}/\text{m}$ . Transition to shorter pulses increased the P3 scribe conductivity to  $0.78\ \text{S}/\text{m}$  and  $0.94\ \text{S}/\text{m}$  for  $1\ \text{ps}$  and  $300\ \text{fs}$  pulses, respectively. According to the results, shorter pulses induced higher conductivity scribes.

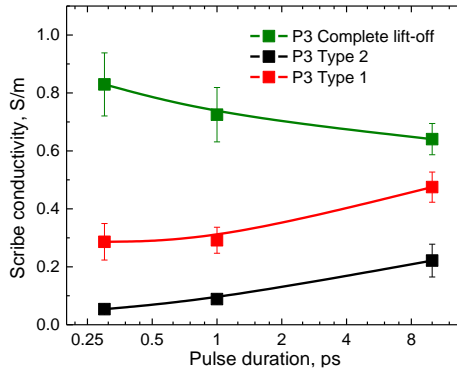


**Fig. 71.** Extracted P3 scribe conductivity versus laser pulse duration.

Although the complete lift-off approach showed the best visual quality of the scribes (minimum melting of CIGS absorber), the latter approach was inferior to both Type 1 and Type 2 approaches regarding the conductivity of the scribes. The lowest conductivity scribes were scribed using the shortest 300 fs pulses: Type 1 approach produced  $0.29 \pm 0.06$  S/m conductivity scribes, while Type 2 minimised the conductivity to  $0.05 \pm 0.01$  S/m. The LLST measurements showed that the conductivity of Type 1 and Type 2 scribes was directly dependent on the laser pulse duration.

One of the effects facilitating the complete lift-off is the laser energy absorption at the CZTSe/Mo interface. For this to happen, laser radiation should penetrate through the TCO, CdS, and CZTSe layers down to Mo. Experimental results demonstrated smaller P3 crater sizes compared to the P2 craters, meaning that part of the laser energy was absorbed in the exposed kesterite ring (in the area around the exposed Mo crater). Therefore, the shorter duration pulses could produce higher conductivity scribes due to higher pulse peak intensities heating CZTSe to higher temperatures around the exposed Mo crater.

On the contrary, both Type 1 and Type 2 approaches utilised lower laser fluence and were focused into smaller spot sizes minimising the laser affected area. The material was either directly ablated or removed due to the TCO layer spallation. In both cases, shorter laser pulses reduced thermal diffusion length, which resulted in lower P3 scribe conductivity.

## 7.6 Mini-module efficiency simulation

A 3-cell CZTSe mini-module simulation was conducted to evaluate the possible efficiency losses caused by the parallel conductance of the P3 scribes. The model used in the simulation was presented in Section 3.9.2. Simulations included Standard Test Conditions and neglected the influence of P1 and P2

scribes. Three CZTSe cells were serially connected via two monolithic interconnects (which included two P3 scribes). Fig. 37 shows the equivalent circuit of the mini-module. A 1 cm<sup>2</sup> area square-shaped cells were simulated. Parameters for the 9.7 % efficiency DC-sputtered CZTSe solar cell were borrowed from [104]. The model did not include the active area loss caused by the dead area.

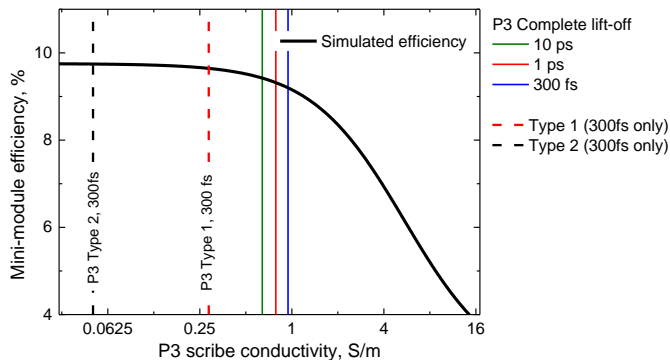


**Fig. 72.** Dependence of the simulated 3-cell CZTSe mini-module efficiency on the P3 scribe conductivity.

The extracted mini-module efficiency of 9.76 % correlated well with the experimentally measured value in [104]. Fig. 72 illustrates the dependence of a simulated 3-cell mini-module efficiency on the P3 scribe conductivity. Regarding the complete lift-off scribes, 10 ps duration pulses caused the smallest efficiency losses of 3.6 % relative (see Table 17). The transition from the 10 ps pulses to sub-ps pulses (300 fs) decreased the absolute module efficiency from 9.4 % to 9.2 %, which could be evidence of non-linear absorption effects with femtosecond laser pulses.

**Table 17.** Simulated 3-cell CZTSe mini module efficiency based on the experimentally measured conductivity of P3 scribes.

P3 scribe type	Pulse duration	Scribe conductivity, S/m	Module efficiency, % (absolute)	Efficiency loss, % (relative change)
Complete lift-off	300 fs	0.94	9.2	6.1
Complete lift-off	1 ps	0.78	9.32	4.7
Complete lift-off	10 ps	0.64	9.42	3.6
Type 1	300 fs	0.29	9.64	1
Type 2	300 fs	0.05	9.74	0.2

The complete lift-off approach fell behind the Type 1 and Type 2 counterparts regarding the absolute module efficiency. The Type 2 approach was far more superior with the absolute efficiency of 9.74 %.

## 7.7 Conclusions

1. The complete lift-off approach enhanced the quality of P2 and P3 laser processes: melting of the CIGS layer was avoided entirely, or negligible compared to other conventional laser patterning approaches.
2. Raman measurements revealed that the shorter duration pulses resulted in a more pronounced structural disorder of the main CZTSe phase and the formation of the conductive CTSe phase.
3. The lowest P3 complete lift-off scribe conductivity of 0.64 S/m was achieved with the longest pulse duration (10 ps) investigated in the LLST experiments.
4. Despite the reduced melting of the CZTSe layer, the complete lift-off scribes were significantly more conductive compared to the P3 Type 1 and Type 2 approaches by 2.3 and 12.8 times, respectively.

## 8 FORMATION OF P2 INTERCONNECTS BY MODIFYING THE CONDUCTIVITY OF CIGS ABSORBER WITH A PICOSECOND LASER

**The material, related to this chapter was published in [A2], [A3], [C8], [C9]**

A conventional thin-film solar module production incorporates three patterning steps identified as P1, P2, and P3. These scribes are not performed immediately one after another but at different stages of the module production. Therefore, the cell deposition processes must be interrupted for the laser scribing to be applied. It complicates the production of the modules, since at least three vacuum pumping steps are required, each followed by ventilation, laser alignment, and scribing procedures.

The non-optimized P3 patterning regimes resulted in a significant increase of the solar cell's parallel conductance. It was quickly noticed that laser could be used to deliberately transform the CIGS absorber into the highly conductive areas to act as P2 interconnects. This method was first shown in [78, 79]. Authors used a nanosecond laser to obtain the P2 laser-weld resistivity of about  $1 \Omega \times \text{cm}$  ( $1 \text{ S/m}$ ), which was comparable to that achieved in conventional mechanically patterned modules [137, 138]. This way, three scribing steps could be reduced to two by performing P2 and P3 scribes at the same time after the TCO deposition.

Unfortunately, the nanosecond pulses are not favourable due to high thermal effects [139]. In this case, the ultra-short pulsed laser should be introduced alongside the nanosecond laser.

This chapter discusses the possibility to use a picosecond laser for the P2 series interconnect formation. A single ultrashort laser could be used for both P2 and P3 processes, this way, reducing the costs and increasing the throughput of the production line [80].

### 8.1 Conductivity of micro-weld channels in CIGS solar cell

The P2 experiments were focused on finding the optimal picosecond laser fluence and pulse overlap parameters to modify laser-irradiated areas into a highly conductive compound. The Atlantic 60 W ultra-short pulse laser working at 1 MHz pulse repetition rate was used in the laser setup #2. Laser beam spot size was set to  $50 \mu\text{m}$  by slightly shifting the sample out of the focal plane. The LLST measurements followed the P2 processing. It was found that the conductivity of the P2 scribes highly depended on the laser irradiation dose. A balance between the laser fluence and pulse overlap was required to

maintain sufficient CIGS modification without completely removing the CIGS layer nor damaging the molybdenum back-contact.

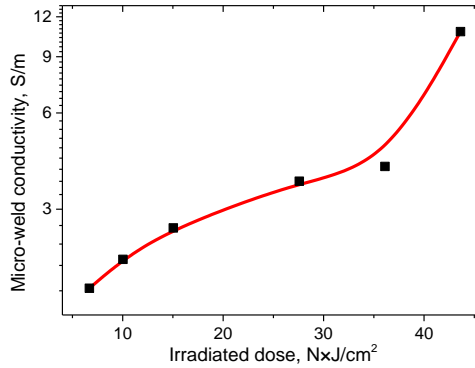


**Fig. 73.** Measured P2 micro-weld conductivity versus accumulated laser dose.

Single-scan P2 micro-welds with the laser irradiation doses ranging from 6.8 to 43.6  $N \times J/cm^2$  were performed through the ZnO front-contact side. The laser fluence and pulse overlap were controlled by adjusting the laser pulse energy and the laser scanning speed. The dependence between the extracted P2 scribe conductivity and the irradiated laser dose is presented in Fig. 73. Measurements revealed that the P2 scribe conductivity could be controlled by adjusting the irradiated laser dose: increasing the irradiated dose increased the micro-weld conductivity. The maximum P2 scribe conductivity of 10.8 S/m was obtained at the highest irradiation dose of 43.6  $N \times J/cm^2$ .

Previous investigations revealed that the micro-weld conductivity differed from sample to sample [99]. A variation could arise due to the CIGS composition changes between different samples. An optimum P2 micro-weld conductivity regime (43.6  $N \times J/cm^2$ , 0.09  $J/cm^2$ , and 100 mm/s) was tested on seven CIGS samples. As expected, resistivity scattered moderately from sample to sample. The best and the mean value of the P2 scribe conductivity was 28.3 S/m and 17.9 S/m, respectively. The standard deviation of the micro-weld conductivity was 2.2 S/m. The repeatability of the P2 micro-welds processed under the same conditions is shown in Table 18.

**Table 18.** P2 micro-weld repeatability test was done on 7 different CIGS #5 samples. Processing parameters: 43.6  $N \times J/cm^2$  laser irradiation dose, 0.09  $J/cm^2$  fluence, and 100 mm/s laser scanning speed.

Sample No.	1	2	3	4	5	6	7
P2 conductivity, S/m	10.8	17.2	15.9	13.8	22	18.3	28.3

## 8.2 A closer look into the morphology of the P2 micro-welds

Fig. 74 shows the SEM images of the investigated P2 micro-welds. In the case of the laser micro-weld #1, the irradiated laser dose was set to  $6.8 \text{ N} \times \text{J}/\text{cm}^2$  (laser scanning speed was set to 900 mm/s, and the laser fluence was set to  $0.12 \text{ J}/\text{cm}^2$ ). According to the SEM image, the front-contact layer was entirely removed revealing the slightly melted CIGS layer. The LLST measurements showed the micro-weld conductivity of 1.7 S/m.

For the P2 micro-weld #2, the irradiated laser dose was increased to  $16.7 \text{ N} \times \text{J}/\text{cm}^2$  by setting the laser fluence to  $0.3 \text{ J}/\text{cm}^2$ . The LLST measurements showed improved micro-weld conductivity to 2.2 S/m. However, the visual quality of the P2 scribe was not acceptable: a crack was formed in the Mo back-contact along the scribe.

Further, the laser fluence was reduced from 0.3 to  $0.09 \text{ J}/\text{cm}^2$ , and the scanning speed was reduced to 100 mm/s. This way, micro-weld #3 was processed with the maximum investigated laser dose of  $43.6 \text{ N} \times \text{J}/\text{cm}^2$  without damaging the Mo back-contact. The LLST measurements indicated the conductivity of 10.8 S/m. Furthermore, SEM analysis revealed the satisfactory quality of the micro-weld #3: the Mo back-contact was partly exposed but damage-free.

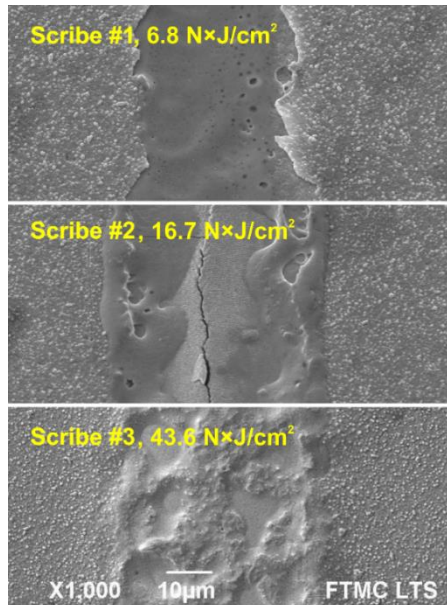


**Fig. 74.** SEM images of the P2 micro-weld in the complete P3 CIGS structure modified with different laser scribing parameters:  $0.12 \text{ J}/\text{cm}^2$ ,  $6.8 \text{ N} \times \text{J}/\text{cm}^2$ , 900 mm/s (scribe #1);  $0.3 \text{ J}/\text{cm}^2$ ,  $16.7 \text{ N} \times \text{J}/\text{cm}^2$ , 900 mm/s (scribe #2); and  $0.09 \text{ J}/\text{cm}^2$ ,  $43.6 \text{ N} \times \text{J}/\text{cm}^2$ , 100 mm/s (scribe #3).

It is worth mentioning that both #1 and #3 micro-welds were performed with laser fluence lower than the single pulse ablation threshold –  $0.14 \text{ J/cm}^2$  (ablation threshold was measured using Liu method [140]). For this reason, it was possible to irradiate sufficient laser dose into the CIGS layer in the case of micro-weld #3, so that it was transformed into the highly conductive compound without damaging the Mo back-contact.

### 8.3 Mini-module efficiency simulations

A CIGS mini-module was simulated to estimate efficiency losses caused by the resistivity of the serial interconnect. From this point, the P2 micro-weld resistivity is used instead of the conductivity since it is more common to describe the cell's P2 interconnect electrical behaviour in Ohms-centimetre. A simulated mini-module consisted of three CIGS cells connected in series via two serial interconnects. The CIGS electrical parameters were borrowed from [102] and are provided in Table 5 in Section 3.9 (solar cell #1). As previously, simulations were based on a classical diode equation. The P2 laser micro-weld resistivity was incorporated into the model considering that P2 weld resistance was connected in series with a series resistor. The model used in the simulation was presented in Section 3.9.1.

When the P2 interconnect resistivity was set to  $0 \text{ } \Omega \times \text{cm}$ , the simulated mini-module showed the maximum efficiency of 21.75 %. In reality, however, the P2 interconnects inevitably have some resistance. Therefore, Fig. 75 illustrates the dependence of the simulated 3-cell mini module efficiency on the P2 micro-weld resistivity. According to simulations, the P2 interconnect resistivity should be below  $1 \text{ } \Omega \times \text{cm}$  in order to preserve the high module efficiency, which is a typical value for the resistivity of commercial module P2 interconnects [137, 138, 141]. Therefore, in this case, relative efficiency losses would be limited to 1.8 % (21.4 % absolute efficiency). In our case, the best obtained P2 resistivity value was  $3.5 \text{ } \Omega \times \text{cm}$ , which corresponded to relative efficiency losses of 8.2 % (20.1 % absolute efficiency). On the other hand, the mean value obtained for P2 interconnects caused a solar module performance degradation to 18.6 %, absolute. Further increase in the interconnect resistivity resulted in even more significant efficiency loss.

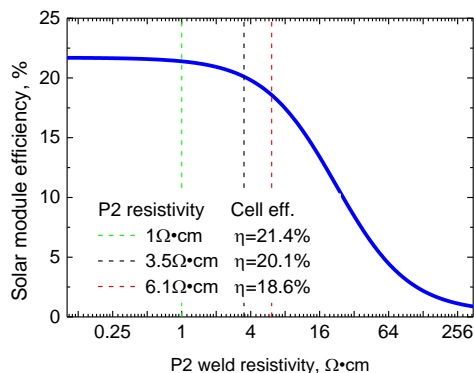


**Fig. 75.** Simulated efficiency dependence of the CIGS mini-module on the P2 micro-weld resistivity.

#### 8.4 Raman and EDS analysis of the laser transformed P2 interconnects

In this section, Raman spectroscopy was used to track material modifications after the P2 laser treatment. Raman analysis of the laser scribe #3 was performed in areas 1, 2, and 3, as shown in Fig. 76, while Fig. 77a presents the measured spectra. Here, a spectrum of a laser non-affected area is indicated as “1”. The main peak in the CIGS Raman spectrum was the  $A_1$  vibration line at  $174\text{ cm}^{-1}$  [142, 143]. A broad line in the range of  $210 - 230\text{ cm}^{-1}$  was a combined intrinsic vibration  $B_2/E$  of CIGS [144].

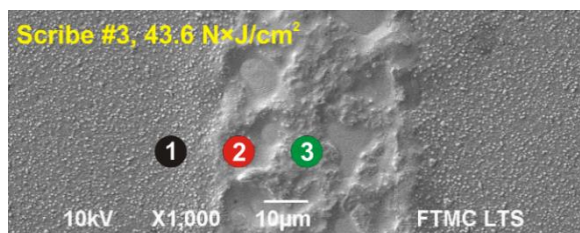


**Fig. 76.** A scheme of Raman measurements denoted with numbers 1, 2, and 3. Scribe #3 processing parameters:  $0.09\text{ J/cm}^2$ ,  $43.6\text{ N}\times\text{J/cm}^2$ ,  $100\text{ mm/s}$ .

At the edge of the laser scribe (measurement spot 2), the decrease of the main CIGS  $A_1$  peak was visible. Additionally, the peak at  $240\text{ cm}^{-1}$  became more pronounced in the Raman spectra, which indicated the formation of the  $\text{CuGaSe}_2$  (CGSe) phase. At the centre of the P2 scribe, the CGSe phase became the dominant one (see Fig. 77a).

The peak intensity ratio between the CGSe and CIGS  $A_1$  phases was measured at different laser irradiation doses (see Fig. 77b). A positive correlation was found: increasing the irradiated laser dose increased a CGSe/CIGS ratio. High laser doses led to the rapid decomposition of CIGS and formation of CGSe compound. This was observed as the domination of CGSe phase when the ratio exceeded unity. Furthermore, the  $\text{CuGaSe}_2$  phase

is more than 50 times more conductive than the CIGS phase [124, 145]. Increased P2 micro-weld conductivity correlated well with the formation of CGSe phase.

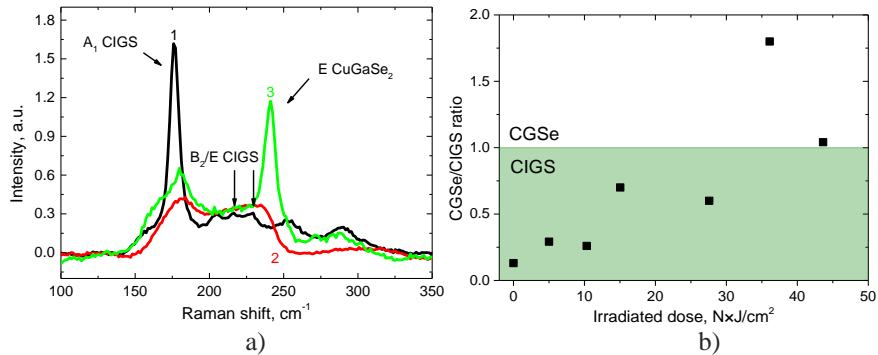


**Fig. 77.** Raman spectra of the laser transformed CIGS absorber layer (a). Numbers denote the measurement spots in the P2 scribe #3. The CGSe phase versus irradiated laser dose was measured in spot 3 (b).

EDS analysis was applied to detect Cu/(Ga+In) (CGI) element atomic ratio changes in the P2 scribes #1 and #3. Again, measured areas were numbered in Fig. 78. Measurement 1 was made in a laser non-affected area, while the remaining measurements (2 - 5) were evenly distributed from the edge to the centre of the micro-weld. According to [124, 146, 147], the resistivity of the CIGS films can be altered from  $10^6$  to  $10^{-1} \Omega \times \text{cm}$  by changing the CGI element atomic ratio from 0.7 to 1.2. Laser-induced heating can cause partial vaporisation of CIGS composing elements: In and Se evaporate first, and they are followed by Ga and Cu at higher temperatures [79].

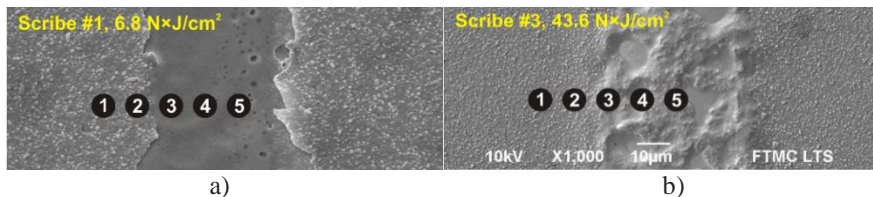


**Fig. 78.** A scheme of EDS measurements in the CIGS structure. Measurement spots are numbered and marked as black circles. Two irradiated laser doses were investigated:  $6.8 \text{ N} \times \text{J}/\text{cm}^2$  (a) and  $43.6 \text{ N} \times \text{J}/\text{cm}^2$  (b).

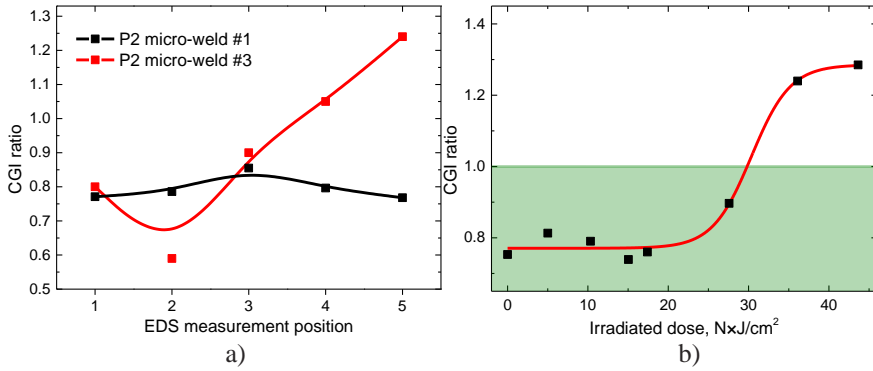


**Fig. 79.** CGI ratio of the laser transformed CIGS material (a) and the CGI ratio versus the irradiated laser dose measured in the centre of the P2 scribe #3 (b).

The CGI ratio measured in the laser non-affected areas fluctuated between 0.75 and 0.8 – a range of values close to a typical CGI ratio of the high-performance CIGS devices (see Fig. 79a) [102, 147].

In the case of the P2 micro-weld #1, the CGI ratio did not exceed 0.85 at any measured position in the laser-affected area. Hence, a minor P2 interconnect conductivity of 1.7 S/m was recorded.

However, CGI ratio was significant at the centre of micro-weld #3. The maximum value of 1.24 was detected at the centre of the channel, which indicated the formation of the Cu-rich phase, which was followed by an increase in the micro-weld conductivity.

Finally, it was discovered that the CGI ratio had a threshold type of behaviour (see Fig. 79b). No significant changes in the CGI ratio were observed for laser irradiation doses below  $20 \text{ N} \times \text{J}/\text{cm}^2$ . However, further increase of the laser irradiation dose resulted in a significant increase in the content of copper in the laser-treated areas. Lastly, CGI ratio changes coincided well with the P2 micro-weld conductivity relationship versus the irradiated laser dose.

Results suggest that a single picosecond laser source could be used for both P2 and P3 scribing processes [80]. For example, simultaneous P2 and P3 processing could be realised by dividing the laser beam into two paths. This type of solar cell processing can give benefits, such as higher flexibility in minimising the width of the interconnects, easier alignment of the scribes, faster processing rates, reduction in the number of production steps, and the production costs. However, the extracted P2 micro-weld conductivity fluctuated from sample to sample. It seems that the micro-weld approach is sensitive to the CIGS material properties. It is not clear how significantly the P2 conductivity fluctuations could affect the device efficiency on the large module scale.

## 8.5 Conclusions

1. Picosecond pulses can be used to transform the CIGS absorber layer into a highly conductive compound with the best achieved micro-weld resistivity value of  $3.5 \Omega \times \text{cm}$ , which slightly fell behind the typical P2 interconnect resistivity of  $1 \Omega \times \text{cm}$  found in conventional P2 interconnects.
2. Conductivity (resistivity) of the micro-weld was controlled by changing the irradiated laser dose into the CIGS solar cell: increasing the dose increased the micro-weld conductivity. It was associated with the degradation of the main CIGS phase and the formation of the Cu-rich phase (CGSe).
3. Micro-welds of the highest conductivity were achieved with the laser fluence below the single pulse ablation threshold. This way, sufficiently high laser dose could be irradiated into the CIGS layer to transform it into the highly conductive compound without completely removing the layer or damaging the Mo back-contact.
4. Three-cell mini-module efficiency simulations showed the relative efficiency loss of 8 % for the  $3.5 \Omega \times \text{cm}$  resistivity P2 interconnects. Absolute efficiency degraded from 21.75 % to 20.1 %.

## LIST OF MAIN CONCLUSIONS

1. The deviation between the areal CIGS conductivity simulated in a small probe and full area probe regimes depended on the areal conductivity of the CIGS sample and the area of the simulated structure. The difference can be kept below 5 % if the radius of the CIGS structure with  $194 \text{ S/m}^2$  areal conductivity is no larger than 6 mm.
2. Saturation of the measured parallel conductance of the CIGS solar cell was avoided by employing short and tightly packed laser scribes in the LLST technique.
3. LLST measurements revealed the relationship between the P3 scribe conductivity and the used laser wavelength. It was possible to minimise the scribe conductivity by properly selecting the laser radiation wavelength, so that, according to the simulations, most of the laser energy was absorbed either in the CIGS absorber or in the TCO front-contact but did not penetrate down to Mo back-contact.
4. Increasing the laser pulse repetition rate from 0.1 to 1 MHz increased the heat accumulation in the CIGS solar cell, which was observed as the pronounced melting, crack and void formation in the laser-scribed areas. This effect was highly dominant in the case of P3 Type 1 scribes.
5. The all-laser-scribed 8-cell mini-module structured using the P3 Type 2 process showed higher efficiency of 13.2 % compared to the 12.8 % efficiency of the device structured using the Type 1 approach.
6. Despite the reduced melting of the CIGS layer, the complete lift-off scribes were significantly more conductive compared to the P3 Type 1 and Type 2 approaches by 2.3 and 12.8 times, respectively.
7. Picosecond pulses can be used to transform the CIGS absorber layer into a highly conductive compound with the best achieved micro-weld resistivity value of  $3.5 \text{ } \Omega \times \text{cm}$ , which slightly fell behind the typical P2 interconnect resistivity of  $1 \text{ } \Omega \times \text{cm}$  found in conventional P2 interconnects.

## SUMMARY

In this thesis, research results on LLST technique development and application of laser radiation to perform P2 and P3 scribes in CIGS and CZTSe thin-film solar cells are presented.

LLST technique was applied to extract the conductivity of P3 scribes. Laser scribing was performed at different laser wavelengths (ranging from 355 nm to 2.5  $\mu\text{m}$ ) and pulse durations (300 fs, 1 ps, 10ps, 60 ps, and 6 ns). Laser-scribed areas were investigated with optical and SEM microscopes, Raman and EDS spectrometers. CIGS and CZTSe mini-module simulations were conducted to evaluate the possible device efficiency losses caused by the laser process. Simulation of coupled laser energy distribution in the CIGS cell was also presented.

Results showed that the LLST technique could be used to evaluate the conductivity of P3 scribes reliably. Changing laser radiation wavelength had a notable impact on the conductivity of the P3 scribes. Scribing at a high pulse repetition rate (in the range of 1 MHz), resulted in significant shunting of the CIGS device caused by the heat accumulation. The damage to the CZTSe solar cell patterned using a complete lift-off approach showed inverse dependence to the pulse duration. Finally, picosecond laser pulses at 1 MHz pulse repetition rate locally transformed CIGS solar cell into a highly conductive compound suitable for P2 interconnects.

## REFERENCES

- [1] M. Sharafi and T.Y. Elmekawy, Multi-objective optimal design of hybrid renewable energy systems using PSO-simulation based approach, *Renewable Energy*, **68**, 67-79 (2014).
- [2] Global Energy Transformation A Roadmap to 2050, retrieved from International Renewable Energy Agency (IRENA), website [https://www.irena.org/-/media/Files/IRENA/Agency/Publication/2018/Apr/IRENA\\_Report\\_GET\\_2018.pdf](https://www.irena.org/-/media/Files/IRENA/Agency/Publication/2018/Apr/IRENA_Report_GET_2018.pdf).
- [3] Fraunhofer ISE: Photovoltaics Report 2018, retrieved from Fraunhofer ISE, website [www.ise.fraunhofer.de/content/dam/ise/de/documents/publications/studies/Photovoltaics-Report.pdf](http://www.ise.fraunhofer.de/content/dam/ise/de/documents/publications/studies/Photovoltaics-Report.pdf).
- [4] M.A. Green, Y. Hishikawa, E.D. Dunlop, D.H. Levi, J. Hohl-Ebinger, and A.W.Y. Ho-Baillie, Solar cell efficiency tables (version 52), *Progress in Photovoltaics: Research and Applications*, **26**(7), 427-436 (2018).
- [5] S. Dongaonkar and M.A. Alam, In-Line Post-Process Scribing for Reducing Cell to Module Efficiency Gap in Monolithic Thin-Film Photovoltaics, *IEEE Journal of Photovoltaics*, **4**(1), 324-332 (2014).
- [6] S. Nishiwaki, A. Burn, S. Buecheler, M. Murr, S. Pilz, V. Romano, R. Witte, L. Krainer, G.J. Spühler, and A.N. Tiwari, A monolithically integrated high-efficiency Cu(In,Ga)Se<sub>2</sub> mini-module structured solely by laser, *Progress in Photovoltaics: Research and Applications*, **23**(12), 1908-1915 (2015).
- [7] A. Wehrmann, S. Puttnins, L. Hartmann, M. Ehrhardt, P. Lorenz, and K. Zimmer, Analysis of laser scribes at CIGS thin-film solar cells by localized electrical and optical measurements, *Optics & Laser Technology*, **44**(6), 1753-1757 (2012).
- [8] M. Rekow, R. Murison, C. Dunskey, C. Dinkel, J. Pern, L. Mansfield, T. Panarello, and S. Nikumb, P3 scribing processes using a pulse programmable industrial fiber laser, *Proceedings of 25th European Photovoltaic Solar Energy Conference and Exhibition*, (2010).
- [9] G.Q. Chen and X.F. Wu, Energy overview for globalized world economy: Source, supply chain and sink, *Renewable and Sustainable Energy Reviews*, **69**, 735-749 (2017).
- [10] N.L. Panwar, S.C. Kaushik, and S. Kothari, Role of renewable energy sources in environmental protection: A review, *Renewable and Sustainable Energy Reviews*, **15**(3), 1513-1524 (2011).
- [11] BP Statistical Review of World Energy 2017, retrieved from BP, website <https://www.bp.com/content/dam/bp/en/corporate/pdf/energy-economics/statistical-review-2017/bp-statistical-review-of-world-energy-2017-full-report.pdf>.
- [12] Xieqiu Zhang and X. Xiao, Recent progress of Cu(InGa)Se<sub>2</sub> solar cells, *Proc. SPIE 8312, Display, Solid-State Lighting, Photovoltaics, and Optoelectronics in Energy III*, (2011).
- [13] BP Statistical Review of World Energy 2018, retrieved from BP, website <https://www.bp.com/content/dam/bp/en/corporate/pdf/energy-economics/statistical-review/bp-stats-review-2018-full-report.pdf>.
- [14] O. Morton, A new day dawning?: Silicon Valley sunrise, *Nature*, **443**, 19 (2006).
- [15] Global PV capacity is expected to reach 969GW by 2025, retrieved from Power Technology, website <https://www.power-technology.com/comment/global-pv-capacity-expected-reach-969gw-2025/>.

- [16] S.A. Khalate, R.S. Kate, and R.J. Deokate, A review on energy economics and the recent research and development in energy and the  $\text{Cu}_2\text{ZnSnS}_4$  (CZTS) solar cells: A focus towards efficiency, *Solar Energy*, **169**, 616-633 (2018).
- [17] S. Rühle, Tabulated values of the Shockley–Queisser limit for single junction solar cells, *Solar Energy*, **130**, 139-147 (2016).
- [18] A. Shah, *Thin-Film Silicon Solar Cells*. (EPFL Press, 2010).
- [19] G. Blaesser and E. Rossi, Extrapolation of outdoor measurements of PV array I–V characteristics to standard test conditions, *Solar Cells*, **25**(2), 91-96 (1988).
- [20] A.M. Bagher, M.M.A. Vahid, and M. Mohsen, Types of Solar Cells and Application, *American Journal of Optics and Photonics*, **3**(5), 94-113 (2015).
- [21] T.D. Lee and A.U. Ebong, A review of thin film solar cell technologies and challenges, *Renewable and Sustainable Energy Reviews*, **70**, 1286-1297 (2017).
- [22] An Analysis of the Cost and Performance of Photovoltaic Systems as a Function of Module Area, retrieved from National Renewable Energy Laboratory (NREL), website [www.nrel.gov/docs/fy17osti/67006.pdf](http://www.nrel.gov/docs/fy17osti/67006.pdf).
- [23] T. Feurer, P. Reinhard, E. Avancini, B. Bissig, J. Löckinger, P. Fuchs, R. Carron, T.P. Weiss, J. Perrenoud, S. Stutterheim, S. Buecheler, and A.N. Tiwari, Progress in thin film CIGS photovoltaics – Research and development, manufacturing, and applications, *Progress in Photovoltaics: Research and Applications*, **25**, 645-667 (2017).
- [24] M. Powalla, S. Paetel, D. Hariskos, R. Wuerz, F. Kessler, P. Lechner, W. Wischmann, and T.M. Friedlmeier, Advances in Cost-Efficient Thin-Film Photovoltaics Based on  $\text{Cu}(\text{In,Ga})\text{Se}_2$ , *Engineering*, **3**(4), 445-451 (2017).
- [25] M.M. Osman and H.Z. Alibaba, Comparative Studies on Integration of Photovoltaic in Hot and Cold Climate, *Scientific Research Journal (Scirj)*, **3**(4), 48-60 (2015).
- [26] I.M. Dharmadasa, *Advances in Thin-Film Solar Cells*. (CRC Press, 2012).
- [27] F. Janiček, *Renewable Energy Sources 2*. (Renesans, 2012).
- [28] P. Singh and N.M. Ravindra, Analysis of series and shunt resistance in silicon solar cells using single and double exponential models, *Emerging Materials Research*, **1**(1), 33-38 (2012).
- [29] H. Hoppe, M. Seeland, and B. Muhsin, Optimal geometric design of monolithic thin-film solar modules: Architecture of polymer solar cells, *Solar Energy Materials and Solar Cells*, **97**, 119-126 (2012).
- [30] M.A. Green, *Solar cells: operating principles, technology, and system applications*. (Prentice-Hall, 1982).
- [31] S. Sharma, K.K. Jain, and A. Sharma, Solar Cells: In Research and Applications—A Review, *Materials Sciences and Applications*, **6**(12), 1145-1155 (2015).
- [32] J. Ramanujam and U.P. Singh, Copper indium gallium selenide based solar cells – a review, *Energy & Environmental Science*, **10**(6), 1306-1319 (2017).
- [33] G. Rajan, K. Aryal, S. Karki, P. Aryal, R.W. Collins, and S. Marsillac, Characterization and Analysis of Ultrathin CIGS Films and Solar Cells Deposited by 3-Stage Process, *Journal of Spectroscopy*, **2018**, 1-9 (2018).
- [34] A. Chirilă, S. Buecheler, F. Pianezzi, P. Bloesch, C. Gretener, A.R. Uhl, C. Fella, L. Kranz, J. Perrenoud, S. Seyrling, R. Verma, S. Nishiwaki, Y.E. Romanyuk, G. Bilger, and A.N. Tiwari, Highly efficient  $\text{Cu}(\text{In,Ga})\text{Se}_2$  solar cells grown on flexible polymer films, *Nature Materials*, **10**(11), 857-861 (2011).
- [35] S. Kim, H. Yoo, T.R. Rana, T. Enkhbat, G. Han, J. Kim, S. Song, K. Kim, J. Gwak, Y.-J. Eo, and J.H. Yun, Effect of Crystal Orientation and Conduction

- Band Grading of Absorber on Efficiency of Cu(In,Ga)Se<sub>2</sub> Solar Cells Grown on Flexible Polyimide Foil at Low Temperature, *Advanced Energy Materials*, **8**(26), 1801501 (2018).
- [36] E. Ghorbani, J. Kiss, H. Mirhosseini, G. Roma, M. Schmidt, J. Windeln, T.D. Kühne, and C. Felser, Hybrid-Functional Calculations on the Incorporation of Na and K Impurities into the CuInSe<sub>2</sub> and CuIn<sub>5</sub>Se<sub>8</sub> Solar-Cell Materials, *The Journal of Physical Chemistry C*, **119**(45), 25197-25203 (2015).
- [37] M.A. Green, K. Emery, Y. Hishikawa, W. Warta, and E.D. Dunlop, Solar cell efficiency tables (version 39), *Progress in Photovoltaics: Research and Applications*, **20**(1), 12-20 (2012).
- [38] M.A. Green, K. Emery, Y. Hishikawa, W. Warta, and E.D. Dunlop, Solar cell efficiency tables (version 42), *Progress in Photovoltaics: Research and Applications*, **21**(5), 827-837 (2013).
- [39] M.A. Green, K. Emery, Y. Hishikawa, W. Warta, and E.D. Dunlop, Solar cell efficiency tables (version 43), *Progress in Photovoltaics: Research and Applications*, **22**(1), 1-9 (2014).
- [40] M.A. Green, K. Emery, Y. Hishikawa, W. Warta, and E.D. Dunlop, Solar cell efficiency tables (version 44), *Progress in Photovoltaics: Research and Applications*, **22**(7), 701-710 (2014).
- [41] M.A. Green, Y. Hishikawa, W. Warta, E.D. Dunlop, D.H. Levi, J. Hohl-Ebinger, and A.W.H. Ho-Baillie, Solar cell efficiency tables (version 50), *Progress in Photovoltaics: Research and Applications*, **25**(7), 668-676 (2017).
- [42] E. Placzek-Popko, Top PV market solar cells 2016, *Opto-Electronics Review*, **25**(2), 55-64 (2017).
- [43] X. Liu, Y. Feng, H. Cui, F. Liu, X. Hao, G. Conibeer, D.B. Mitzi, and M. Green, The current status and future prospects of kesterite solar cells: a brief review, *Progress in Photovoltaics: Research and Applications*, **24**(6), 879-898 (2016).
- [44] H. Katagiri, K. Jimbo, W.S. Maw, K. Oishi, M. Yamazaki, H. Araki, and A. Takeuchi, Development of CZTS-based thin film solar cells, *Thin Solid Films*, **517**(7), 2455-2460 (2009).
- [45] M. Asaduzzaman, A.N. Bahar, M.M. Masum, and M.M. Hasan, Cadmium free high efficiency Cu<sub>2</sub>ZnSn(S,Se)<sub>4</sub> solar cell with Zn<sub>1-x</sub>Sn<sub>x</sub>O<sub>y</sub> buffer layer, *Alexandria Engineering Journal*, **56**(2), 225-229 (2017).
- [46] A. Freundlich, E.A. Lund, M.A. Scarpulla, and J.-F. Guillemoles, Modeling Cu<sub>2</sub>ZnSnS<sub>4</sub>(CZTS) solar cells with kesterite and stannite phase variation, *Proc. SPIE 8620, Physics, Simulation, and Photonic Engineering of Photovoltaic Devices II*, (2013).
- [47] S. Chen, X.G. Gong, A. Walsh, and S.-H. Wei, Crystal and electronic band structure of Cu<sub>2</sub>ZnSnX<sub>4</sub> (X=S and Se) photovoltaic absorbers: First-principles insights, *Applied Physics Letters*, **94**(4), 41903 (2009).
- [48] N. Kattan, B. Hou, D.J. Fermín, and D. Cherns, Crystal structure and defects visualization of Cu<sub>2</sub>ZnSnS<sub>4</sub> nanoparticles employing transmission electron microscopy and electron diffraction, *Applied Materials Today*, **1**(1), 52-59 (2015).
- [49] M.P. Paranthaman, W. Wong-Ng, and R.N. Bhattacharya, *Semiconductor Materials for Solar Photovoltaic Cells*. (Springer International Publishing, 2016).
- [50] G. Conibeer and A. Willoughby, *Solar Cell Materials: Developing Technologies*. (John Wiley & Sons, 2014).

- [51] H. Katagiri, Survey of development of CZTS-based thin film solar cells, *2012 IEEE 3rd International Conference on Photonics*, (2012).
- [52] S.K. Wallace, D.B. Mitzi, and A. Walsh, The Steady Rise of Kesterite Solar Cells, *ACS Energy Letters*, **2**(4), 776-779 (2017).
- [53] C.S. Solanki and H.K. Singh, *Anti-reflection and Light Trapping in c-Si Solar Cells* (Springer Singapore, 2017).
- [54] A. Smets, K. Jäger, O. Isabella, R.V. Swaaij, and M. Zeman, *Solar Energy- The physics and engineering of photovoltaic conversion, technologies and systems*. (UIT Cambridge, 2016).
- [55] Photovoltaic module documentation, retrieved from Solar Frontier, website [http://www.solar-frontier.com/eng/solutions/products/pdf/SAB12-0742\\_04\\_SFKxxx-S\\_One\\_Page\\_UL%20Manual.pdf](http://www.solar-frontier.com/eng/solutions/products/pdf/SAB12-0742_04_SFKxxx-S_One_Page_UL%20Manual.pdf).
- [56] eFlex3.1m – for Buildings & Mobility, retrieved from Flisom, website [www.flisom.com/wp-content/uploads/2018/04/Datasheet\\_eFlex\\_3.1m\\_201804.pdf](http://www.flisom.com/wp-content/uploads/2018/04/Datasheet_eFlex_3.1m_201804.pdf).
- [57] R. Scheer and H.W. Schock, *Photovoltaics: Physics, Technologies, and Thin Film Devices*. (Wiley, 2011).
- [58] D.J. Hwang, S. Kuk, Z. Wang, S. Fu, T. Zhang, G. Kim, W.M. Kim, and J.-H. Jeong, Laser scribing of CIGS thin-film solar cell on flexible substrate, *Applied Physics A*, **123**(1), 55 (2016).
- [59] Manufacturing with the roll-to-roll method, retrieved from website [www.zsw-bw.de/en/research/photovoltaics/topics/flexible-solar-cells-and-modules.html#c773](http://www.zsw-bw.de/en/research/photovoltaics/topics/flexible-solar-cells-and-modules.html#c773).
- [60] N. Aiko, N. Jiro, T. Hideyuki, S. Tadate, N. Hiroyuki, T. Kenji, K.-S. Yukiko, I. Shogo, S. Hajime, and N. Shigeru, Evaluation of femtosecond laser-scribed Cu(In,Ga)Se<sub>2</sub> solar cells using scanning spreading resistance microscopy, *Applied Physics Express*, **11**(3), 032301 (2018).
- [61] C. Dunskey and F. Colville, Solid state laser applications in photovoltaics manufacturing, *Proc. SPIE 6871*, 687129-10 (2008).
- [62] E. Schneller, N.G. Dhere, and A. Kar, Overview of laser processing in solar cell fabrication, *Proc. SPIE 9180, Laser Processing and Fabrication for Solar, Displays, and Optoelectronic Devices III*, (2014).
- [63] R. Witte, B. Frei, S. Schneeberger, S. Bücheler, S. Nishiwaki, A. Burn, M. Murali, V. Romano, and L. Krainer, Investigation of a reliable all-laser scribing process in thin film Cu(In,Ga)(S,Se)<sub>2</sub> manufacturing, *Proc. SPIE 8607, Laser Applications in Microelectronic and Optoelectronic Manufacturing (LAMOM) XVIII*, (2013).
- [64] H.P. Huber, F. Herrnberger, S. Kery, and S. Zoppel, Selective structuring of thin-film solar cells by ultrafast laser ablation, *Proc. SPIE 6881, Commercial and Biomedical Applications of Ultrafast Lasers VIII*, (2008).
- [65] S. Bahl, K. Kaufmann, S. Schoenfelder, and J. Bagdahn, Investigations and Modeling for Mechanical Scribing of CIGS Thin Film Solar Cells, *28th European Photovoltaic Solar Energy Conference and Exhibition*, (2013).
- [66] E. Markauskas, P. Gečys, I. Repins, C. Beall, and G. Račiukaitis, Laser lift-off scribing of the CZTSe thin-film solar cells at different pulse durations, *Solar Energy*, **150**, 246-254 (2017).
- [67] J.J. Scragg, P.J. Dale, D. Colombara, and L.M. Peter, Thermodynamic Aspects of the Synthesis of Thin-Film Materials for Solar Cells, *ChemPhysChem*, **13**(12), 3035-3046 (2012).

- [68] J.-F. Guillemoles, L. Kronik, D. Cahen, U. Rau, A. Jasenek, and H.-W. Schock, Stability Issues of Cu(In,Ga)Se<sub>2</sub>-Based Solar Cells, *The Journal of Physical Chemistry B*, **104**(20), 4849-4862 (2000).
- [69] J. Hermann, M. Benfarah, S. Bruneau, E. Axente, G. Coustillier, T. Itina, J.F. Guillemoles, and P. Alloncle, Comparative investigation of solar cell thin film processing using nanosecond and femtosecond lasers, *Journal of Physics D: Applied Physics*, **39**(3), 453 (2006).
- [70] P. Gecys, E. Markauskas, M. Gedvilas, G. Raciukaitis, I. Repins, and C. Beall, Ultrashort pulsed laser induced material lift-off processing of CZTSe thin-film solar cells, *Solar Energy*, **102**, 82-90 (2014).
- [71] A. Burn, V. Romano, M. Muralt, R. Witte, B. Frei, S. Bücheler, and S. Nishiwaki, Selective ablation of thin films in latest generation CIGS solar cells with picosecond pulses, *Proc. SPIE 8243, Laser Applications in Microelectronic and Optoelectronic Manufacturing (LAMOM) XVII*, (2012).
- [72] T.-W. Kim, J.-Y. Lee, D.-H. Kim, and H.-J. Pakh, Ultra-short laser patterning of thin-film CIGS solar cells through glass substrate, *International Journal of Precision Engineering and Manufacturing*, **14**(8), 1287-1292 (2013).
- [73] G. Heise, A. Börner, M. Dickmann, M. Englmaier, A. Heiss, M. Kemnitzer, J. Konrad, R. Moser, J. Palm, H. Vogt, and H.P. Huber, Demonstration of the monolithic interconnection on CIS solar cells by picosecond laser structuring on 30 by 30 cm<sup>2</sup> modules, *Progress in Photovoltaics: Research and Applications*, **23**(10), 1291-1304 (2015).
- [74] K. Kaufmann and C. Hagendorf, Indirect ablation of Cu(In, Ga)Se<sub>2</sub>-layers by ns pulses with a wavelength of 1342 nm, *2016 IEEE 43rd Photovoltaic Specialists Conference (PVSC)*, (2016).
- [75] H. Gerhard, D. Matthias, K. Jan, S. Sebastian, S. Jürgen, and P.H. Heinz, Laser lift-off initiated by direct induced ablation of different metal thin films with ultra-short laser pulses, *Journal of Physics D: Applied Physics*, **45**(31), 315303 (2012).
- [76] J. Sotrop, A. Kersch, M. Domke, G. Heise, and H.P. Huber, Numerical simulation of ultrafast expansion as the driving mechanism for confined laser ablation with ultra-short laser pulses, *Applied Physics A*, **113**(2), 397-411 (2013).
- [77] A. Buzás and Z. Geretovszky, Nanosecond laser-induced selective removal of the active layer of CuInGaSe<sub>2</sub> solar cells by stress-assisted ablation, *Physical Review B*, **85**(24), 245304 (2012).
- [78] P.O. Westin, U. Zimmermann, M. Ruth, and M. Edoff, Next generation interconnective laser patterning of CIGS thin film modules, *Solar Energy Materials and Solar Cells*, **95**(4), 1062-1068 (2011).
- [79] P.O. Westin, U. Zimmermann, and M. Edoff, Laser patterning of P2 interconnect via in thin-film CIGS PV modules, *Solar Energy Materials and Solar Cells*, **92**(10), 1230-1235 (2008).
- [80] P. Gečys, E. Markauskas, A. Žemaitis, and G. Račiukaitis, Variation of P2 series interconnects electrical conductivity in the CIGS solar cells by picosecond laser-induced modification, *Solar Energy*, **132**, 493-502 (2016).
- [81] P. Gecys, G. Raciukaitis, A. Wehrmann, K. Zimmer, A. Braun, and S. Ragnow, Scribing of Thin-Film Solar Cells with Picosecond and Femtosecond Lasers, *Journal of Laser Micro/Nanoengineering*, **7**(1), 33-37 (2012).
- [82] S.H. Lee, C.K. Kim, J.H. In, H.S. Shim, and S.H. Jeong, Selective removal of CuIn<sub>1-x</sub>Ga<sub>x</sub>Se<sub>2</sub> absorber layer with no edge melting using a nanosecond Nd: YAG laser, *Journal of Physics D: Applied Physics*, **46**(10), 105502 (2013).

- [83] R. Moser, M. Domke, G. Marowsky, and H.P. Huber, Nanosecond Laser Lift-Off of a Copper-Indium-Diselenide Thin Film at a Wavelength of 1342nm, *Physics Procedia*, **41**, 746-751 (2013).
- [84] J. Hermann, M. Benfarah, G. Coustillier, S. Bruneau, E. Axente, J.F. Guillemoles, M. Sentis, P. Alloncle, and T. Itina, Selective ablation of thin films with short and ultrashort laser pulses, *Applied Surface Science*, **252**(13), 4814-4818 (2006).
- [85] J. Hermann, M. Benfarah, S. Bruneau, E. Axente, G. Coustillier, T. Itina, J.F. Guillemoles, and P. Alloncle, Comparative investigation of solar cell thin film processing using nanosecond and femtosecond lasers, *Journal of Physics D: Applied Physics*, **39**(3), 453-460 (2006).
- [86] B. Vidhya, S. Velumani, and R. Asomoza, Effect of milling time and heat treatment on the composition of  $\text{CuIn}_{0.75}\text{Ga}_{0.25}\text{Se}_2$  nanoparticle precursors and films, *Journal of Nanoparticle Research*, **13**(7), 3033-3042 (2011).
- [87] A. Narazaki, T. Sato, H. Niino, H. Takada, K. Torizuka, J. Nishinaga, Y. Kamikawa-Shimizu, S. Ishizuka, H. Shibata, and S. Niki, Ultrafast laser scribing of transparent conductive oxides in  $\text{Cu}(\text{In,Ga})\text{Se}_2$  solar cells via laser lift-off process: the control of laser-induced damage, *Proc. SPIE 10091, Laser Applications in Microelectronic and Optoelectronic Manufacturing (LAMOM) XXII*, (2017).
- [88] P. Gečys, E. Markauskas, J. Dudutis, and G. Račiukaitis, Interaction of ultrashort laser pulses with CIGS and CZTSe thin films, *Applied Physics A*, **114**(1), 231-241 (2014).
- [89] K. Stelmaszczyk, C. Schultz, M. Schüle, M. Weizman, C. A. Kaufmann, R. Schlatmann, B. Rau, V. Quaschnig, B. Stegemann, and F. Fink, Investigation of thin-film CIGS degradation under P2 scribe laser illumination, *29th European Photovoltaic Solar Energy Conference and Exhibition*, (2014).
- [90] O. Stenzel, *The Physics of Thin Film Optical Spectra*. (Springer, 2015).
- [91] P. Schaaf, *Laser Processing of Materials– Fundamentals, Applications and Developments*. (Springer Science & Business Media, 2010).
- [92] K. Sugioka, M. Meunier, and A. Piqué, *Laser Precision Microfabrication*. (Springer, 2010).
- [93] E.T. Akinlabi, R.M. Mahamood, and S.A. Akinlabi, *Advanced Manufacturing Techniques Using Laser Material Processing*. (Engineering Science Reference, 2016).
- [94] A.M. Rodin, M. Grishin, and A. Michailovas, Picosecond laser with 11W output power at 1342nm based on composite multiple doping level  $\text{Nd:YVO}_4$  crystal, *Optics & Laser Technology*, **76**, 46-52 (2016).
- [95] E. Smith and G. Dent, *Modern Raman Spectroscopy: A Practical Approach*. (Wiley, 2005).
- [96] R. Kiselev, I.W. Schie, S. Aškračić, C. Krafft, J. Popp, and K. Gerwert, Design and first applications of a flexible Raman micro-spectroscopic system for biological imaging, *Biomedical Spectroscopy and Imaging*, **5**(2), 115-127 (2016).
- [97] K. Bouzidi, M. Chegaar, and M. Aillerie, Solar Cells Parameters Evaluation from Dark I-V Characteristics, *Energy Procedia*, **18**, 1601-1610 (2012).
- [98] X. Wang, M. Ehrhardt, P. Lorenz, C. Scheit, S. Ragnow, X.W. Ni, and K. Zimmer, In-process measuring of the electrical shunt resistance of laser-scribed thin-film stacks by nested circular scribes, *Review of Scientific Instruments*, **84**(10), 104704 (2013).

- [99] E. Markauskas, P. Gečys, A. Žemaitis, M. Gedvilas, and G. Račiukaitis, Validation of monolithic interconnection conductivity in laser scribed CIGS thin-film solar cells, *Solar Energy*, **120**, 35-43 (2015).
- [100] X. Wang, M. Ehrhardt, P. Lorenz, C. Scheit, S. Ragnow, X.W. Ni, and K. Zimmer, The influence of the laser parameter on the electrical shunt resistance of scribed Cu(InGa)Se<sub>2</sub> solar cells by nested circular laser scribing technique, *Applied Surface Science*, **302**, 194-197 (2014).
- [101] K. Zimmer, X. Wang, P. Lorenz, L. Bayer, M. Ehrhardt, C. Scheit, and A. Braun, In-process Evaluation of Electrical Properties of CIGS Solar Cells Scribed with Laser Pulses of Different Pulse Lengths, *Physics Procedia*, **56**, 1024-1033 (2014).
- [102] P. Jackson, D. Hariskos, R. Wuerz, O. Kiowski, A. Bauer, T.M. Friedlmeier, and M. Powalla, Properties of Cu(In,Ga)Se<sub>2</sub> solar cells with new record efficiencies up to 21.7%, *physica status solidi (RRL)*, **9**(1), 28-31 (2015).
- [103] P. Gečys, E. Markauskas, S. Nishiwaki, S. Buecheler, R. De Loor, A. Burn, V. Romano, and G. Račiukaitis, CIGS thin-film solar module processing: case of high-speed laser scribing, *Scientific Reports*, **7**, 40502 (2017).
- [104] G. Brammertz, M. Buffière, S. Oueslati, H. ElAnzeery, K.B. Messaoud, S. Sahayaraj, C. Köble, M. Meuris, and J. Poortmans, Characterization of defects in 9.7% efficient Cu<sub>2</sub>ZnSnSe<sub>4</sub>-CdS-ZnO solar cells, *Applied Physics Letters*, **103**(16), 163904 (2013).
- [105] Y. Liao, S. Zhang, Z. Tang, X. Liu, and K. Huang, Power loss density of electromagnetic waves in unimolecular reactions, *RSC Advances*, **7**(43), 26546-26550 (2017).
- [106] J. Clatot, G. Campet, A. Zeinert, C. Labrugère, and A. Rougier, Room temperature transparent conducting oxides based on zinc oxide thin films, *Applied Surface Science*, **257**(12), 5181-5184 (2011).
- [107] C. Jagadish and S. Pearton, *Zinc Oxide Bulk, Thin Films and Nanostructures*. (Elsevier Science, 2006).
- [108] E. Khawaja and S.G. Tomlin, The optical constants of thin evaporated films of cadmium and zinc sulphides, *Journal of Physics D: Applied Physics*, **8**(5), 581 (1975).
- [109] E.D. Palik, *Handbook of Optical Constants of Solids*. (Academic Press, 1997).
- [110] M. Urbańczyk, W. Jakubik, and E. Maciak, Sensor Properties of Cadmium Sulphide (CdS) Thin Films Insurface Acoustic Wave System - Preliminary Results, *Molecular and Quantum Acoustics*, **26**, 273-281 (2005).
- [111] P.D. Paulson, R.W. Birkmire, and W.N. Shafarman, Optical characterization of CuIn<sub>1-x</sub>Ga<sub>x</sub>Se<sub>2</sub> alloy thin films by spectroscopic ellipsometry, *Journal of Applied Physics*, **94**(2), 879-888 (2003).
- [112] M.-L. Liu, F.-Q. Huang, L.-D. Chen, and I.-W. Chen, A wide-band-gap *p*-type thermoelectric material based on quaternary chalcogenides of Cu<sub>2</sub>ZnSnQ<sub>4</sub> (Q=S,Se), *Applied Physics Letters*, **94**(20), 202103 (2009).
- [113] H. Yang, L.A. Jauregui, G. Zhang, Y.P. Chen, and Y. Wu, Nontoxic and Abundant Copper Zinc Tin Sulfide Nanocrystals for Potential High-Temperature Thermoelectric Energy Harvesting, *Nano Letters*, **12**(2), 540-545 (2012).
- [114] R.S. Hixson and M.A. Winkler, Thermophysical properties of molybdenum and rhenium, *International Journal of Thermophysics*, **13**(3), 477-487 (1992).
- [115] J.R. Davis, *Heat-resistant materials*. (ASM International, 1997).

- [116] Matthias Haldimann, Andreas Luible, and M. Overend, *Structural Use of Glass*. (IABSE, 2008).
- [117] S. Lauzurica, J.J. García-Ballesteros, M. Colina, I. Sánchez-Aniorte, and C. Molpeceres, Selective ablation with UV lasers of a-Si:H thin film solar cells in direct scribing configuration, *Applied Surface Science*, **257**(12), 5230-5236 (2011).
- [118] P. Lorenz, T. Smausz, T. Csizmadia, M. Ehrhardt, K. Zimmer, and B. Hopp, Shadowgraph studies of laser-assisted non-thermal structuring of thin layers on flexible substrates by shock-wave-induced delamination processes, *Applied Surface Science*, **336**, 43-47 (2015).
- [119] S. Johnston, T. Unold, I. Repins, R. Sundaramoorthy, K.M. Jones, B. To, N. Call, and R. Ahrenkiel, Imaging characterization techniques applied to Cu(In,Ga)Se<sub>2</sub> solar cells, *Journal of Vacuum Science & Technology A*, **28**(4), 665-670 (2010).
- [120] A. Gerber, V. Huhn, T.M.H. Tran, M. Siegloch, Y. Augarten, B.E. Pieters, and U. Rau, Advanced large area characterization of thin-film solar modules by electroluminescence and thermography imaging techniques, *Solar Energy Materials and Solar Cells*, **135**, 35-42 (2015).
- [121] S. Sho, Photoluminescence characterization of Cu(In,Ga)Se<sub>2</sub> solar-cell processes, *physica status solidi (b)*, **252**(6), 1211-1218 (2015).
- [122] A.Y. Polyakov, N.B. Smirnov, A.V. Govorkov, E.A. Kozhukhova, S.J. Pearton, D.P. Norton, A. Osinsky, and A. Dabiran, Electrical properties of undoped bulk ZnO substrates, *Journal of Electronic Materials*, **35**(4), 663-669 (2006).
- [123] A.S. Khomane, Crystallographic, morphological, optical and electrical properties of CBD deposited cadmium sulphide thin films, *Archives of Applied Science Research*, **3**, 273-279 (2011).
- [124] Y.-m. Xue, B.-h. Yang, C.-q. Qu, L. Zhang, C.-m. Xu, and Y. Sun, Structural and electrical properties of co-evaporated In, Ga-rich CIGS thin films, *Optoelectronics Letters*, **4**(6), 437-439 (2008).
- [125] T.-W. Kim, H.-J. Park, H.K. Park, D.J. Hwang, and C.P. Grigoropoulos, Comparison of multilayer laser scribing of thin film solar cells with femto, pico, and nanosecond pulse durations, *SPIE Solar Energy + Technology*, (2009).
- [126] F. Bauer, A. Michalowski, T. Kiedrowski, and S. Nolte, Heat accumulation in ultra-short pulsed scanning laser ablation of metals, *Optics Express*, **23**(2), 1035-1043 (2015).
- [127] P. Gečys, G. Račiukaitis, M. Ehrhardt, K. Zimmer, and M. Gedvilas, ps-laser scribing of CIGS films at different wavelengths, *Applied Physics A*, **101**(2), 373-378 (2010).
- [128] P. Gecys, E. Markauskas, G. Raciukaitis, I. Repins, and C. Beall, Selective Front Side Patterning of CZTS Thin-Film Solar Cells by Picosecond Laser Induced Material Lift-Off Process, *Phys. Procedia*, **41**(0), 734-738 (2013).
- [129] D. Nam, A.S. Opanasyuk, P.V. Koval, A.G. Ponomarev, A.R. Jeong, G.Y. Kim, W. Jo, and H. Cheong, Composition variations in Cu<sub>2</sub>ZnSnSe<sub>4</sub> thin films analyzed by X-ray diffraction, energy dispersive X-ray spectroscopy, particle induced X-ray emission, photoluminescence, and Raman spectroscopy, *Thin Solid Films*, **562**, 109-113 (2014).
- [130] M. Grossberg, J. Krustok, J. Raudoja, K. Timmo, M. Altosaar, and T. Raadik, Photoluminescence and Raman study of Cu<sub>2</sub>ZnSn(Se<sub>x</sub>S<sub>1-x</sub>)<sub>4</sub> monograins for photovoltaic applications, *Thin Solid Films*, **519**(21), 7403-7406 (2011).

- [131] P.M.P. Salomé, P.A. Fernandes, and A.F. da Cunha, Morphological and structural characterization of  $\text{Cu}_2\text{ZnSnSe}_4$  thin films grown by selenization of elemental precursor layers, *Thin Solid Films*, **517**(7), 2531-2534 (2009).
- [132] P. Uday Bhaskar, G. Suresh Babu, Y.B. Kishore Kumar, and V. Sundara Raja, Growth and characterization of  $\text{Cu}_2\text{ZnSnSe}_4$  thin films by a two-stage process, *Solar Energy Materials and Solar Cells*, **115**, 181-188 (2013).
- [133] S. Venkatachalam, S. Agilan, D. Mangalaraj, and S.K. Narayandass, Optoelectronic properties of ZnSe thin films, *Materials Science in Semiconductor Processing*, **10**(2), 128-132 (2007).
- [134] S. Siebentritt, Why are kesterite solar cells not 20% efficient?, *Thin Solid Films*, **535**, 1-4 (2013).
- [135] A. Redinger and S. Siebentritt, Coevaporation of  $\text{Cu}_2\text{ZnSnSe}_4$  thin films, *Applied Physics Letters*, **97**(9), 092111 (2010).
- [136] M.A. Olgar, Y. Atasoy, B.M. Başol, M. Tomakin, G. Aygun, L. Ozyuzer, and E. Bacaksız, Influence of copper composition and reaction temperature on the properties of CZTSe thin films, *Journal of Alloys and Compounds*, **682**, 610-617 (2016).
- [137] J.-H. Yoon, J.-K. Park, W.M. Kim, J. Lee, H. Pak, and J.-h. Jeong, Characterization of efficiency-limiting resistance losses in monolithically integrated  $\text{Cu}(\text{In,Ga})\text{Se}_2$  solar modules, *Scientific Reports*, **5**, 7690 (2015).
- [138] J. Johansson, *Modelling and Optimization of CIGS Solar Cell Modules*. (Lund university, 2007).
- [139] A.D. Compaan, I. Matulionis, and S. Nakade, Laser scribing of polycrystalline thin films, *Optics and Lasers in Engineering*, **34**(1), 15-45 (2000).
- [140] J.M. Liu, Simple technique for measurements of pulsed Gaussian-beam spot sizes, *Optics Letters*, **7**(5), 196-198 (1982).
- [141] J. Ermer, R. Gay, D. Pier, and D. Tarrant, Challenges and progress in the scale up of  $\text{CuInSe}_2$  thin film photovoltaic technology, *Journal of Vacuum Science & Technology A*, **11**(4), 1888-1895 (1993).
- [142] C.-M. Xu, X.-L. Xu, J. Xu, X.-J. Yang, J. Zuo, N. Kong, W.-H. Huang, and H.-T. Liu, Composition dependence of the Raman  $A_1$  mode and additional mode in tetragonal  $\text{Cu-In-Se}$  thin films, *Semiconductor Science and Technology*, **19**(10), 1201-1206 (2004).
- [143] L. Ouyang, M. Zhao, D. Zhuang, J. Han, Z. Gao, L. Guo, X. Li, R. Sun, and M. Cao, Annealing treatment of  $\text{Cu}(\text{In,Ga})\text{Se}_2$  absorbers prepared by sputtering a quaternary target for 13.5% conversion efficiency device, *Solar Energy*, **118**, 375-383 (2015).
- [144] D. Wang, L. Wan, Z. Bai, and Y. Cao, Mixed phases in  $p$ -type  $\text{CuInSe}_2$  thin films detected by using micro-Raman scattering spectroscopy, *Applied Physics Letters*, **92**(21), 211912 (2008).
- [145] S.R. Kodigala, *Thin Films and Nanostructures*, S.R. Kodigala, Editor 2010, Academic Press. p. 319-391.
- [146] S.H. Kwon, D.Y. Lee, B.T. Ahn, K.H. Yoon, and J. Song, Characterization of  $\text{Cu}(\text{In}_{1-x}\text{Ga}_x)\text{Se}_2$  films prepared by three-stage coevaporation and their application to CIGS solar cells for a 14.48 % efficiency, *Journal of the Korean Physical Society*, **39**(4), 655-660 (2001).
- [147] A. Virtuani, E. Lotter, M. Powalla, U. Rau, J.H. Werner, and M. Acciarri, Influence of Cu content on electronic transport and shunting behavior of  $\text{Cu}(\text{In,Ga})\text{Se}_2$  solar cells, *Journal of Applied Physics*, **99**(1), 014906 (2006).

## NOTES

Vilniaus universiteto leidykla  
Universiteto g. 1, LT-01513 Vilnius  
El. p. [info@leidykla.vu.lt](mailto:info@leidykla.vu.lt),  
[www.leidykla.vu.lt](http://www.leidykla.vu.lt)  
Tiražas 25 egz.